Master Thesis : Synergistic visible-light photocatalysis by ZnO nanohybrids immobilized on activated halloysite for textile dyes degradation (including an introduction to research methodology)

Auteur : Hasan, Md Nahid Bin
Promoteur(s) : Lambert, Stéphanie
Faculté : Faculté des Sciences appliquées
Diplôme : Master : ingénieur civil en chimie et science des matériaux, à finalité spécialisée en Advanced Materials - Innovative Recycling
Année académique : 2025-2026
URI/URL : http://hdl.handle.net/2268.2/26121

UNIVERSITE DE LIEGE
FACULTE DES SCIENCES APPLIQUEES

Synergistic visible-light photocatalysis by ZnO nanohybrids immobilized on activated halloysite clay for textile dyes degradation

Written by

Hasan Md Nahid Bin

Thesis presented to obtain the degree of:

Master of Science in Chemical and Materials Science Engineering, professional focus in Advanced Materials– Innovative Recycling

Thesis supervisor:

Prof. LAMBERT Stéphanie

Mr. Ngue Song Pierre

Academic year: **2025 – 2026**

Acknowledgement

First, I would like to thank everyone I had the pleasure of meeting during my master's thesis. I begin by expressing my sincere gratitude from the core of my heart to my supervisor, Prof. Stéphanie Lambert, for accepting and welcoming me to her team and allowing me to work on this wonderful research project of my interest. I am truly grateful for her kindness, her availability, time in answering my questions, and discussion with her anytime, and her valuable feedback on this thesis. In a word she silently motivated me till the end of my work which is unimaginable.

Importantly this work would not have been successful without the support of my lab supervisor, Mr. Pierre Ngué Song. I am deeply thankful for his day-to-day guidance, suggestion, and dedication throughout the entire time. He was always available to answer my questions, even during his busiest moments, and his support greatly helped me stay motivated and reassured me during times of doubt. He provided valuable assistance in the laboratory, like teaching me experimental procedures, apparatus and developing methodology and ensured that I had all the necessary materials for synthesis. He also guided me during my material synthesis, materials characterization and sample making. I also sincerely thank him for his guidance to photocatalytic test. A deep gratitude to him for careful proofreading, thoughtful corrections, and constant support during the writing of this report.

I would like to thank Mr. Jérémy Geens for my lab training and useful information during the lab. I would also like to thank Dr. Julien Mahy and Dr. Alexandre Léonard for their help, their willingness to answer my questions regarding characterization techniques and data interpretation. I also thank Mr. Baptiste Herlin from Centexbel, the technician who helped me during photocatalytic tests, for his guidance and valuable insights. I am also extending my gratitude to the members of the NCE laboratory at the University of Liège for their kindness and assistance throughout this project.

Finally, it would not be possible to be here today without the support of my family, who sacrificed a great deal to help me on this university journey, and I am sincerely grateful to them. I also want to thank my friends and peers for their advice, as well as my close friends. I cannot mention everyone, but I am thankful for all the wonderful moments I have shared with them throughout my university years.

Summary

This study wanted to address the water pollution caused by textile azo dyes and synthesized advanced photocatalytic composite materials based on clay supported ZnO nano hybrids for enhanced photocatalytic degradation of azo dyes along with establishing their synergistic relationship. Due to limited visible-light activity of ZnO in photocatalysis, different pure, metal-doped and modified materials were synthesized and successfully ZnO nanoparticles were immobilized into them to form binary and ternary photocatalytic composite materials *i.e.* ZnO nano hybrids and tested for enhanced photocatalytic degradation of reactive black 5 (RB5) azo dyes in synthetic solution. Specifically, raw halloysite was modified by chemical treatment and an activated clay (AC) was produced. Then graphitic carbon nitride (g-C_3N_4) was synthesized and modified with Fe metal doping to form Fe/g-C_3N_4. After that ZnO nano particles were synthesized using precipitation process and 4 different composite materials were formed particularly [Fe/g-C_3N_4]/AC, ZnO/AC, [Fe/g-C_3N_4]/ZnO and [Fe/g-C_3N_4]/ZnO/AC. Then 6 different analytical tests were carried out namely SEM, XRD, DRS, Nitrogen adsorption-desorption, XPS and zeta potential for assessing the surface morphology, surface texture, crystal structure, optical properties and surface charge, etc. of 8 synthesized materials. To evaluate the photocatalytic performance of 8 sample materials, photocatalytic experiments were carried out in the photocatalytic reactor for degradation of RB5 azo dye under Visible light. The initial and residual concentrations of the dye were noted after 0, 2, 4, 6, and 8 h and RB5 degradation percentage was calculated. It was observed that, ternary composite [Fe/g-C_3N_4]/ZnO/AC is the best sample, showing a removal of 70% within 2 h ending with the complete degradation of azo dye after 8 h. For this sample, the RB5 degradation kinetic law was also determined and a probable mechanism of RB5 dye degradation was proposed. To conclude, binary and ternary heterojunction composite materials like [Fe/g-C_3N_4]/ZnO and [Fe/g-C_3N_4]/ZnO/AC can enhance the photocatalytic performance of pure ZnO for degradation of azo dyes overcoming the barrier of limited visible light activity.

Keywords: Azo dyes, photocatalysis, halloysite nano clay, ZnO nanoparticles, wastewater, ternary composite, degradation.

Contents

Chapter 1: Introduction 1

1.1 Azo dyes 1

1.2 Water pollution and environmental impact caused by azo dyes 2

1.3 Wastewater treatment techniques to remove azo dyes 4

1.3.1 Adsorption process 6

1.3.1.1 Clay materials and Halloysite nano clay adsorbent materials 8

1.3.1.2 Halloysite nano clay 11

1.3.2 Advanced Oxidation Processes (AOP) 14

1.4 Photocatalysis process 15

1.4.1 ZnO-based photocatalysis 16

1.5 Objectives of master thesis 24

Chapter 2: Materials and methods 25

2.1 Reagents and chemicals 25

2.2 Activation of halloysite 25

2.3 Synthesis of carbon graphitic nitride (g-C_3N_4) 26

2.4 Synthesis of iron doped-carbon graphitic nitride (Fe/g-C_3N_4) 26

2.5 Synthesis of [Fe/g-C_3N_4]/AC binary composite 27

2.6 Synthesis of ZnO 28

2.7 Synthesis of ZnO/AC composite 29

2.8 Synthesis of [Fe/g-C_3N_4]/ZnO composite 30

2.9 Synthesis of [Fe/g-C_3N_4]/ZnO/AC ternary composite 31

2.10 Characterization of samples 32

2.10.1 Scanning Electron Microscopy (SEM) 32

2.10.2 X-ray Diffraction (XRD) 34

2.10.3 Nitrogen adsorption-desorption measurements 35

2.10.4 Zeta potential 36

2.10.5 X-ray photoelectron spectroscopy (XPS) 37

2.10.6 Diffuse reflectance spectroscopy (DRS) 38

2.11 Photocatalytic experiments 40

Chapter 3: Results and discussion 42

3.1 SEM images analysis 42

3.2 XRD analysis 45

3.3 Textural properties 50
3.4 Zeta potential analysis 53
3.5 DRS analysis 55
3.6 XPS analysis 59
3.7 Photocatalytic degradation analysis 66
Chapter 4: Conclusion and Perspectives 74
4.1 Conclusion 74
4.2 Perspectives 76
Appendices 77
Bibliography 82

List of figures

Figure 1: Chemical structure of an azo dye 1
Figure 2: Common azo dyes names and structures 2
Figure 3: Water pollution caused by azo dyes 3
Figure 4: Toxic effect of azo dyes in ecosystem 3
Figure 5: Pie-chart showing the percentage of literature available on dye removal for (a) various physico-chemical and biological techniques and (b) Adsorption techniques using different adsorbents. 5
Figure 6: Mechanisms of adsorption process 7
Figure 7: Application of different adsorbent materials in treating dyeing polluted water 7
Figure 8: Classification of clay minerals 9
Figure 9: Two structural sheets of clay minerals 9
Figure 10: Applications of clay minerals 10
Figure 11: Structure of kaolinite and Halloysite clay 11
Figure 12: Tubular structure of halloysite clay 12
Figure 13: Adsorption mechanisms of RB5 dye by activated halloysite clay (AC) 13
Figure 14: Reaction mechanisms of different AOPs 14
Figure 15: Mechanism of photocatalytic degradation of water pollutants 16
Figure 16: Crystal structure of ZnO (a) Zinc blende (b) wurtzite and (c) rock salt 17
Figure 17: Applications of ZnO nanoparticles 17
Figure 18: ZnO nanoparticles synthesis method 18
Figure 19: Photocatalytic mechanism of ZnO to degrade dye pollutant 20
Figure 20: Synthesis route of g-C_3N_4 22
Figure 21: Photocatalytic mechanism of Fe/g-C_3N_4 samples 23
Figure 22: Synthesis of activated clay (AC) 26
Figure 23: Synthesis of g-C_3N_4 26
Figure 24: Synthesis of Fe/g-C_3N_4 sample 27
Figure 25 : Synthesis of [Fe/g-C_3N_4]/AC 28
Figure 26 : Synthesis of ZnO sample 29
Figure 27: Synthesis of ZnO/AC sample 30
Figure 28 : Synthesis of [Fe/g-C_3N_4]/ZnO sample 31
Figure 29 : Synthesis of [Fe/g-C_3N_4]/ZnO/AC 32
Figure 30: SEM electron beam interactions with sample 33
Figure 31: Typical mechanism of XRD technique 34
Figure 32: Photoelectron spectrometer with electron energy analyzer for XPS 38
Figure 33: DRS mechanisms 39
Figure 34: Photocatalytic reactor setup and arrangement 40
Figure 35: Photocatalytic degradation experiment of RB5 41
Figure 36: UV-Vis spectrophotometer and calibration curve of RB5 dye 41
Figure 37 : SEM images of (a) Raw clay (RC) and (b) Activated clay (AC) 42
Figure 38: SEM micrographs of (a) g-C_3N_4 and (b) Fe/g-C_3N_4 43
Figure 39: SEM images of ZnO nano particles 43
Figure 40: SEM images of ZnO/AC composite 44
Figure 41 : SEM images of [Fe/g-C_3N_4]/ZnO composite 44
Figure 42 : SEM images of [Fe/g-C_3N_4]/ZnO/AC ternary composite 45

Figure 43: XRD spectra of RC, MH800 and AC 46
Figure 44: XRD spectra of g-C_3N_4 and Fe/g-C_3N_4 samples 47
Figure 45: XRD spectra of AC, Fe/g-C_3N_4 and [Fe/g-C_3N_4]/AC samples 48
Figure 46: XRD spectra of ZnO, ZnO/AC, [Fe/g-C_3N_4]/ZnO and [Fe/g-C_3N_4]/ZnO/AC samples 49
Figure 47: Nitrogen adsorption-desorption isotherms of RC, MH800 and AC samples 51
Figure 48: Nitrogen adsorption-desorption isotherms of g-C_3N_4, Fe/g-C_3N_4 and [Fe/g-C_3N_4]/AC samples 52
Figure 49: Nitrogen adsorption-desorption isotherms of ZnO, ZnO/AC, [Fe/g-C_3N_4]/ZnO and [Fe/g-C_3N_4]/ZnO/AC samples 53
Figure 50: UV-Vis DRS curves of ZnO/AC, AC and ZnO samples 56
Figure 51: UV-Vis DRS curves of [Fe/g-C_3N_4]/AC, Fe/g-C_3N_4 and g-C_3N_4 samples 57
Figure 52: UV-Vis DRS curves of [Fe/g-C_3N_4]/ZnO/AC, [Fe/g-C_3N_4]/ZnO, ZnO/AC and ZnO samples 58
Figure 53: XPS spectra of (a) g-C_3N_4 and (b) Fe/g-C_3N_4 samples 60
Figure 54: XPS spectra of (a)AC and (b) [Fe/g-C_3N_4]/AC samples 62
Figure 55: XPS spectra of (a) ZnO, (b) ZnO/AC, (c) [Fe/g-C_3N_4]/ZnO and (d) [Fe/g-C_3N_4]/ZnO/AC samples 66
Figure 56: Visual observations of degradation of azo dye RB5 at definite time interval 67
Figure 57: Degradation curves of RB5 (a) C/C_0 vs time and (b) removal % vs time 68
Figure 58: Expected mechanism of ternary composite in degrading RB5 dye in photocatalysis (generated by AI) 70
Figure 59: Pseudo-first-order kinetic of ternary composite after (a) 8 h and (b) 2 h 72

List of tables

Table 1: Some names and uses of azo dyes 2
Table 2: Textural properties of samples 50
Table 3: Zeta potential of the samples 54
Table 4: Band gap of all samples 55
Table 5: Synergistic role of each component in ternary composite 70
Table 6: Kinetics data 71

Chapter 1: Introduction

1.1 Azo dyes

Azo dyes are the most used synthetic dyes known for their brilliance colors and extensive applications across various industries. These dyes contain a common structural unit but form a very diverse family and their importance may increase in future due to their easy uses, chemical stability and cheapness. Usually, these types of dyes are synthesized using diazotization and coupling reaction methods [1]. Azo dyes represent over 60% of total commercial dyes production with around 70% of dyes used in industrial applications [1]. Common uses of azo dyes include leather, paper, textile, food, pharmaceuticals and cosmetics industries. Specifically, approximately 80% of azo dye is utilized in textile dyeing process [2].

In terms of definition, azo dyes are those synthetic dyes which have one or more azo linkages (–N=N–) connecting the aromatic rings. Their general structure is R_1–N=N–R_2, where R_1 and R_2 are typically benzene, naphthalene or heterocyclic groups along with auxochromes such as –OH, $–NH_2$, $–SO_3H$, and –COOH which imparts color and solubility [1-3]. A common chemical structure of an azo dye is shown in Figure 1.

Azo dyes are commonly classified following:

- *By number of azo groups:* monoazo, disazo, trisazo and polyazo [1,2].
- *By application (textile):* acid, reactive, direct, disperse, vat and basic dyes [4].
- *By ionic character:* anionic (e.g., acid, reactive, direct), cationic and non-ionic; also classified based on hydrophobic or hydrophilic nature [3,5].

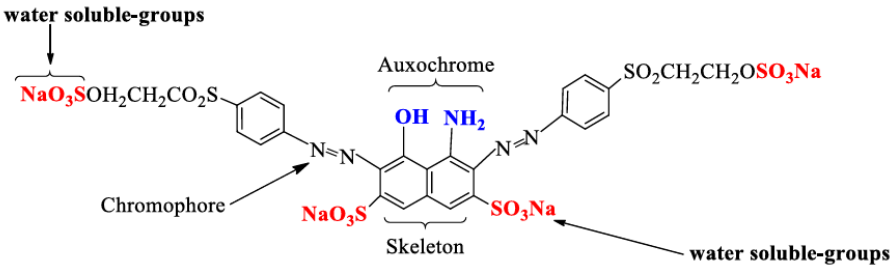

Figure 1: Chemical structure of an azo dye

Some names of commonly used azo dyes and their application along with their structure are shown in Table 1 and Figure 2.

Table 1: Some names and uses of azo dyes

Azo dye name / type	Uses
Tartrazine, Sunset Yellow, Allura Red, Amaranth etc.	Food, drinks, pharmaceuticals etc. [3]
Congo Red, Methyl Orange, Reactive Black 5, Orange II, Methyl Red etc.	Textile, fabrics and wastewater model dyes etc. [5]
Heterocyclic azo dye (pyrimidine, thiadiazole, quinoline based) etc.	High-fastness textile dyes, sensors, solar cells and bioactive agents etc. [4]

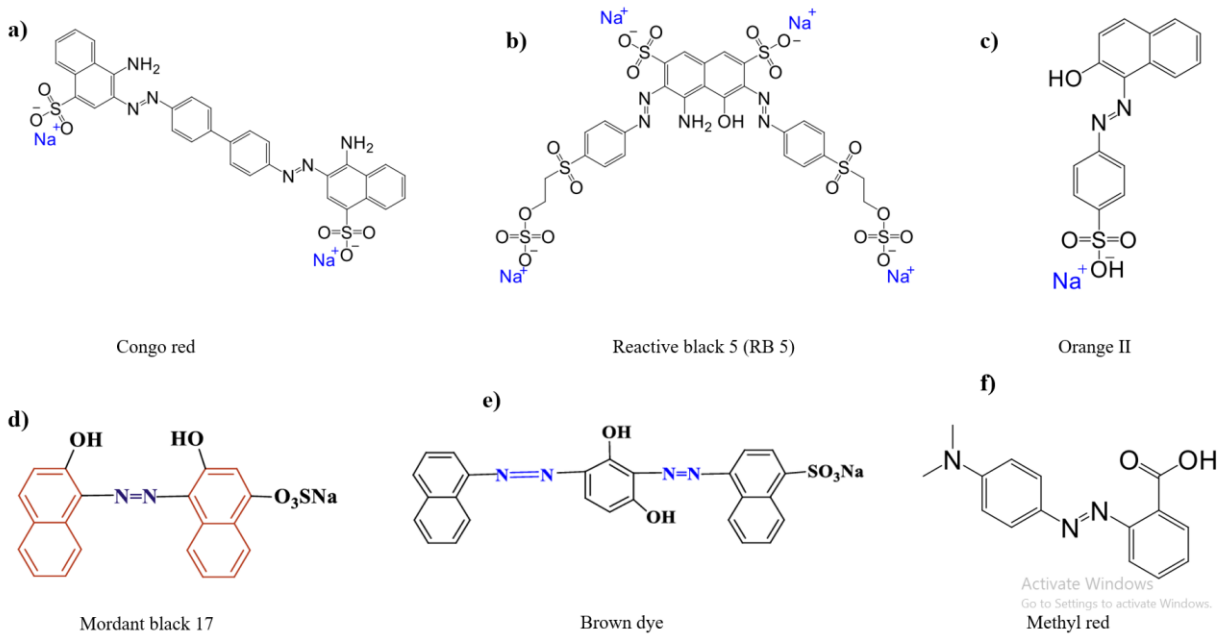

Figure 2: Common azo dyes names and structures [1,5]

In this study, reactive black 5 (RB5) azo dye (Figure 2(b)) will be used. It is an anionic azo dye that has molecular weight equal to 991.8 g/mol

1.2 Water pollution and environmental impact caused by azo dyes

It is predicted that approximately 10-15% of dyes used during textile dyeing processes fail to bind to fibers and are consequently released into the environment [2]. Many textile industries discharge untreated dye-containing wastewater rich in colored compounds, particularly azo dyes, which constitute a major global source of persistent and toxic water pollution [6].

These dye laden effluents are commonly released into natural water bodies, including rivers, coastal areas and groundwater systems (Figure 3). As a result, a significant fraction of industrial wastewater worldwide contains high concentrations of azo dyes, which are regarded as major xenobiotic pollutants due to their harmful effects on aquatic ecosystems [7, 8].

Figure 3: Water pollution caused by azo dyes [9]

The direct release of azo dye-contaminated water into environments can also disrupt soil ecosystems. These dyes may migrate into agricultural lands, where they can enter the food chain and ultimately accumulate in the human body as illustrated in Figure 4.

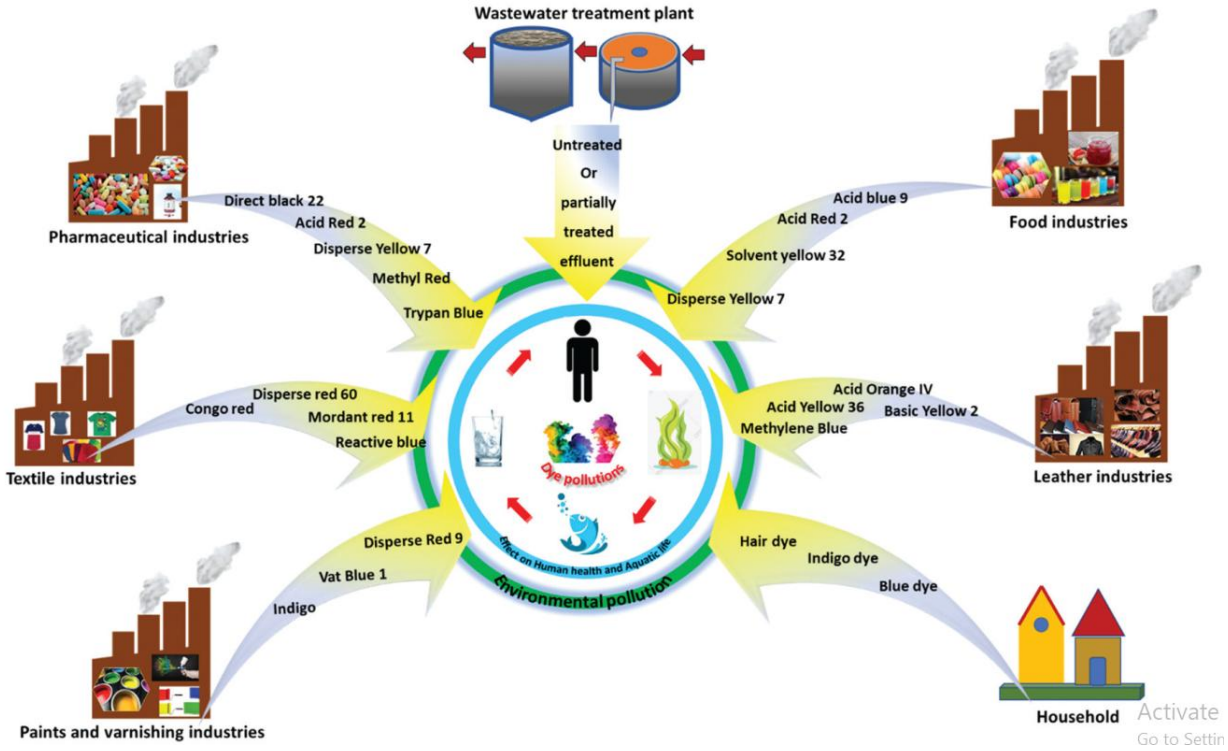

Figure 4: Toxic effect of azo dyes in ecosystem [10]

Azo dyes are characterized by high chemical stability and strong resistance to biodegradation because of their complex molecular structures. As a result, they can remain in the environment for extended periods after discharge, leading to both immediate and long-term environmental impacts. Their low cost, ease of application and vibrant coloration have made azo dyes extensively used in the textile industry, which in turn has intensified environmental contamination through the continuous release of dye-containing effluents into aquatic environments [11,12].

Certain azo dyes, particularly those containing nitro functional groups, are considered mutagenic and their breakdown products may generate hazardous aromatic amines such as 1,4-phenylenediamine and o-tolidine [13]. The accumulation of azo dyes in wastewater also contributes to increased biological oxygen demand (BOD) and chemical oxygen demand (COD), while simultaneously reducing light penetration in water bodies. This inhibits photosynthetic activity, disturbs *pH* conditions and alters the natural balance of organic and inorganic constituents within aquatic ecosystems [14]. Furthermore, owing to their automatic and xenobiotic nature, azo dyes are widely recognized as toxic and potentially carcinogenic substances that may adversely affect human health, including the reproductive and central nervous systems [15].

1.3 Wastewater treatment techniques to remove azo dyes

The removal of dyes from industrial effluents is considered both challenging and costly because dye molecules possess complex automatic structures that exhibit strong resistance to light, heat, oxidation and biodegradation [16]. Given the serious environmental impacts associated with azo dye contamination, effective wastewater treatment processes involving decolorization and detoxification are essential prior to the discharge of textile effluents into natural water bodies [17]. A variety of biological, physical, and chemical techniques (Figure 5 (a)) have been employed for the treatment of dye-containing wastewater, including coagulation/flocculation [18], membrane filtration technologies [19], enzymatic degradation [20], iron exchange [14], electrodialysis [14] and electrochemical methods [14]. Although these approaches can achieve high dye removal efficiencies, their practical implementation is often limited by high operational expenses, lengthy treatment duration and complex processing requirements, particularly for large scale applications [21]. In addition, several of these methods generate substantial amounts of sludge or produce secondary toxic by-products that require additional treatment, thereby increasing overall treatment costs and reducing economic feasibility [22]. Chemical oxidation processes, especially electrochemical treatments, also face limitations due to their high energy consumption, extensive chemical usage and the need for specialized equipment design [23].

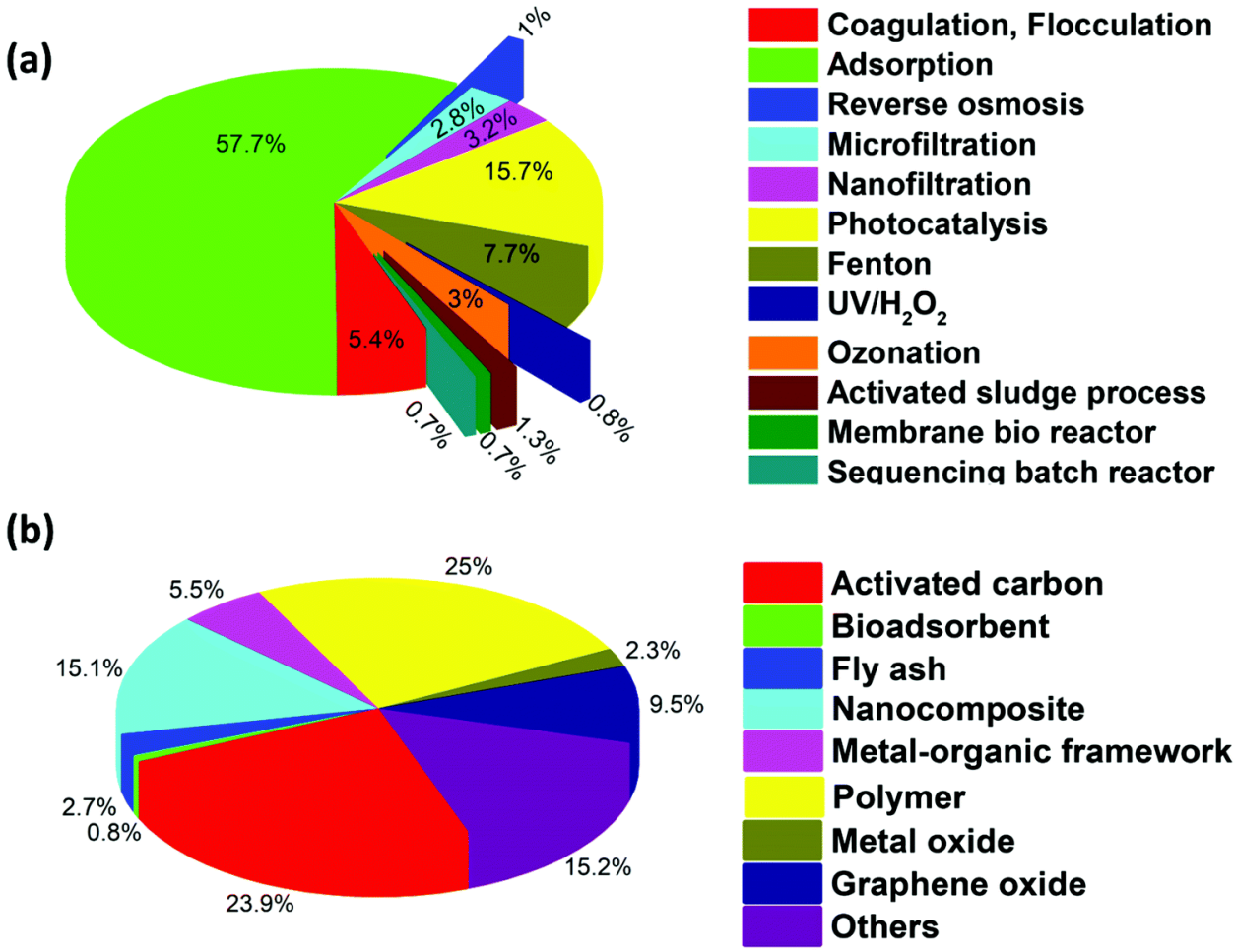

Figure 5: Pie-chart showing the percentage of literature available on dye removal for (a) various physico-chemical and biological techniques and (b) Adsorption techniques using different adsorbents [10].

Conventional biological treatment methods, such as those utilizing bacteria, fungi, algae and yeast are generally less effective for azo dye removal because synthetic dye possesses high chemical stability and resistance to biodegradation [14, 15]. Furthermore, biological processes are often time intensive and may not be sufficiently efficient for training large volumes of contaminated wastewater. Among the various wastewater treatment technologies discussed above, due to its low operational cost, simple design, flexibility, ease of operation, and relative tolerance toward toxic pollutants, adsorption process has become a highly efficient and commonly used technique [24, 25]. The growing significance of adsorption in dye removal is further reflected in the large proportion of published research focused on adsorption-based techniques, as illustrated in Figure 5 (b).

In addition to adsorption, over the past decade advanced oxidation processes (AOPs) have attracted significant interest as promising alternatives for wastewater treatment. These processes are particularly attractive because of their capability to effectively degrade and mineralize dye molecules in aquatic environments [12]. The following sections provide a more detailed discussion of both important water treatment approaches.

1.3.1 Adsorption process

Adsorption is one of the most employed techniques for the treatments and purification of industrial wastewater because of its cost effectiveness, operational simplicity and adaptability. This method is extensively applied in industries such as textiles, dyeing, lather, cosmetics, plastics, food processing and paper manufacturing, where efficient water treatment is essential. Adsorption can be defined as a mass transfer phenomenon in which dissolved substances present in an aqueous solution accumulate selectively on the surface of solid material. More specifically, it involves the diffusion and attachment of atoms, molecules and ions onto the surface of solid particles. The adhesion occurs due to the presence of unbalanced attractive forces between the solid surface and the contaminant species (Figure 6) [26]. In an adsorption process, the solid material that attracts and retains the molecules is referred to as the adsorbent, while the substances being retained on the surface are known as adsorbates. The overall adsorption interaction may be represented by the following equilibrium expression, where A denotes the adsorbate, B the adsorbent and AB the resulting adsorbed complex [14]:

$$A + B \rightleftharpoons AB \ldots\ldots\ldots\ldots (1.1)$$

Usually there are two main types of adsorptions physical adsorption (physisorption) and chemical adsorption (chemisorption) [2, 26]. Chemisorption refers to the attachment of particles onto the solid surface through the formation of chemical bonds such as ionic, covalent and metallic interactions [27]. In contrast, physisorption involves the attachment of molecules to the surface through weaker physical interactions, mainly van der Waals forces [26]. A key distinction between both mechanisms lies in the strength and nature of the bonding, with chemisorption involving much stronger and more specific interactions than physisorption. The efficiency of adsorption processes is influenced by several parameters, including the properties of the aqueous medium, the nature of the adsorbate, the characteristics of the adsorbent, the chemical structure of the pollutants, operating conditions and aspects such as contaminant separation and adsorbent regeneration [26, 27]. For dye-contaminated wastewater, key operational parameters such as initial dye concentration, *pH*, temperature, adsorbent dosage, and contact time play a crucial role in determining the overall removal efficiency [10].

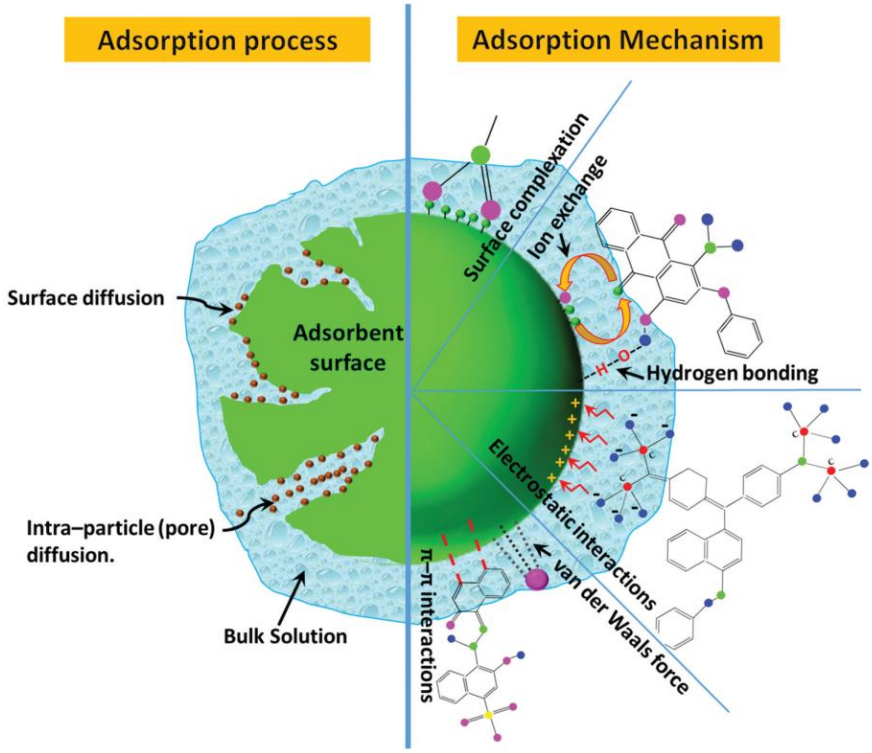

Figure 6: Mechanisms of adsorption process [10].

Regarding adsorbent materials, a wide range of substances has been explored for the dye removal from wastewater. These include bio-sorbents, carbon-based nanomaterials, transition metal oxides, clay-based materials, metal-organic frameworks (MOFs) and polymer-based adsorbents, as illustrated in Figure 7.

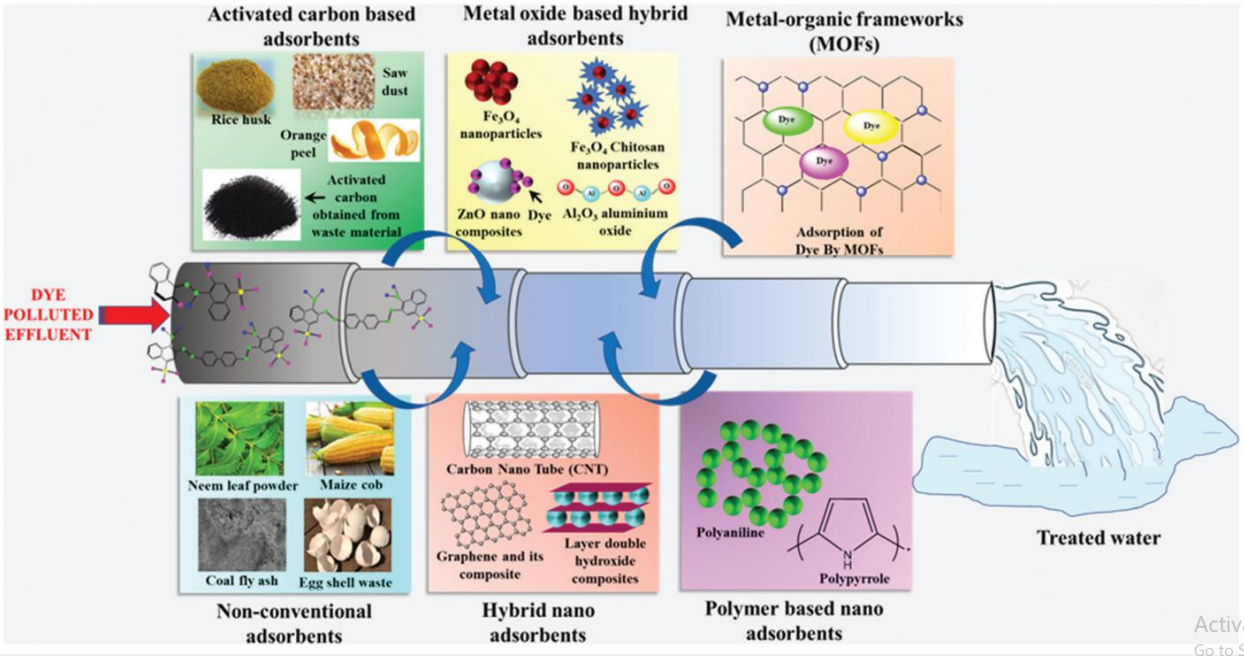

Figure 7: Application of different adsorbent materials in treating dyeing polluted water [10]

In recent years, soil-based clay materials have gained increasing attention as alternatives to chemically available adsorbents, due to their low cost, abundance, non-toxic nature, relatively high surface area and strong ion-exchange capabilities [28, 29]. In this work, clay materials are examined in detail, including their classification, structural characteristics and common applications. Special emphasis is placed on halloysite nano clay and clay-based composites, particularly their use as adsorbent materials and support matrix for the treatment of synthetic azo dye solutions.

1.3.1.1 Clay materials and Halloysite nano clay adsorbent materials

Clay is a naturally occurring material that exhibits soft and plastic behavior when wet but becomes rigid upon heating or calcination. Clay materials are classified as hydrous layer aluminosilicates and constitute an important group within the phyllosilicate family. They typically consist of very fine particles, with dimensions ranging from less than 2 mm up to about 4 mm in at least one direction [30]. A wide variety of clays exist (Figure 8), including ceramic clays, paper clays, earthenware and stoneware clays, ball clays fire clays, kaolin, bentonite, bleaching earth, fuller's earth, China clay, common clay, flint clay, refractory clay, laponite and nano clays, among others [31].

Structurally, clay materials are composed of stacked tetrahedral (T) and octahedral (O) sheets, which form either 1:1 (T–O) or 2:1 (T–O–T) layered arrangements, as illustrated in Figure 9. These layers are built from fundamental structural units: the silicon-oxygen tetrahedron $(Si_2O_5)^{2-}$ and the aluminum octahedral (gibbsite-like) sheet. In the tetrahedral sheet, each tetrahedron shares three of its four oxygen atoms with neighboring units, forming a hexagonal network with basal oxygens like together while apical oxygens extend upward or downward. The octahedral sheet consists of edge-sharing octahedra formed by oxygen and hydroxyl groups, with central cations such as Al^{3+}, Mg^{2+}, or Fe^{2+}. These octahedra are also arranged in a hexagonal pattern, while the tetrahedral framework is typically coordinated by cations such as Al^{3+}, Fe^{3+}, or Si^{4+} [32].

Clay materials, which form the primary constituents of natural clays, are generated in aqueous environments and include several major types such as montmorillonite, halloysite, vermiculite, kaolinite, illite, chlorite, sepiolite, and palygorskite [30].

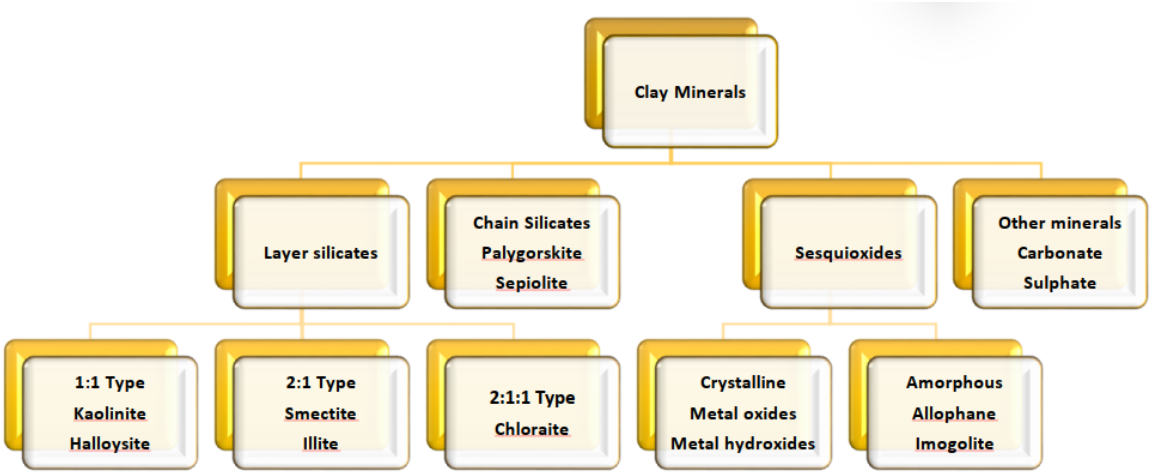

Figure 8: Classification of clay minerals [30]

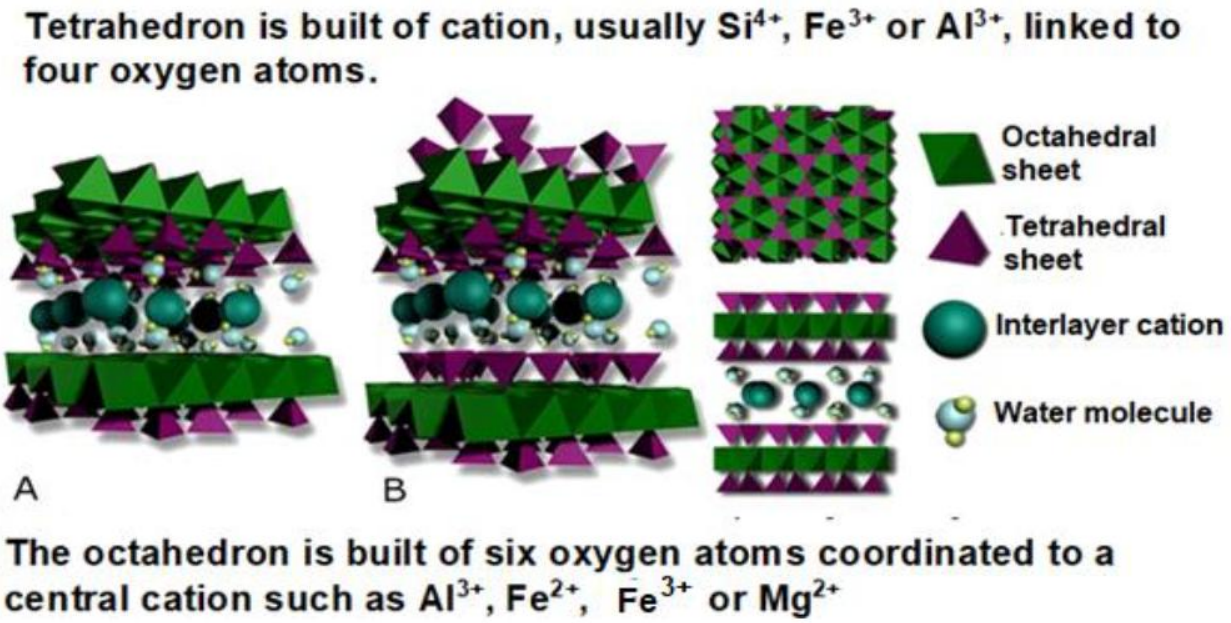

Figure 9: Two structural sheets of clay minerals [30]

A wide range of clay types and clay minerals are available, each with specific industrial applications, as illustrated in Figure 10. Clay minerals are considered environmentally friendly materials due to their low cost, natural abundance and generally non-toxic nature. Their suitability for environmental applications is largely attributed to their high specific surface area, significant porosity, surface charge characteristics and the presence of various surface functional groups. These features make them effective as adsorbents, flocculants and filtration media [33, 34]. In some cases, clay has been reported to exhibit adsorption capacities that can exceed those of activated carbon under comparable conditions of temperature and *pH* [35].

The adsorption and desorption behavior of organic compounds on clay surfaces is mainly governed by interfacial properties of clay minerals as well as the chemical nature of the adsorbate molecules [36]. Because clay surfaces typically carry a net negative charge, they show strong affinity for positively charged species, particularly cationic dyes and heavy metal ions, resulting in high adsorption efficiency for these contaminants.

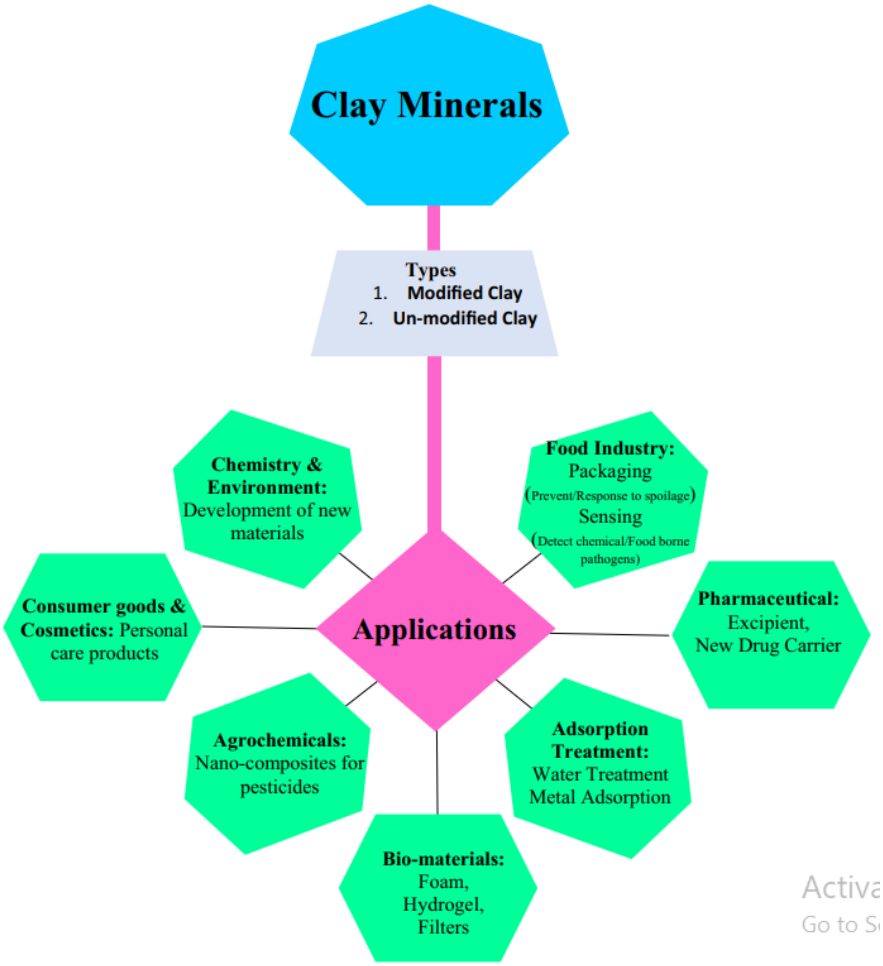

Figure 10: Applications of clay minerals [37]

1.3.1.2 Halloysite nano clay

Halloysite is a clay mineral belonging to the kaolin group which also includes kaolinite, dickite and nacrite [38]. It shares many similarities with kaolinite, in terms of structure, composition and origin. Both are dioctahedral 1:1 layered aluminosilicates and commonly occur together as hydrated aluminium silicate minerals [39]. Although halloysite has the same ideal chemical composition as kaolinite, it contains a higher amount of water. This is because its structural layers are separated by a single layer of water molecules, as shown in Figure 11. Halloysite exist in two main forms: a hydrated form with a basal spacing of approximately 10 Å, represented by the formula $Al_2Si_2O_5(OH)_4 \cdot 2H_2O$ and an anhydrous form with a reduced interlayer spacing of about 7 Å, represented by $Al_2Si_2O_5(OH)_4$ [39]. Halloysite typically forms through hydrothermal alteration of rocks or via surface weathering processes [40]. In nature, it can occur in various morphologies, including tubular platy or spherical structures, depending on geological conditions, location and crystallization pathways. Among these, nanotubular morphology (Figure 12) is the most notable and widely studied [41]. This tubular structure arises from the rolling of layered sheets, where the silicon- oxygen tetrahedral layer forms the outer surface and the aluminum- oxygen octahedral layer forms the inner surface. These layers are separated by a monomolecular layer of interlayer water [41].

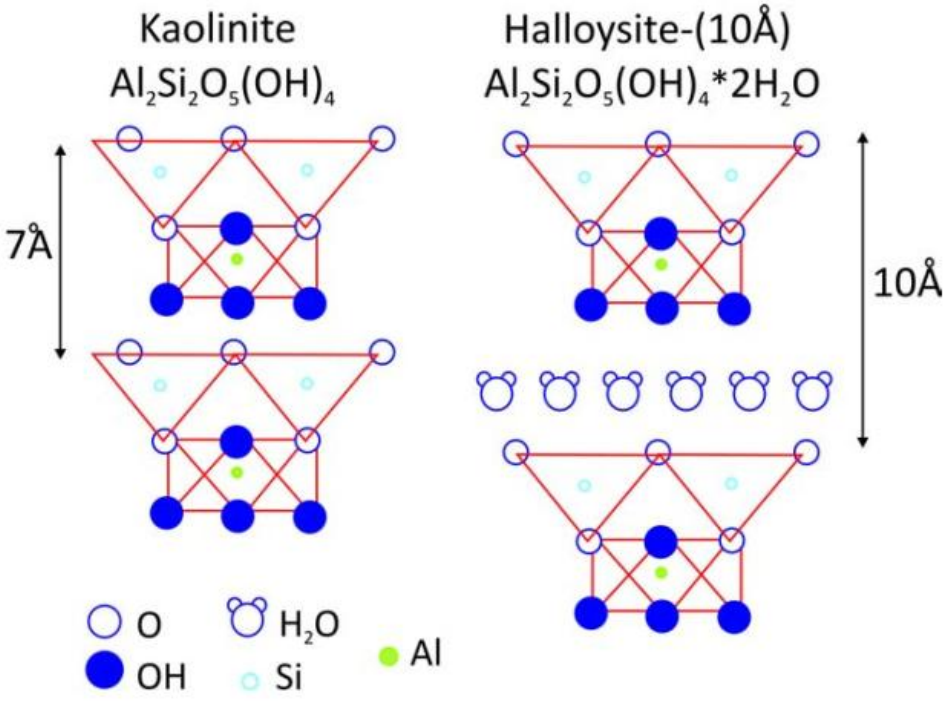

Figure 11: Structure of kaolinite and Halloysite clay [39]

Due to its structural and compositional variations, halloysite has been referred to by different names in the literature, including halloysite, meta halloysite, hydrated halloysite and endellite [40]. There is a huge application of halloysite clay [39], some are mentioned below:

- Drug delivery and controlled release systems
- Green nanotechnology applications
- Use as additives in polymers, plastics and paints.
- In cosmetic and personal care products.
- Wound healing and burning care materials.
- As antimicrobial packaging films (ex. ZnO-loaded HNs).
- Capture of tumor cells.
- Uses in corrosion protection coatings.
- Use as adsorbent materials for pollutants and contaminants in water treatment.
- Carrier for hydrophobic and hydrophilic active agents.
- Skin cleansing and moisturizing applications.

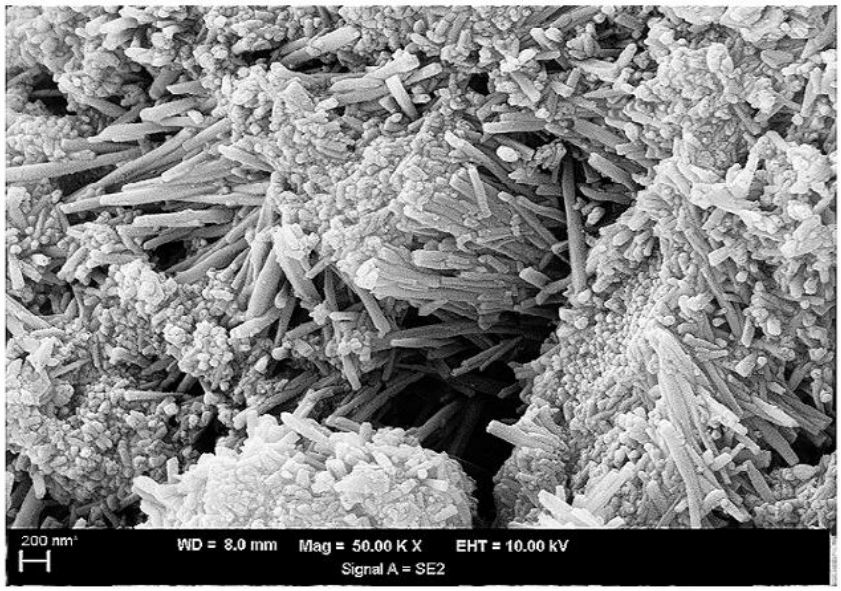

Figure 12: Tubular structure of halloysite clay [41]

In the present study, raw halloysite nano clay was subjected to both thermal and acid treatments to produce activated halloysite clay (AC). This modified material was then employed as an adsorbent and as a photocatalyst -supporting materials for the removal of Reactive Black 5 dye from synthetic aqueous solutions. The adsorption of Reactive Black 5 (RB5) onto acid activated halloysite is governed by multiple mechanisms, including electrostatic attraction, hydrogen bonding, pore diffusion and π–π interactions shown (Figure 13). Acid activation improves the adsorption efficiency by enlarging the specific surface area, increasing pore accessibility and generating additional active hydroxyl sites that can interact with anionic dye molecules [42].

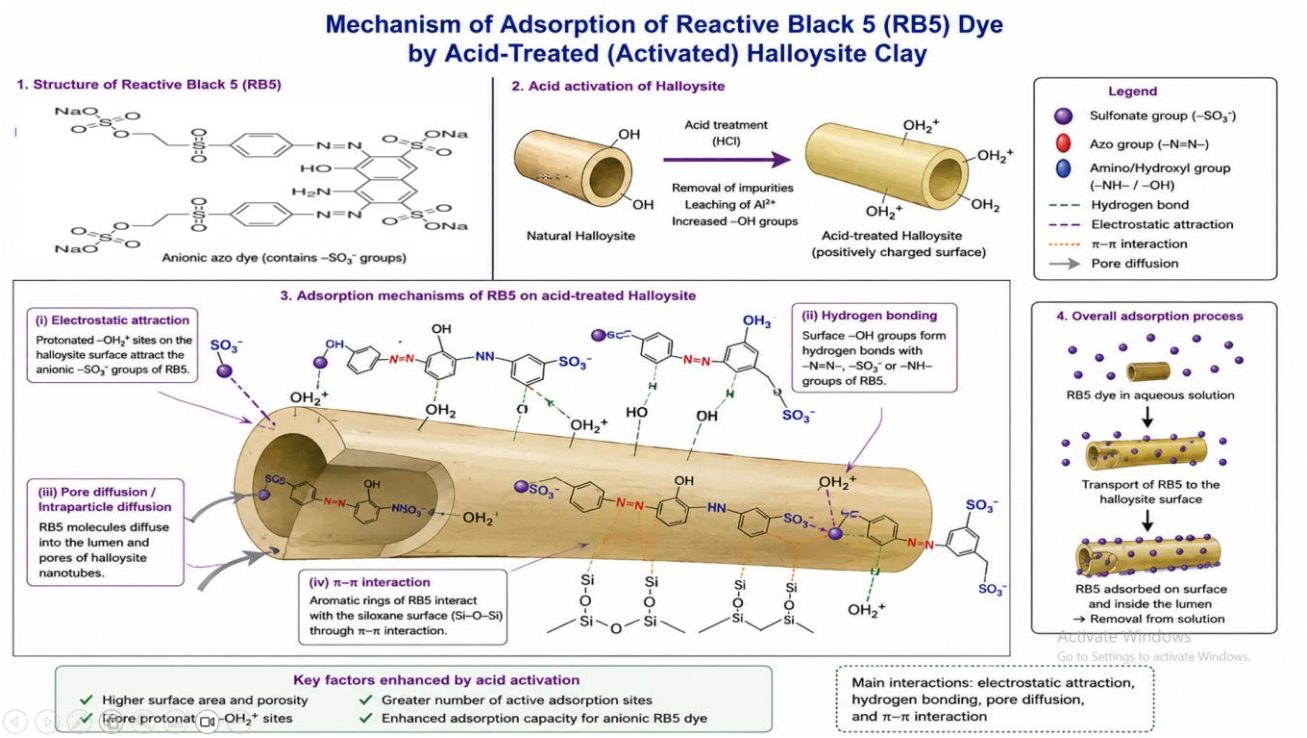

Figure 13: Adsorption mechanisms of RB5 dye by activated halloysite clay (AC) [generated by AI]

During acid treatment, hydroxyl groups on halloysite become protonated, resulting in the formation of positively changed adsorption site on the clay surface:

$$\text{Halloysite–OH} + H^+ \rightarrow \text{Halloysite–OH}_2^+ \ldots\ldots\ldots\ldots\ldots (1.2)$$

Since, RB5 is an anionic dye containing sulfonate groups (RB5–SO_3^-), these negatively charged functional groups are strongly attracted to positively charged protonated sites on halloysite through electrostatic interactions.

$$\text{Halloysite–OH}_2^+ + \text{RB5–SO}_3^- \rightarrow \text{Halloysite–OH}_2^+\cdots\text{SO}_3^-\text{–RB5} \ldots\ldots. (1.3)$$

In addition to electrostatic forces, hydrogen bonding also contributes to adsorption. The hydroxyl groups of halloysite can interact with nitrogen and oxygen containing functional groups in RB5, forming hydrogen bonds such as:

$$\text{Halloysite–OH}\cdots\text{N=N}\cdots\text{RB5 or Halloysite–OH}\cdots\text{O–SO}_3^-\cdots\text{RB5} \ldots\ldots (1.4)$$

Furthermore, π–π interactions between aromatic rings of RB5 and the siloxane surface of halloysite provide additional stabilization to the adsorbed dye molecules:

$$\pi_{\text{RB5}}\cdots\pi_{\text{Halloysite}} \ldots\ldots\ldots (1.5)$$

Reactive Black 5 possesses molecular dimensions of approximately 2.5-3.0 nm × 0.8-1.2 nm, which are considerably smaller than the inner lumen diameter of halloysite nanotubes (10-100 nm) [41,43]. Therefore, pore diffusion plays an important role in the overall adsorption process as RB5 molecules diffuse into the nanotube lumen, mesopores and surface cavities of halloysite before reaching equilibrium.

1.3.2 Advanced Oxidation Processes (AOP)

Originally, introduced in the 1980s for potable water treatments, AOPs are defined as oxidation processes that generate hydroxyl radicals (OH•) in sufficient quantities to achieve affective water purification. Over time, this concept has been expanded to include processing involving other reactive species, particularly sulfate radicals ($SO_4^{\bullet -}$) [44]. These treatment systems are based on the in-situ generation of reactive oxygen species (ROS), especially hydroxyl radicals, which are highly reactive and capable of non-selectively oxidizing complex organic pollutants into simpler and less harmful compounds [45]. The classification of AOPs in literature is generally based on the method used for hydroxyl radical generation, including different chemical, photochemical and electrochemical pathways [45]:

1. Fenton oxidation
2. Ozone oxidation
3. Electrochemical oxidation
4. Photocatalysis
5. Radiation
6. Sonolysis

The general reaction pathways involved in different AOPs are illustrated in Figure 14.

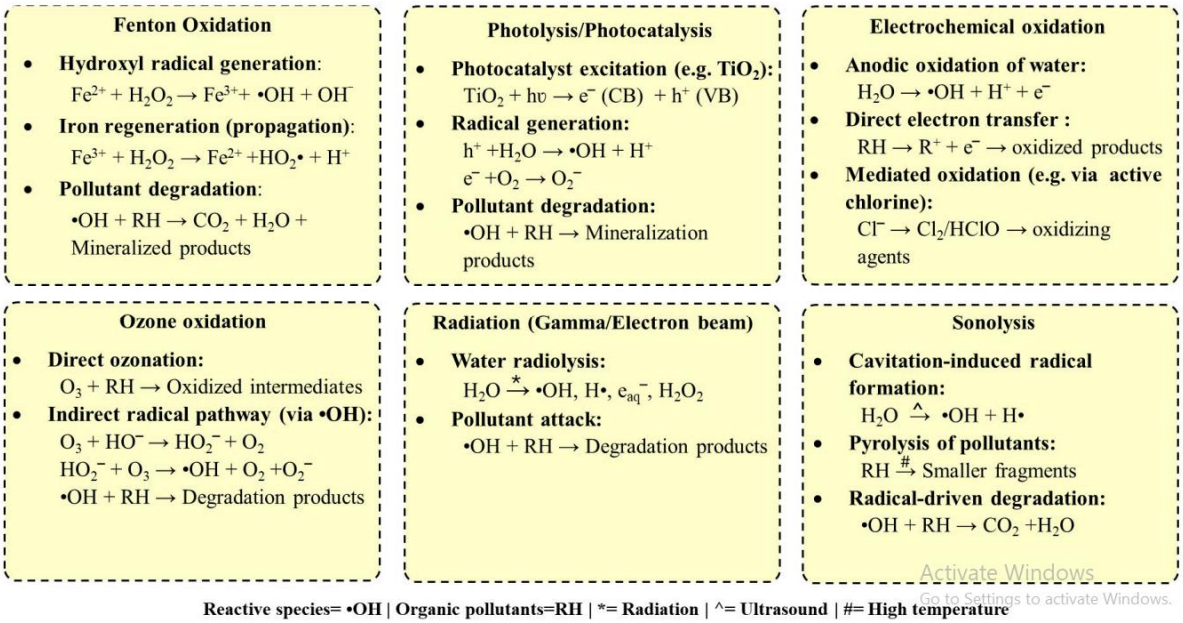

Figure 14: Reaction mechanisms of different AOPs [45]

Despite their high efficiency in removing contaminants, AOPs face several practical challenges. Many of the processes are energy intensive, which can remove their feasibility for large scale or continuous industrial applications due to high operational and environmental costs. In addition, intermediate degradation products may be formed during the oxidation processes, some of which can produce toxicity and therefore require additional treatment steps. Another important limitation is related to scalability. While AOPs often show excellent performance under controlled laboratory conditions, their efficiency may decrease in real wastewater systems. This reduction in performance is commonly attributed to the complexity of real effluents, mass transfer limitations and the deactivation of photocatalysts during operation [46].

1.4 Photocatalysis process

Photocatalysis has demonstrated strong potential in a wide range of environmental and energy applications, including CO_2 reduction, hydrogen (H_2) production, and wastewater treatment, making it promising green technology [47]. Photocatalysis is regarded as a highly efficient and cost-effective water treatment method because it combines renewable energy with semiconducting materials. Compared with other AOPs, it requires fewer chemical inputs, and therefore it is more economical and environmentally sustainable, unlike conventional AOPs that depend on costly oxidants such as hydrogen peroxide (H_2O_2) or ozone (O_3). Photocatalysis typically relies on naturally available oxygen as the primary oxidizing agent.

When semiconductor particles are exposed to light matching or exceeding their band gap energy, electrons from the valence band (VB) are excited to the conduction band (CB), leaving behind positive holes in the VB. These holes act as strong oxidizers, reacting with water to generate hydroxyl radicals (OH•). Simultaneously, the excited electrons in the CB reduce dissolved oxygen in water to produce superoxide radicals ($O_2^{\bullet -}$) [15]. Both OH• and $O_2^{\bullet -}$ are highly reactive species that attack and degrade organic pollutants, ultimately leading to their complete mineralization [12]. A schematic representation of this mechanism for dye degradation is shown in Figure 15. The heterogeneous photocatalytic process consists of five key steps [48]: (1) reactant transfer from the liquid to the photocatalyst surface; (2) reactant adsorption onto active sites (A* and B*); (3) surface reaction to form the product (AB); (4) product desorption from the surface; and (5) product diffusion back into the bulk liquid.

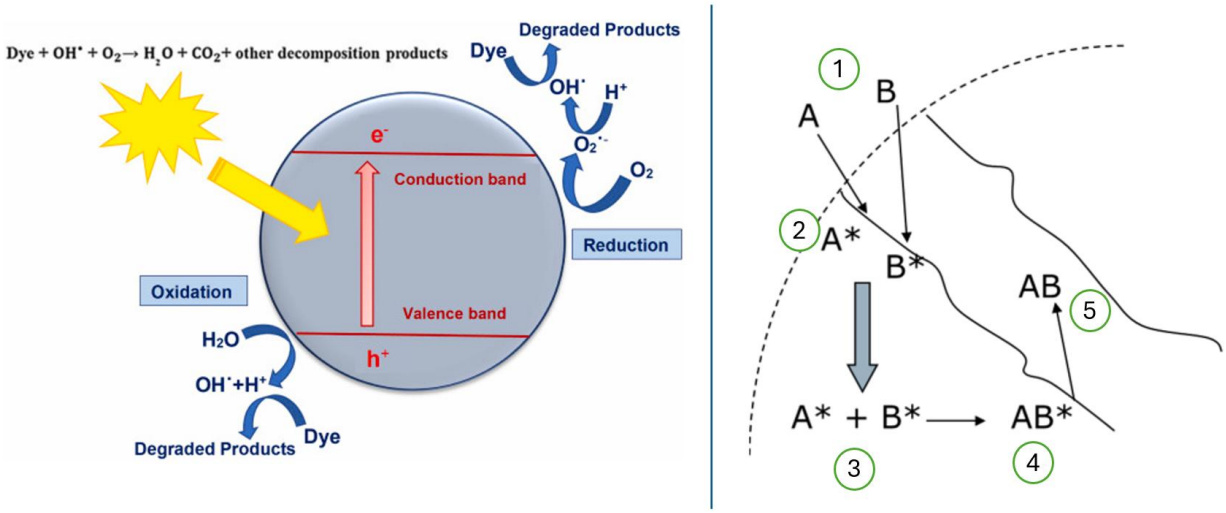

Figure 15: Mechanism of photocatalytic degradation of water pollutants [48]

Despite its advantages, photocatalysis also has several limitations. One major drawback is the reliance on UV light sources, which can be energy demanding and costly for large scale applications. In addition, photocatalytic efficiency can be significantly reduced in turbid or strongly colored wastewater, as these conditions hinder light penetration through absorption and scattering. The process may also require relatively long reaction times to achieve complete degradation of certain persistent pollutants [45]. Another important limitation is related to catalyst recovery. In most cases, photocatalysts are used in the form of suspended powders within slurry reactors. After treatment, these fine particles must be separated and recovered from the treated water, which adds an additional operational step and limits the practicality of photocatalysis for industrial scale applications [15]. A wide range of semiconducting materials, both undoped and doped, have been investigated for the treatment of azo-dyed contaminated water and wastewater. These include TiO_2, ZnO, SnO_2, WO_3, Fe_2O_3, and CdS, which have been studied under UV, visible and solar irradiation due to their favorable photocatalytic activity, light absorption properties, change carrier transport behavior, and relatively simple synthesis methods [15]. The present study focuses specifically on ZnO and ZnO-based composite photocatalysts for the degradation of azo dyes in synthetic aqueous solutions.

1.4.1 ZnO-based photocatalysis

Zinc oxide (ZnO), found naturally as zincite, is a white powder with low water solubility and is the second most abundant metal oxide after iron [49]. Zinc oxide nanoparticles (ZnO-NPs) are valued for their high chemical stability, broad light absorption, strong electrochemical coupling, and excellent photostability, making them useful in many technological and environmental applications [50]. ZnO has a hexagonal wurtzite structure with lattice parameters a = 0.325 nm and c = 0.521 nm, where each oxygen anion is tetrahedrally coordinated by four zinc cations, resulting in a non-centrosymmetric crystal structure (Figure 16) [51].

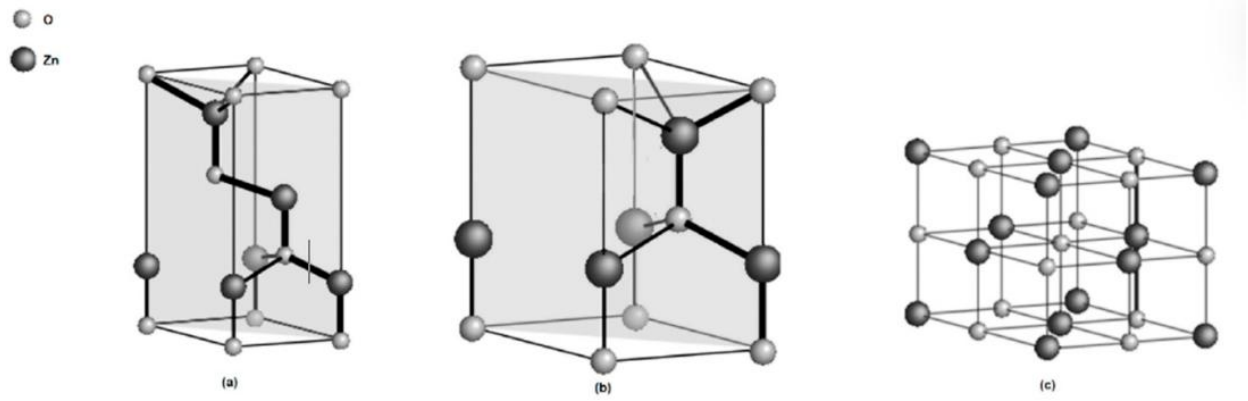

Figure 16: Crystal structure of ZnO (a) Zinc blende (b) wurtzite and (c) rock salt [51]

Due to their versatile properties, ZnO nanoparticles are used in cement, ceramics, glass, plastics, ointments, lubricants, adhesives, pigments, batteries, cosmetics, fire retardants, sunscreens, and dietary supplements (Figure 17) [51]. They can be synthesized via various including mechano-chemical methods, controlled precipitation, sol-gel processing, vapor transport techniques, chemical deposition, hydrothermal and solvothermal approaches, and microemulsion approaches (Figure 18) [52].

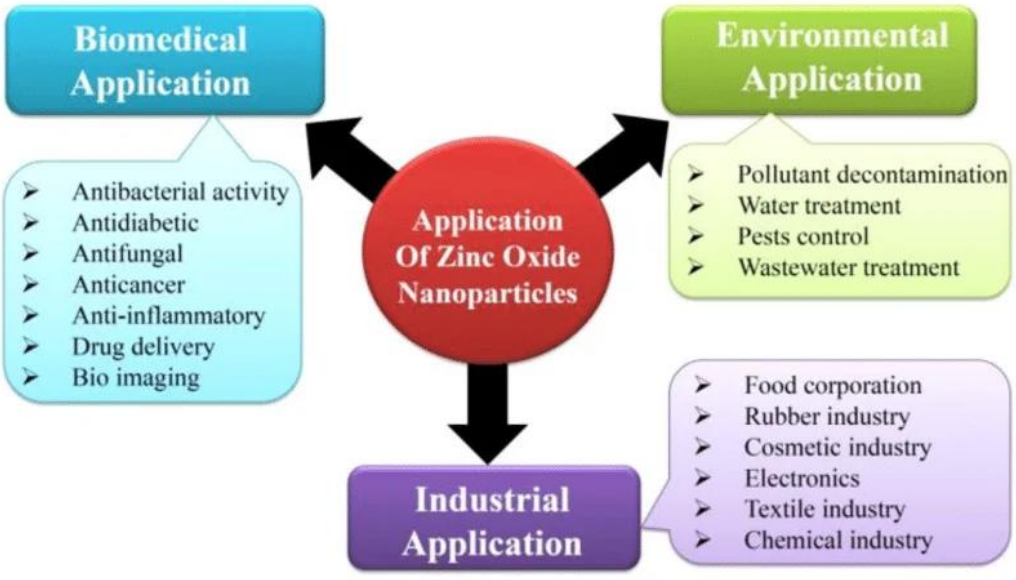

Figure 17: Applications of ZnO nanoparticles [53]

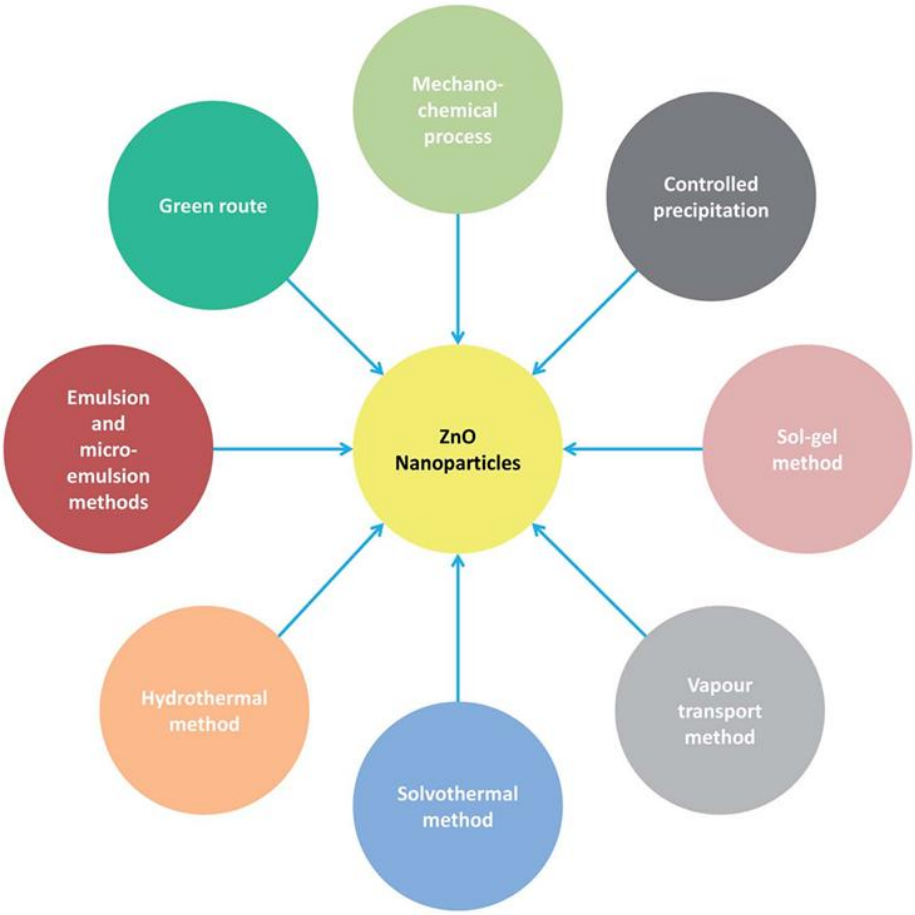

Figure 18: ZnO nanoparticles synthesis method [49]

ZnO is a semiconductor known for its strong electrical, optical, and photocatalytic properties. It has a wide bandgap of about 3.37 eV and a high exciton binding energy of 60 meV, contributing to excellent optical performance [54]. Additional advantages include high transparency, antimicrobial activity, high electron mobility, and good thermal/mechanical stability at room temperature. Strong room-temperature luminescence makes ZnO suitable for optoelectronic and photocatalytic applications [51]. With a wide direct bandgap of about 3.37 eV at room temperature, ZnO exhibits a UV absorption edge near 375 nm, making it highly effective for applications like UV photodetectors and photocatalytic pollutant degradation [54]. Recent studies show that ZnO nanoparticles possess strong photocatalytic performance for environmental remediation, especially in breaking down organic pollutants. This activity stems from their ability to absorb UV light and generate reactive oxygen species (ROS), such as hydroxyl radicals, which are key to degrading organic contaminants in water [54].

According to [55], the photocatalytic mechanism of ZnO proceeds through several sequential steps (Figure 19). Upon irradiation with light energy (hν) equal to or greater than the ZnO bandgap, electrons in the valence band (VB) are excited to the conduction band (CB), generating electron-hole pairs and leaving positively charged holes (h^+) in the VB.

$$ZnO + h\nu \rightarrow ZnO(e^- + h^+) \ldots\ldots\ldots (1.6)$$

Photogenerated electron–hole pairs in ZnO can recombine, lowering photocatalytic efficiency. However, carriers that avoid recombination migrate to the particle surface and drive redox reactions. Specifically, conduction band electrons react with dissolved oxygen to produce superoxide radicals.

$$e^- + O_2 \rightarrow \cdot O_2^- \ldots\ldots\ldots (1.7)$$

These superoxide radicals then undergo further protonation and reduction steps, eventually producing hydrogen peroxide (H_2O_2) and highly reactive hydroxyl radicals (•OH).

$$O_2^- + H^+ \rightarrow HO_2^{\cdot} \ldots\ldots\ldots\ldots\ldots (1.8)$$
$$HO_2^{\cdot} + HO_2^{\cdot} \rightarrow H_2O_2 + O_2 \ldots\ldots (1.9)$$
$$H_2O_2 + h\nu \rightarrow 2 \cdot OH \ldots\ldots\ldots\ldots (1.10)$$

Meanwhile, the photogenerated holes (h^+) in the valence band can oxidize water molecules or hydroxide ions on the catalyst surface, generating additional hydroxyl radicals (•OH).

$$H_2O + h^+ \rightarrow \cdot OH + H^+ \ldots\ldots (1.11)$$
$$OH^- + h^+ \rightarrow \cdot OH \ldots\ldots\ldots\ldots\ldots (1.12)$$

The hydroxyl radicals (•OH) generated in the photocatalytic system are highly reactive oxidants that attack and degrade organic pollutants. Through a series of intermediate reactions, they ultimately achieve complete mineralization of contaminants into harmless end products like carbon dioxide (CO_2) and water (H_2O).

$$OH + \text{Pollutant} \rightarrow \text{Intermediates} \rightarrow CO_2 + H_2O \ldots\ldots (1.13)$$

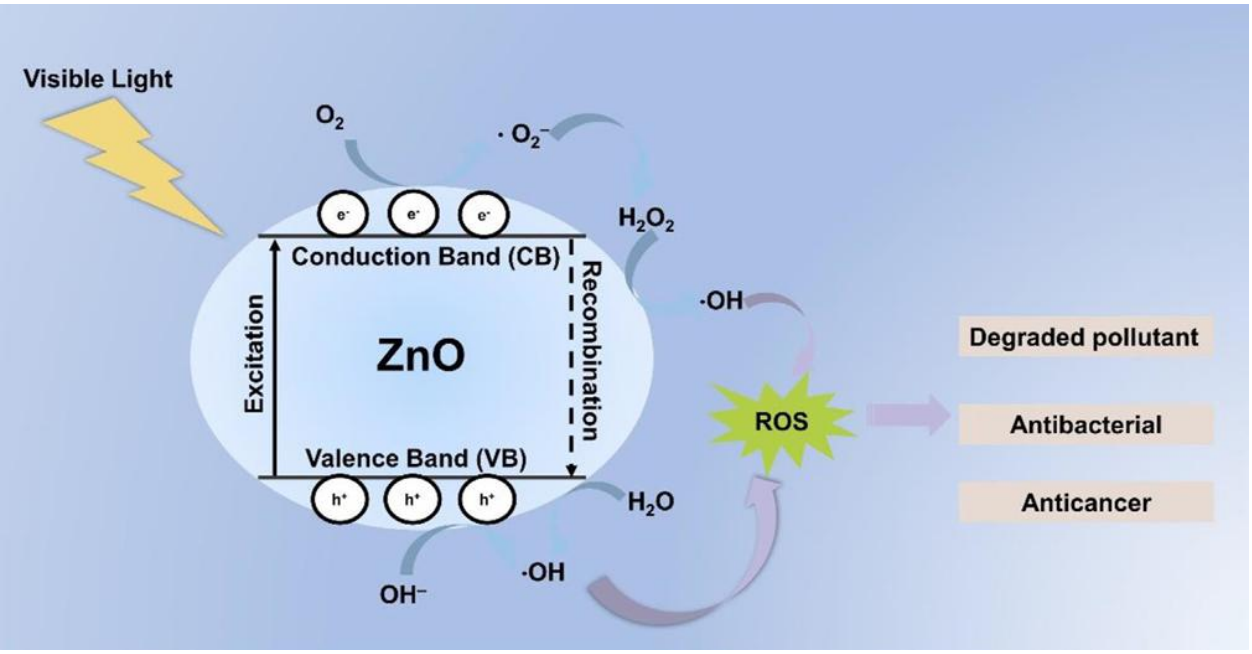

Figure 19: Photocatalytic mechanism of ZnO to degrade dye pollutant [55]

However, ZnO has intrinsic limitations that reduce its photocatalytic efficiency. Its wide band gap (3.37 eV) and high exciton binding energy (60 meV) restrict activation to UV light and promote rapid electron-hole recombination, confining light absorption to the UV region. Since only 4-5% of sunlight is UV, ZnO's solar utilization remains low, limiting practical applications [54,55]. Therefore, enhancing visible-light response and suppressing recombination are essential. Several modification strategies have been developed: (i) non-metal or metal doping (*e.g.* N, C, Fe, Ag) introduces impurity levels that narrow the band gap; (ii) heterojunction construction with narrow band gap semiconductors like CdS, $BiVO_4$, g-C_3N_4 enhances charge separation; (iii) surface modification with noble metals (Ag, Au) leverages localized surface plasmon resonance effects; (iv) defect engineering, particularly creating oxygen vacancies, also narrows the band gap and inhibits recombination [54, 55]. These modified ZnO photocatalysts show improved visible-light responsiveness, charge separation, and stability [55].

1.4.2 Graphitic carbon nitride (g-C_3N_4) and metal-doped g-C_3N_4 photocatalyst

Heterojunction systems using materials such as $BiVO_4$, g-C_3N_4, or CdS not only broaden the light absorption range but also enhance charge carrier separation, minimizing recombination losses. This synergistic interaction between the coupled semiconductors leads to improved overall photocatalytic performance [54].

Graphitic carbon nitride (g-C_3N_4) has gained significant global attention due to its unique structure and favorable optical properties [56]. It is a 2D, π-conjugated, metal-free polymeric semiconductor with a moderate band gap of about 2.7 eV [57]. With excellent chemical and thermal stability and an appropriate band structure, g-C_3N_4 has been widely explored for applications including sensing, supercapacitors, adsorption, organic synthesis, water splitting for hydrogen evolution, photocatalytic degradation, bioimaging, oxygen reduction, lithium-ion batteries, biofuel cells, lubrication, cancer therapy, and forward osmosis membrane additives [57]. Numerous synthesis routes have been developed to produce g-C_3N_4 with varying morphologies and electronic properties [57], including chemical vapor deposition (CVD), physical vapor deposition (PVD), solvothermal and ionothermal methods, single-step nitridation, solid-state reactions, sonochemical synthesis, and thermal condensation. Thermal polymerization of nitrogen-rich precursors (*e.g.* urea, melamine, cyanamide, dicyandiamide, thiourea) is most common due to its simplicity, low cost, and availability [57]. The formation proceeds via stepwise polymerization: cyanamide condenses into dicyandiamide and then melamine; further heating causes deammoniation and polycondensation to form melam, which transforms into melem; continued polymerization and rearrangement of melon finally yield g-C_3N_4 (Figure 20) [57].

However, the photocatalytic performances of g-C_3N_4 is limited by a low specific surface area, inefficient visible-light utilization, and rapid charge carrier recombination [58]. To overcome these drawbacks, metal doping can be used for example, Mn-doped g-C_3N_4 exhibits enhanced visible-light activity due to better carrier separation [58, 59]. Structurally, g-C_3N_4 consists of sp^2-hybridized C and N atoms forming a π-conjugated framework like graphite, with heptazine units containing nitrogen lone pairs that facilitate strong interactions with transition metal ions [58].

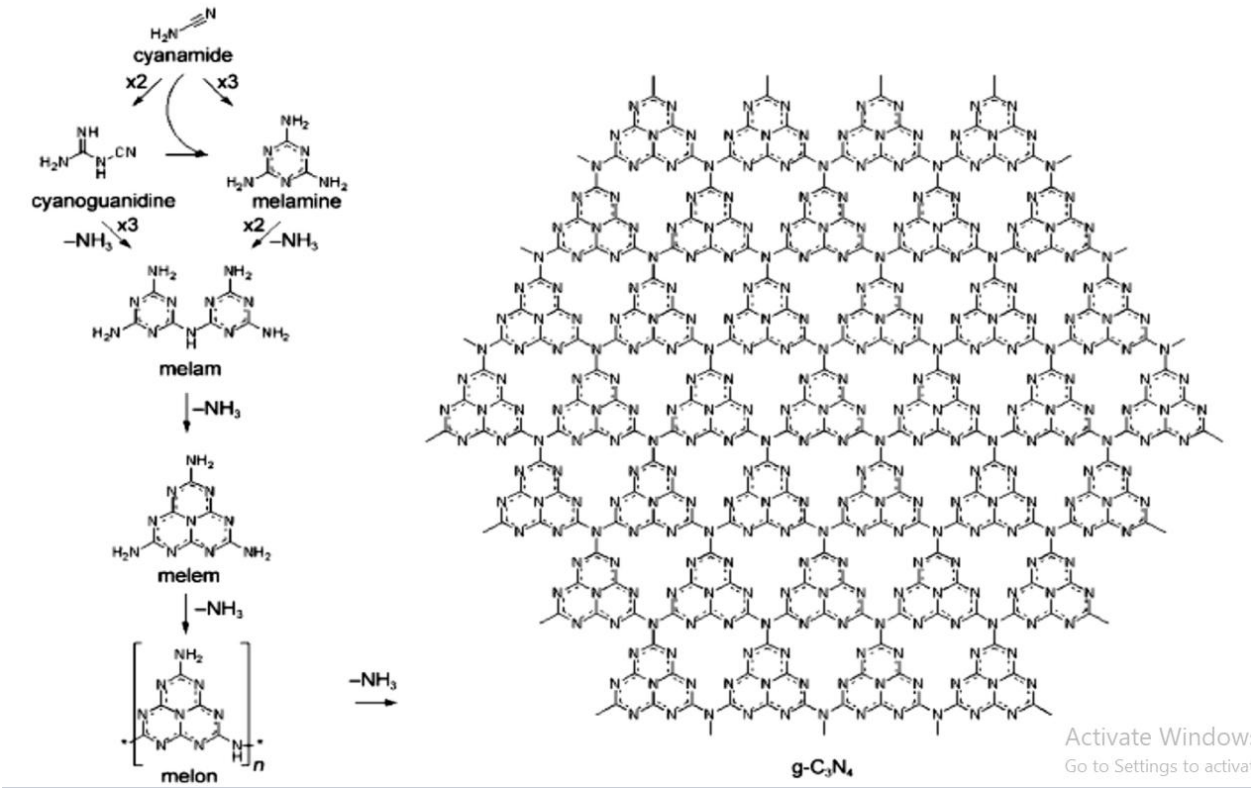

Figure 20: Synthesis route of g-C_3N_4 [57]

Doping approaches using Fe and Zn have also been reported in previous studies [58, 60]. However, in the study of [58], it is reported that compared with pristine g-C_3N_4, Fe (III)-modified g-C_3N_4 samples exhibited significantly improved photocatalytic activity, with the 2% Fe-loaded composite showing the highest efficiency. According to this study [58], the mechanism of Fe-gC_3N_4 is explained in Figure 21. Firstly, due to visible-light irradiation, electrons in g-C_3N_4 are excited from the valence band (VB) to the conduction band (CB), generating electron-hole pairs.

$$g - C_3N_4 + h\nu \rightarrow e^- + h^+ \ldots\ldots\ldots \text{(1.14)}$$

A fraction of the photogenerated electrons reduces Fe (III) to Fe (II), and the resulting Fe (II) species can then react with dissolved oxygen to generate superoxide radicals ($O_2^{\bullet-}$):

$$Fe^{3+} + e^- \rightarrow Fe^{2+} \ldots\ldots\ldots \text{(1.15)}$$

$$Fe^{2+} + O_2 \rightarrow \cdot O_2^- + Fe^{3+} \ldots\ldots\ldots \text{(1.16)}$$

$$O_2^-/\cdot OH/h^+ + RB5 \rightarrow CO_2 + H_2O + \text{byproducts} \ldots\ldots\ldots \text{(1.17)}$$

These processes enhance charge carrier separation and improve the utilization of visible light. The generated superoxide radicals ($O_2^{\bullet-}$) can further participate in subsequent reactions to form hydroxyl radicals (•OH). Together, these reactive oxygen species play a crucial role in the degradation of organic pollutants, ultimately converting them into harmless end products such as carbon dioxide (CO_2) and water (H_2O) [58].

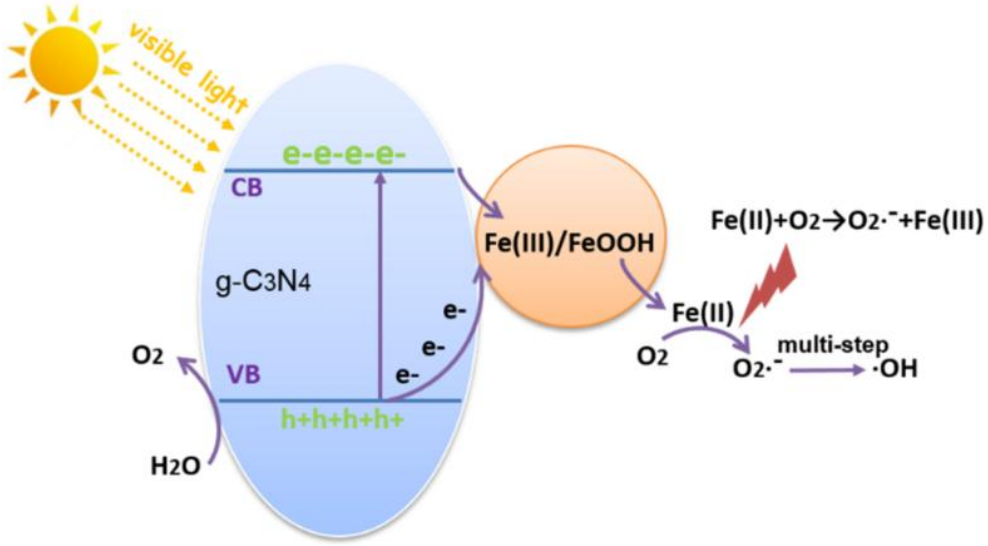

Figure 21: Photocatalytic mechanism of Fe/g-C_3N_4 samples [58]

1.5 Objectives of master thesis

The aim of this study is to address the textile water pollution caused by RB5 dye and to form suitable photocatalytic composite materials for the degradation of azo dye RB5. Therefore, the first objective is to synthesize activated clay (halloysite) from raw clay and prepare g-C_3N_4 semiconductor particles, followed by Fe doping to enhance their photocatalytic properties. Metal-organic framework (MOF)-based composites supported on activated clay, such as [Fe/g-C_3N_4]/AC, will be developed alongside ZnO nanoparticles and ZnO/AC composite materials. Furthermore, [Fe/g-C_3N_4]/ZnO binary heterojunctions and [Fe/g-C_3N_4]/ZnO/AC ternary composites will be synthesized to improve light harvesting and photocatalytic efficiency. Then the photocatalytic, optical, and surface properties of the pure and modified materials will be characterized using techniques such as XRD, SEM, DRS, XPS, Nitrogen adsorption-desorption, and zeta potential analysis. After that, the photocatalytic performance of the synthesized materials will be evaluated through the degradation of Reactive Black 5 (RB5) in synthetic wastewater. In addition, the degradation mechanisms and synergistic interactions among the composite components will be investigated. Finally, the degradation efficiency of RB5 and the reaction kinetics of the most effective photocatalysts will be assessed to determine their suitability for wastewater treatment applications.

In a nutshell, the novelty of this work is to overcome the limitations of pure ZnO in visible light performance by forming binary and ternary heterojunction composite materials like [Fe/g-C_3N_4]/ZnO and [Fe/g-C_3N_4]/ZnO/AC for enhancing the photocatalytic degradation of azo dye RB5 and establishing synergistic relationships among them.

Chapter 2: Materials and methods

2.1 Reagents and chemicals

A less hydrous form of halloysite is used whose formula is $Al_2Si_2O_5(OH)_4$ as the source of clay materials. The halloysite clay is commercially purchased. Then hydrochloric acid (HCl) is used for chemical activation of the clay. For the preparation of carbon graphitic nitride (g-C_3N_4), melamine ($C_3H_6N_6$) was used. $FeCl_3$, absolute ethanol, HCl and melamine were used for iron doped- carbon graphitic nitride (Fe/g-C_3N_4). ZnO was synthesized using zinc acetate dihydrate *i.e.* $Zn(CH_3CO_2)_2.2H_2O$ and NaOH.

2.2 Activation of halloysite

First 50 g of halloysite was put in the furnace heated at 800 °C for10 h (temperature rate = 10 °C/min). After heating, the sample was weighted again, and it was found to be equal to 42.65 g. Therefore, the percentage of mass loss (%) was calculated using the following formula:

$$\text{Mass Loss (\%)} = [\text{initial mass- final mass})/ \text{initial mass}] \times 100 \ldots\ldots\ldots \quad (2.1)$$

The mass loss of sample was equal to 15 % and the sample was named MH-800.

Then 30 g of MH-800 sample was taken in a round bottom flask and 230 ml HCl (6M) was added to it and heated at 120 °C for 5 h in a magnetic stirrer equipped with reflux condenser. The solution was to cool down to room temperature and excess acids were removed by syringe first and washed 5 times using a buchner-filtration process until *pH* was reached at 7. Then the filtered cake was put in the oven and heated at 105 °C for 24 h for drying. After, it was crushed and grinded. At last, it was calcinated in the furnace at 500 °C for 2 h (temperature rate = 10 °C/min). The sample was finally named MH-800-HCl (Figure 22).

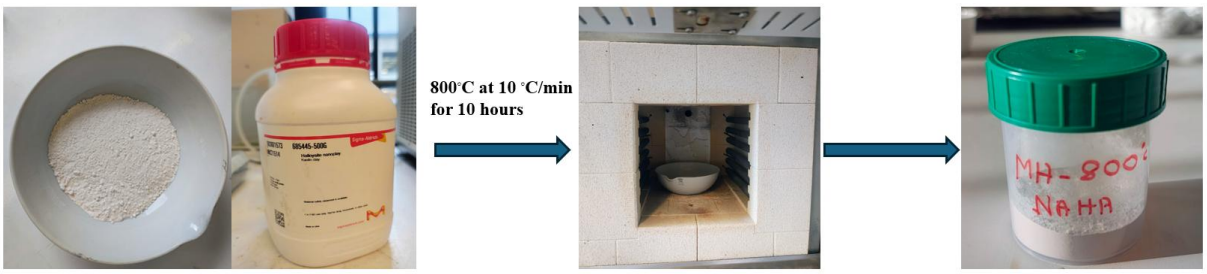

Raw halloysite | Raw halloysite in oven for calcination | Meta halloysite after calcination (thermal treatment)

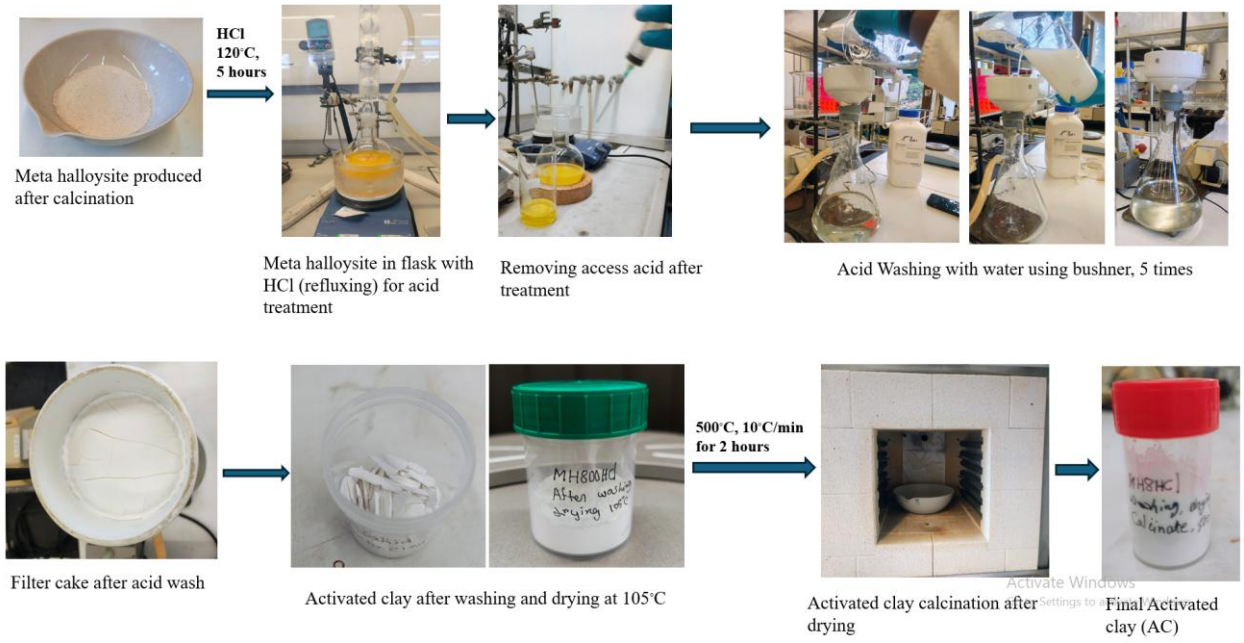

Figure 22: Synthesis of activated clay (AC)

2.3 Synthesis of carbon graphitic nitride (g-C_3N_4)

For the preparation of carbon graphitic nitride (g-C_3N_4), 10 g of melamine was calcinated in the furnace at 500 °C for 5 h (temperature rate = 10 °C/min). Then it was crushed and grinded and finally g-C_3N_4 was produced (Figure 23).

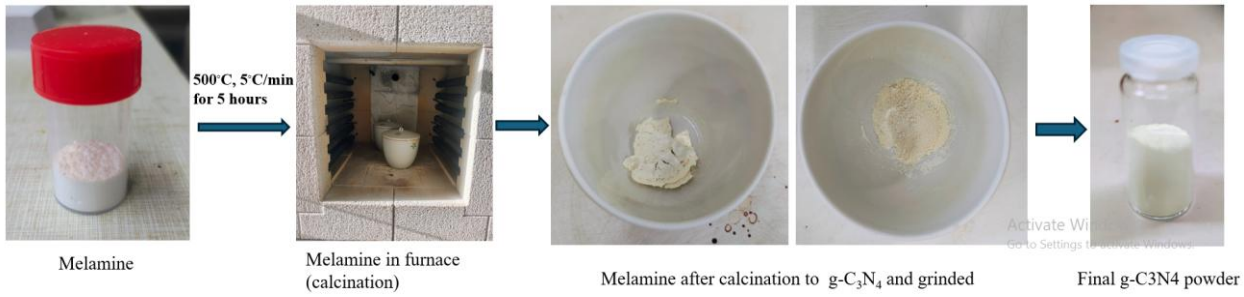

Figure 23: Synthesis of g-C_3N_4

2.4 Synthesis of iron doped-carbon graphitic nitride (Fe/g-C_3N_4)

First, 0.5 g of $FeCl_3$ was dissolved into 60 ml of absolute ethanol. Then 3 drops of HCl (10^{-2} M) were added and stirred properly. After that, 10 g of melamine was added to it, and the mixture was heated at 80 °C until ethanol evaporates completely. Then it was dried in the oven overnight and crushed. The crushed powder was calcinated in the furnace at 500 °C for 5 h (temperature rate = 5 °C/min). After calcination, it was grinded again and finally Fe/g-C_3N_4 sample was obtained (Figure 24).

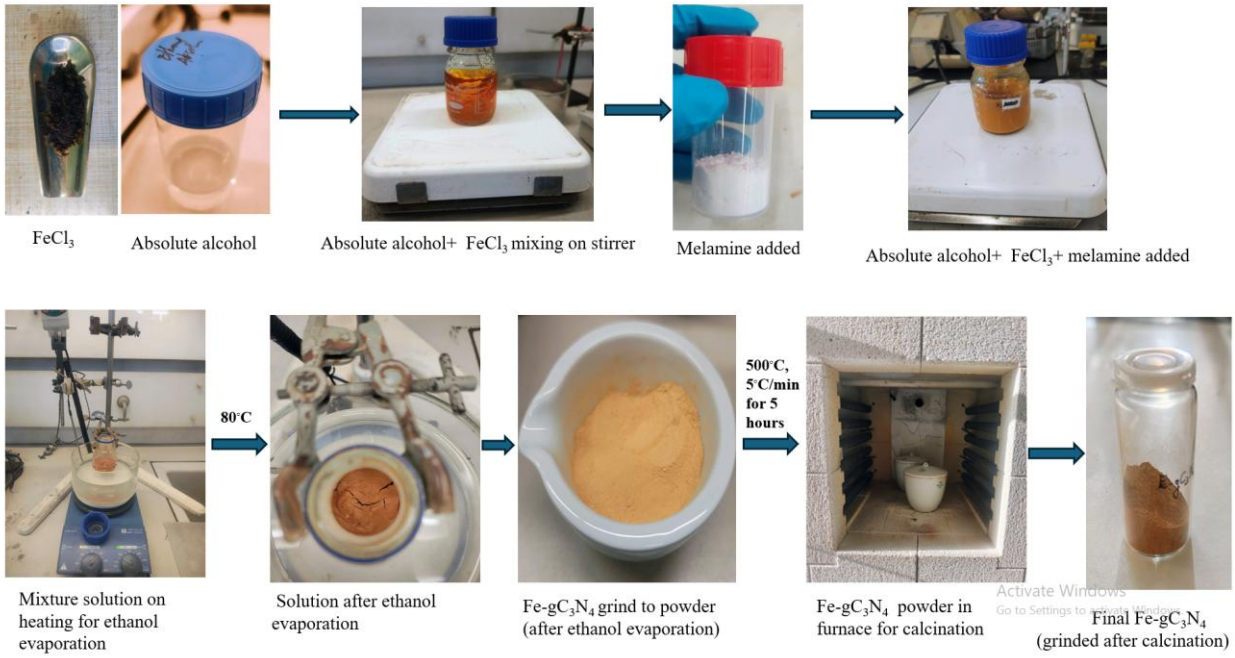

Figure 24: Synthesis of Fe/g-C_3N_4 sample

2.5 Synthesis of [Fe/g-C_3N_4]/AC binary composite

For the fabrication of [Fe/g-C_3N_4]/AC (AC = activated clay), 0.5 g of $FeCl_3$ was dissolved into 60 ml of absolute ethanol. Then 3 drops of HCl (10^{-2} M) were added and stirred properly. After that 10 g of melamine was added to it and the mixture was heated at 80 °C. So, when 50% ethanol was evaporated, then 5 g of AC was added to it. Then when ethanol was completely evaporated, the sample was dried in the oven overnight and crushed afterwards. The crushed powder was calcinated in the furnace at 500 °C for 5 h (temperature rate = 5 °C/min). After calcination, it was grinded again and finally [Fe/g-C_3N_4]/AC sample was obtained (Figure 25).

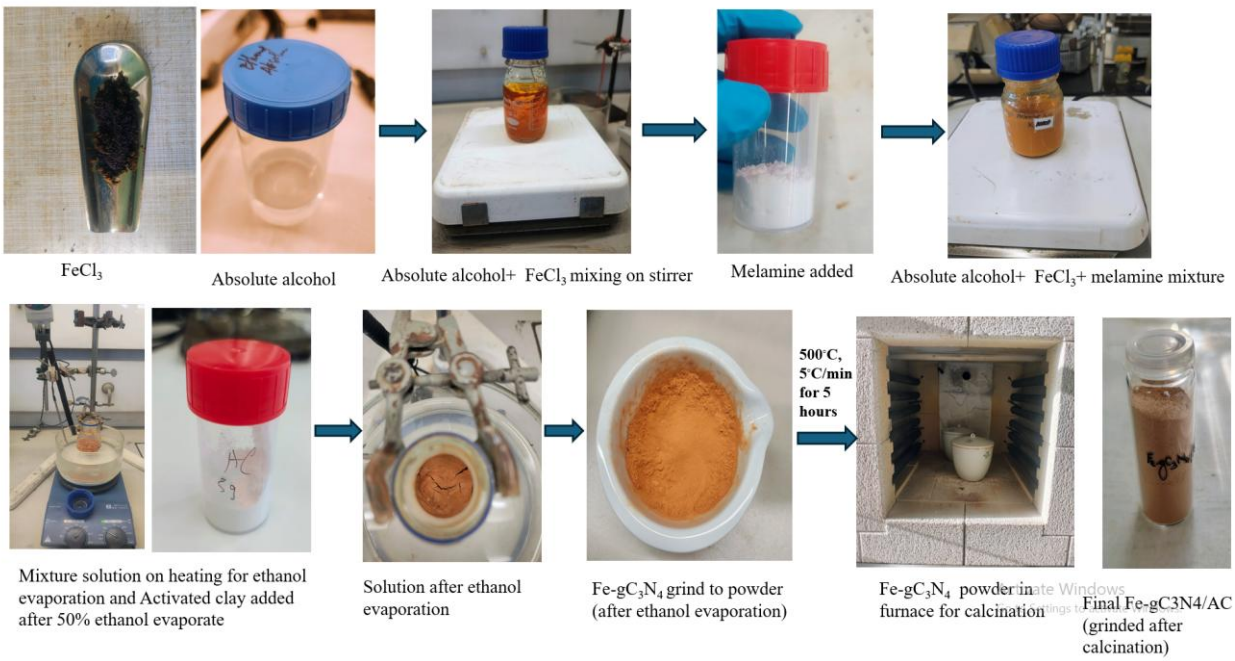

Figure 25 : Synthesis of [Fe/g-C_3N_4]/AC

2.6 Synthesis of ZnO

In this study, ZnO nanoparticles were prepared using the precipitation method-a common technique for large-scale production of reproducible nano powders. First 10 g of zinc acetate dihydrate (Zn $(CH_3CO_2)_2.2H_2O$) was dissolved in 100 ml of deionized water and stirred fully until complete dissolved. Then it was heated at 80 °C on the heating plate. During heating, 200 ml of NaOH (0.5 M) was added to it by burette dropwise and a white precipitate began to form. This mixture was then stirred for 2 h at 80 °C. After that, the solution was cooled down to room temperature. Then the precipitate was washed with water and recovered by centrifugation. So, it was dried for 24 h at 80 °C. Afterwards, it was grinded and white powder of ZnO nano particles was obtained. At last, the ZnO powder was calcined at 300 °C for 2 h (temperature range = 5 °C/min) (Figure 26).

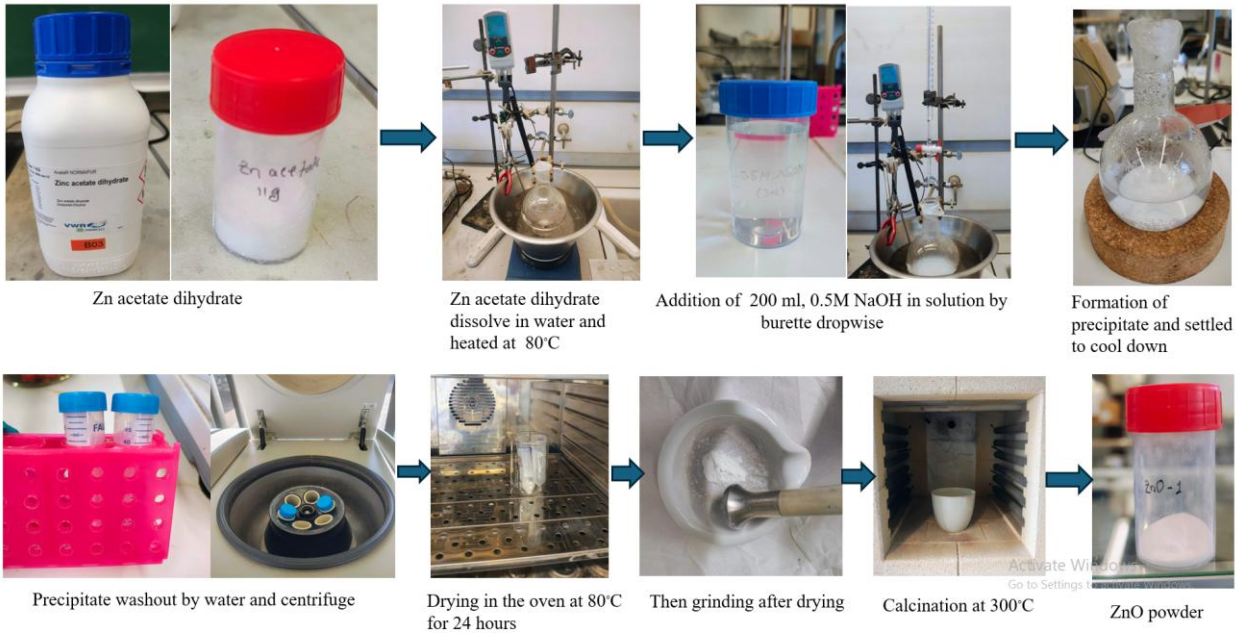

Figure 26 : Synthesis of ZnO sample

2.7 Synthesis of ZnO/AC composite

First 10 g of Zn $CH_3CO_2)_2.2H_2O$ was dissolved in 100 ml of deionized water and stirred fully until complete dissolution. Immediately 5 g of AC (activated clay) was added and stirred until fully dissolved. Here, the mass ratio [Zinc acetate]/[AC] was equal to 2. Then the sample was heated at 80 °C for 1 h. 200 ml NaOH (0.5 M) was added to it by burette dropwise and a precipitate began to form. This mixture was stirred for 2 h at 80 °C. After cooling down to room temperature, the precipitate was washed with water and recovered by centrifugation. The sample was then dried for 24 h at 80 °C. Afterwards, the powder was grinded. At last, ZnO/AC sample was calcined at 300 °C for 2 h (temperature rate = 5 °C/min) (Figure 27).

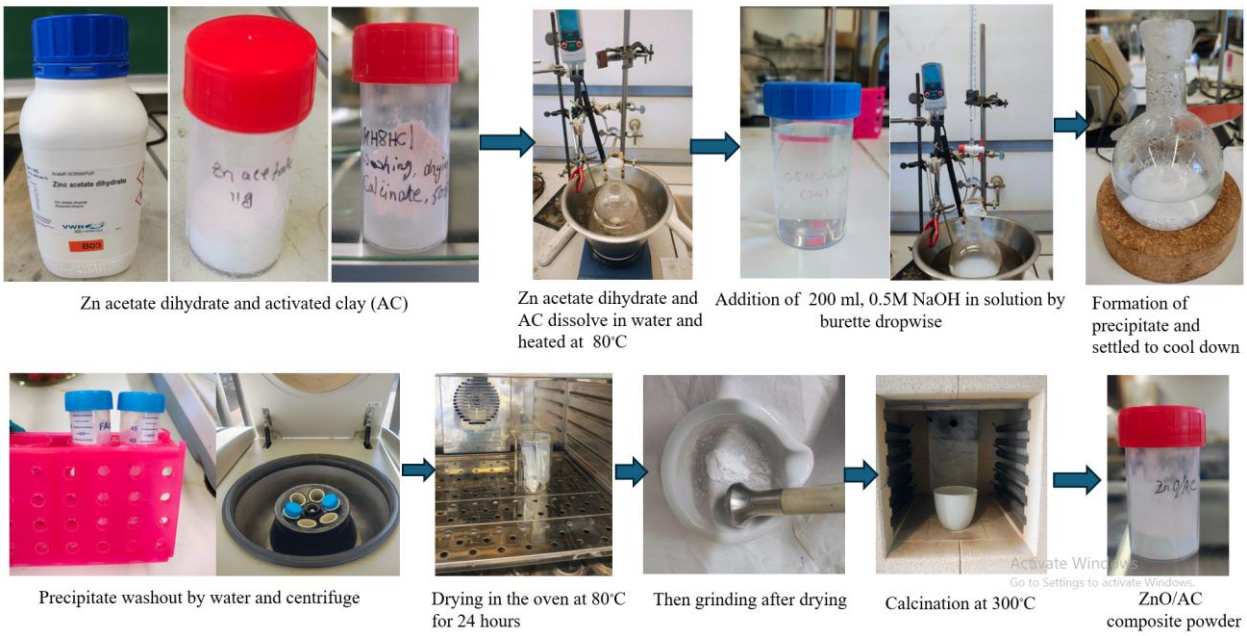

Figure 27: Synthesis of ZnO/AC sample

2.8 Synthesis of [Fe/g-C_3N_4]/ZnO composite

First 10 g of Zn $(CH_3CO_2)_2.2H_2O$ was dissolved in 100 ml of deionized water and stirred fully until complete dissolution. Immediately after, 5 g of Fe/g-C_3N_4 sample was added. The mass ratio [Zinc acetate]/ [Fe/g-C_3N_4] was equal to 2. Then the sample was heated at 80 °C for 1 h. After that, 200 mL of NaOH (0.5 M) was added to it by burette dropwise and a precipitate began to form. The mixture was stirred for 2 h at 80 °C. After cooling dried from temperature, the precipitate was washed with water and recovered by centrifugation. The sample was dried for 24 h at 80 °C. Afterwards, the [Fe/g-C_3N_4]/ZnO powder was calcined at 300 °C for 2 h (temperature rate = 5 °C/min) (Figure 28).

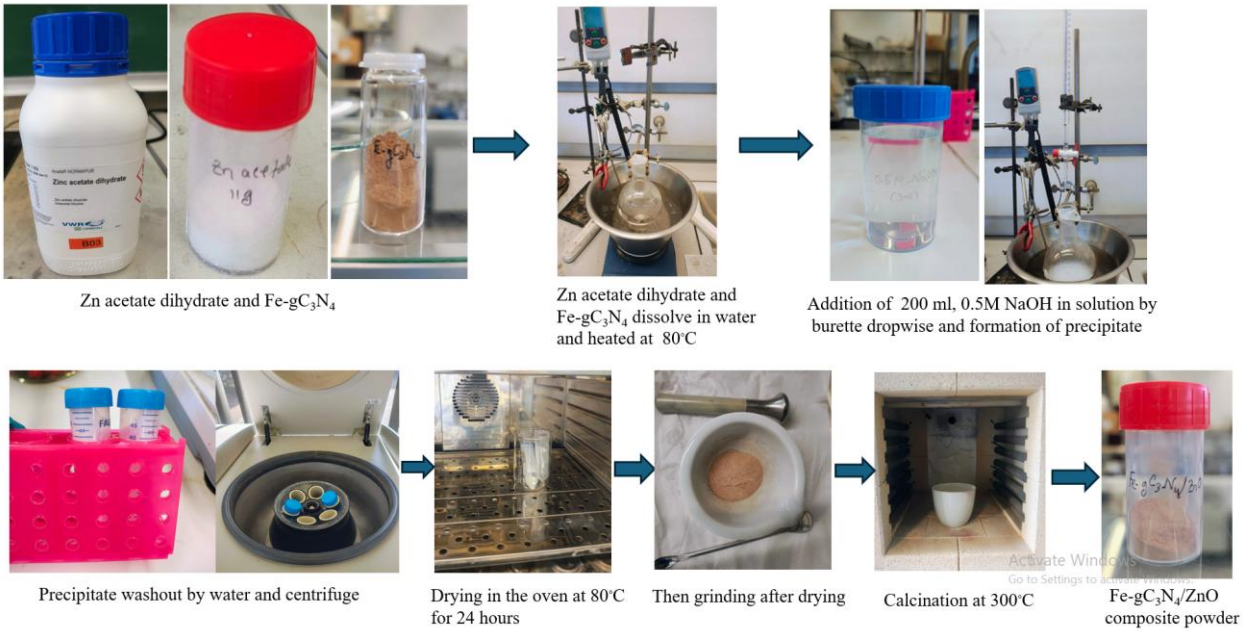

Figure 28 : Synthesis of [Fe/g-C_3N_4]/ZnO sample

2.9 Synthesis of [Fe/g-C_3N_4]/ZnO/AC ternary composite

First 10 g of Zn $(CH_3CO_2)_2.2H_2O$ was dissolved in 100 mL of deionized water and stirred fully until complete dissolution. Immediately after, 5 g of [Fe/g-C_3N_4]/AC powder was added. Here, the mass ratio [Zinc acetate]/[Fe/g-C_3N_4]/AC] was equal to 2. Then the mixture was heated at 80°C for 1 h. After that, 200 mL of NaOH (0.5 M) was added to it by burette dropwise and a precipitate began to form. This mixture was stirred for 2 h at 80 °C. After cooling down to room temperature, the precipitate was washed with water and recovered by centrifugation. The powder was then dried for 24 h at 80 °C and grinded. [Fe/g-C_3N_4]/ZnO/AC powder was calcined at 300 °C for 2 h (temperature rate = 5 °C/min) (Figure 29).

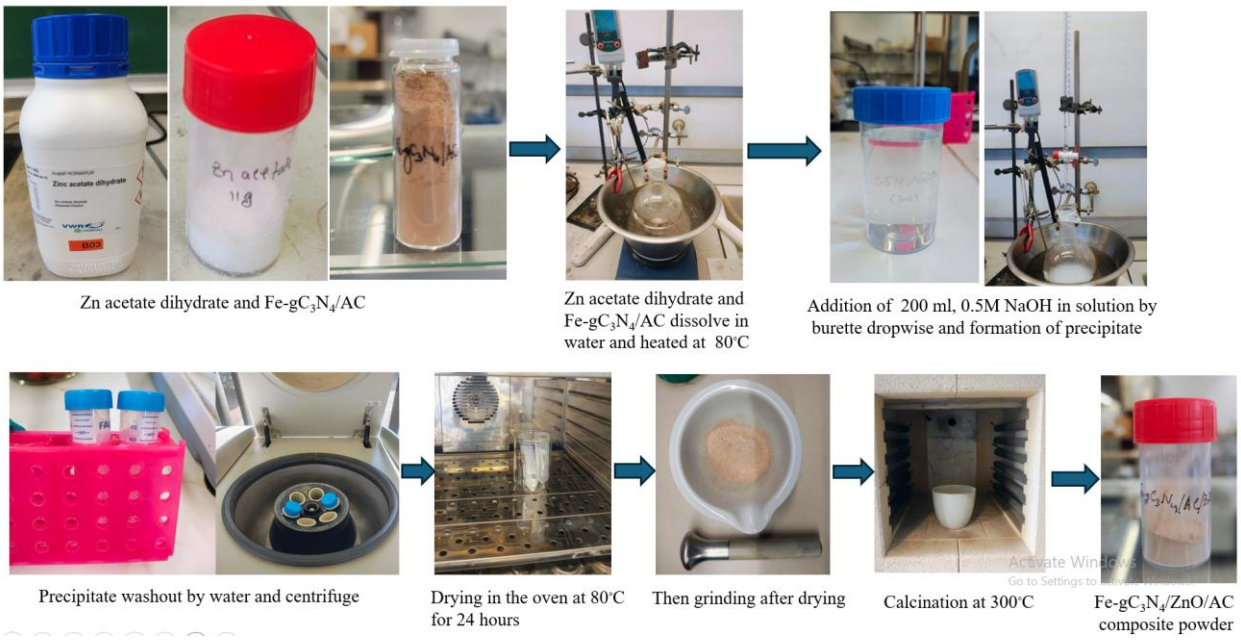

Figure 29 : Synthesis of [Fe/g-C_3N_4]/ZnO/AC

2.10 Characterization of samples

2.10.1 Scanning Electron Microscopy (SEM)

SEM is a powerful and versatile surface characterization technique widely used to investigate the morphology, topography, composition, and crystallographic features of materials with very high spatial resolution. In SEM, a focused beam of high-energy electrons scans the sample surface, generating signals such as secondary electrons (SEs), backscattered electrons (BSEs), and X-rays through interactions with the sample atoms. These emitted signals are collected by detectors to produce detailed images and compositional information about the material. SEM can achieve magnifications up to 300,000× with resolutions approaching 1 nm. The high resolution of SEM is mainly due to the very short wavelength of electrons, as explained by the de Broglie relation:

$$\lambda = \frac{\mathrm{h}}{mv} \text{ …….. (2.2)}$$

where λ is the electron wavelength (m), h is the Planck's constant (J.s), m is the electron mass (kg), and v is its velocity (ms^{-1}). In SEM analysis, samples are mounted on conductive stubs, usually with carbon tape, and non-conductive materials are often coated with conductive metals such as gold or platinum to minimize surface charging. The analysis is performed under vacuum to prevent electron scattering by air molecules. The primary electron beam, accelerating typically between 1-40 keV, is focused onto the sample surface where elastic and inelastic interactions occur within an interaction volume. Secondary electrons mainly provide information about surface morphology and topography, while backscattered electrons reveal compositional contrast.

Characteristic X-rays generated from electron transitions are used for elemental analysis through energy-dispersive X-ray spectroscopy (EDS) (Figure 30). The interaction volume and signal generation depend on factors such as accelerating voltage, atomic number, and beam incidence angle [61]. Overall, SEM is considered a non-destructive and highly effective technique for detailed surface and microstructural characterization of materials.

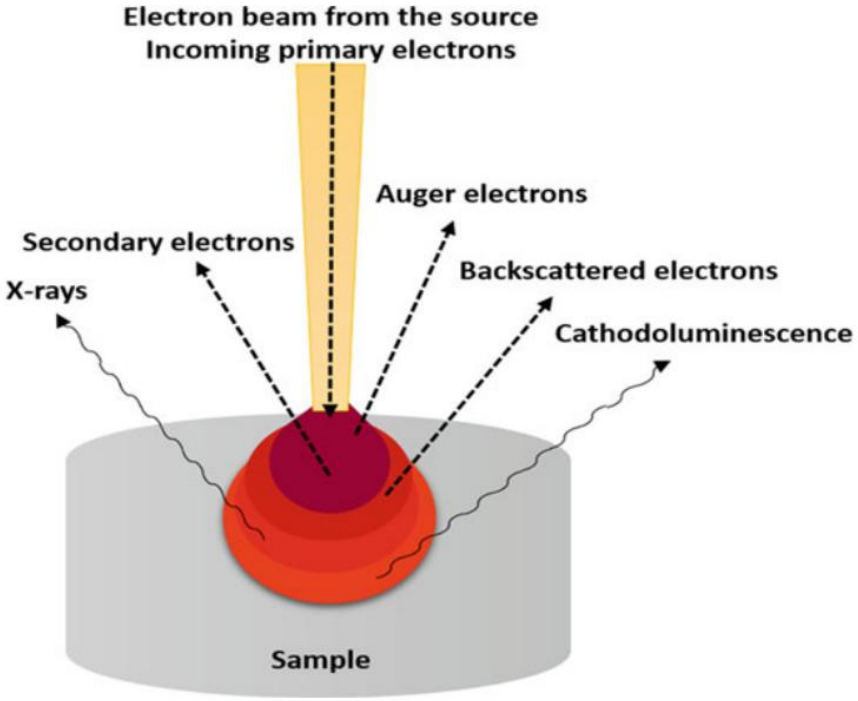

Figure 30: SEM electron beam interactions with sample [61]

In this work, a TESCAN Clara microscope was used under high-vacuum conditions with a 15 keV accelerating voltage. For sample preparation, 1-2 mg of a powder sample (with particle sizes < 2 μm) was placed into a 10 mL bottle. A small volume of acetone was added to create a relatively thick suspension. The mixture was ultrasonically dispersed for 10 min and then drops of the suspension were placed onto a prepared glass slide. The slide was subsequently dried at 60 °C to evaporate acetone. To ensure electrical conductivity of the sample, a thin gold layer was applied using a sputter coater. Finally, the sample was mounted onto a stub using a conductive carbon adhesive sheet.

2.10.2 X-ray Diffraction (XRD)

XRD provides detailed information about atomic arrangements, crystal structures, unit cell parameters and phase identification. This technique is applicable to a wide range of materials, including metals, minerals, ceramics, polymers, and semiconductors, and serves various industries such as mining, power generation, aerospace, and microelectronics [62].

The principal mechanism of XRD relies on the constructive interference of X-rays scattered by the electrons surrounding atoms in a crystalline material. When monochromatic X-rays impinge on a sample, they are scattered in multiple directions; however, only when the atomic arrangement is periodic and orderly does constructive interference occur, producing measurable diffraction peaks (Figure 31). This condition is quantitatively described by Bragg's Law:

$$n\lambda = 2d\sin\,\theta \ldots\ldots\ldots\ldots\ldots\ldots \text{(2.3)}$$

Where λ is the wavelength, d is the interplanar spacing of atomic planes, and θ is the diffraction angle. Peak positions reveal the size and shape of the unit cell, while peak intensities provide information about atomic positions within the cell. Using these principles, XRD can distinguish crystalline materials (which show multiple sharp peaks) from amorphous materials (which display only broad humps due to the lack of periodicity) [62].

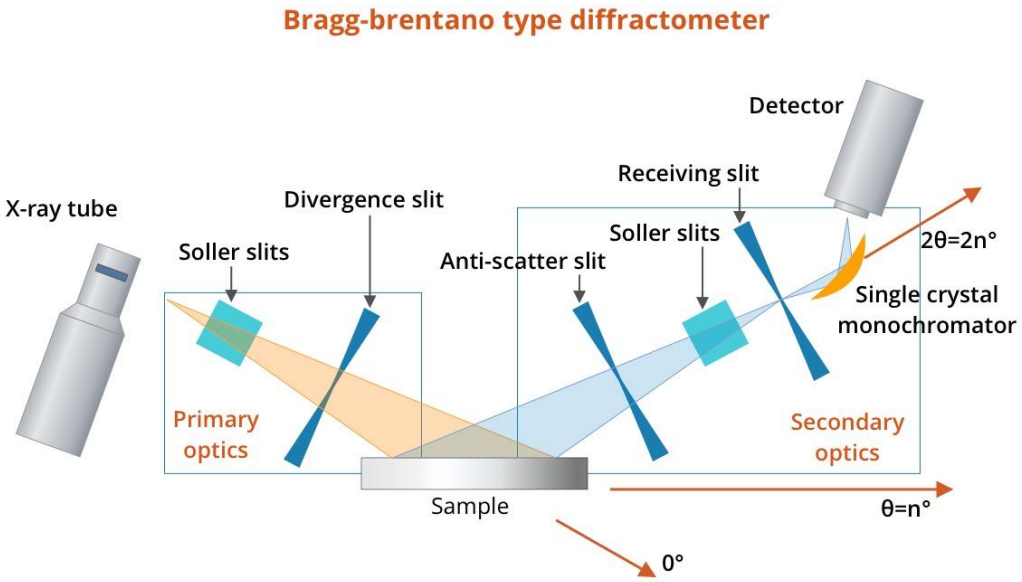

Figure 31: Typical mechanism of XRD technique [63]

In this study, XRD measurements were conducted on a Bruker D8 Twin-Twin powder diffractometer employing Cu-Kα radiation. Data were collected across a 2θ range from 2°-70°, using a step size of 0.02° and a scan speed of 2° per minute.

2.10.3 Nitrogen adsorption-desorption measurements

Nitrogen adsorption-desorption measurements at –196 °C are used for evaluating the specific surface area, porous volume and pore sizes in different materials. These measurements give curves called isotherms, which represent the adsorbed volume of nitrogen as a function of nitrogen relative pressure (p/p_0). The physicians Brunauer, Emmett and Teller defined the adsorption isotherm by the following equation [64]:

$$\frac{\left(\frac{p}{p_0}\right)}{v_a\left(1-\frac{p}{p_0}\right)} = \frac{1}{v_m c} + \left(\frac{c-1}{v_m c}\right)\left(\frac{p}{p_0}\right) \quad \text{..... (2.4)}$$

where $p/p_0$is the relative pressure, $p_0$is the atmospheric pressure, $v_a$is the volume adsorbed per unit mass of the adsorbent (cm^3/g), $v_m$is the volume of adsorbate required to cover the surface of the adsorbent with a monolayer of adsorbate molecules (cm^3/g), and $c$is a constant, known as the BET constant, which depends on the interactions between the adsorbate and the adsorbent. This equation can also be written in the following form:

$$y = \frac{\left(\frac{p}{p_0}\right)}{v_a\left(1-\left(\frac{p}{p_0}\right)\right)} \quad \text{..... (2.5)}$$

If $x = p/p_0$, a plot of $y = f(x)$can be constructed for $x$values ranging from 0.05 to 0.35, corresponding to the relative pressure range required for the formation of a monolayer of adsorbate on the adsorbent surface. If the BET model is valid, the resulting plot should yield a straight line of the form: y=αx+β. From the values of the slope (α) and intercept (β), the BET constant, c, and the monolayer adsorption capacity, v_m, corresponding to the minimum volume of adsorbate required to form a complete monolayer on the adsorbent surface, can be determined using the following two equations:

$$c = \frac{\alpha}{\beta} + 1 \quad \text{and} \quad v_m = \frac{1}{\alpha+\beta} \quad \text{..... (2.6)}$$

The value of $v_m$is directly proportional to the specific surface area of the adsorbent (sample), since $v_m$is, by definition, the amount of adsorbate required to form a complete monolayer covering the surface developed by the sample per unit mass of the sample. Therefore, the specific surface area of a solid is equal to the area occupied by a single adsorbate molecule multiplied by the number of adsorbate molecules contained in v_m, and can be expressed as follows:

$$S_{BET} = a_m \frac{v_m N_A}{V_m} \quad \ldots\ldots\ldots\ldots (2.7)$$

where $S_{BET}$is the specific surface area (m^2/g); $a_m$is the surface area occupied by a single adsorbate molecule in a monolayer, which for nitrogen as the adsorbate is $a_m = 16.2 \times 10^{-20}\ m^2$; $N_A$is Avogadro's number, $N_A = 6.022 \times 10^{23}\ mol^{-1}$; and $V_m$is the molar volume of the adsorbate, which for nitrogen is $V_m = 22.414 \times 10^{-3}\ m^3\ mol^{-1}$. By substituting these values into the above equation, that is, when nitrogen is used as the adsorbate, the following expression is obtained:

$$S_{BET} = 4.37\ v_m \ldots\ldots\ldots\ldots\ldots (2.8)$$

In this study, textural characteristics of the samples were assessed using nitrogen adsorption-desorption measurements conducted on a Micromeritics ASAP 2420 multi-sampler volumetric unit. From the nitrogen adsorption-desorption isotherms, the specific surface area (S_{BET}) was determined through BET method. The specific microporous volume (V_{DR}) was obtained using the Dubinin-Radushkevich theory, while the specific volume of adsorbed liquid was measured at the saturation pressure of nitrogen (V_p).

2.10.4 Zeta potential

Zeta potential (ζ) analysis is a characterization technique based on the movement of dispersed particles in a fluid under an electric field. It provides information about surface charge, which is fundamental for understanding solid-fluid and solid-solid interactions. This knowledge is crucial for optimizing the synthesis and performance of functional materials. The technique is widely applied in fields such as heterogeneous catalysis, nanomaterials, pharmaceuticals, food processing, and environmental science [65]. Zeta potential corresponds to the electrokinetic potential at the slipping plane between the immobile Stern layer and the mobile diffuse layer surrounding a charged particle in suspension. It is not measured directly but calculated from electrophoretic mobility (velocity per unit electric field). The most common method for zeta potential determination is electrophoretic light scattering (ELS). In many cases, ζ(V) is related to the electrophoretic mobility (U/E, $m^2 \cdot V^{-1} \cdot s^{-1}$) through Henry's equation under an applied electric field:

$$U/E = 2\ \epsilon\ \zeta\ F(ka) / 3\ \eta \ldots\ldots\ldots\ldots\ldots (2.9)$$

where ε is the dielectric permittivity of the solvent ($kg \cdot m \cdot V^{-2} \cdot s^{-2}$), η is the dynamic viscosity of the medium ($kg \cdot m^{-1} \cdot s^{-1}$), and $F(\kappa a)$is the dimensionless Henry's function, which depends on the particle size and the thickness of the electrical double layer. In aqueous media, the surface charge of particles arises from protonation or deprotonation of surface hydroxyl groups, which depends strongly on *pH*. At low *pH*, surfaces tend to be positively charged; at high *pH*, negatively charged. The "isoelectric point (IEP)" is the *pH* at which the net surface charge is zero, and the particle has no electrophoretic mobility.

The zeta potential magnitude indicates suspension stability: typically, values above ±30 mV suggest good stability due to electrostatic repulsion, while near-zero values lead to aggregation and flocculation [65].

In this work, zeta potential analysis of the samples was conducted using a Beckman Coulter Delsa Nano C particle analyzer. A quantity of 10 mg from each sample was dispersed into 10 mL of Milli-Q water using ultrasonication. Prior to measurement, the measuring cell was rinsed with Milli-Q water, after which the sample suspension was introduced.

2.10.5 X-ray photoelectron spectroscopy (XPS)

XPS is the most used technique in materials science, chemistry, and chemical engineering for assessing surface chemistry, bonding structure, and composition of surfaces and interfaces. XPS is based on the photoelectric effect, discovered by Hertz and explained by Einstein [66]. When a sample is irradiated with monochromatic X-rays (Figure 32) of known energy ($h\nu$), photons penetrate the surface and interact with core-level electrons of atoms in the sample. If the photon energy exceeds the electron's binding energy (E_B), the electron is ejected via the photoelectric effect. The kinetic energy (E_{kin}) of the emitted photoelectron is measured by a hemispherical electron energy analyzer. The binding energy is then calculated using [66]:

$$E_B = h\nu - E_{kin} \ldots\ldots\ldots\ldots\ldots \text{(2.10)}$$

However, for solid samples, the spectrometer's work function (ϕ_{SP}) also affects the measurement, so the practical equation is:

$$E_B^F = h\nu - E_{kin}^{SP} - \phi_{SP} \ldots\ldots\ldots\ldots\ldots \text{(2.11)}$$

where E_B^F is the binding energy referenced to the Fermi level. Only photoelectrons that escape from the top ~10 nm without inelastic scattering produce sharp and characteristic peaks. All other electrons that lose energy through collisions contribute to a step-like background on the high binding energy side of each peak [66]. The most critical aspect of the mechanism is the chemical shift. The binding energy of a core-level electron is not an intrinsic property of that electron alone; rather, it reflects the total energy difference between the ground state of the atom and the final state with a core hole after photoemission. When an atom is in a different chemical environment (e.g., bonded to more electronegative elements), the valence charge density around it changes. Reduced valence charge density (poorer screening) means the core hole experiences stronger Coulomb attraction, so the emitted photoelectron leaves with lower kinetic energy (appearing at higher binding energy). This is why, for example, the C 1s peak in CF_3 appears at a much higher binding energy than in CH_3 groups [66].

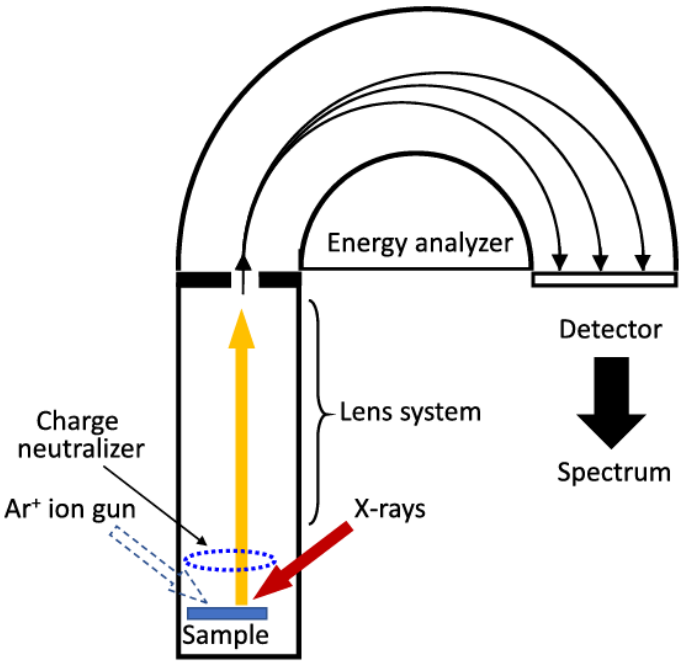

Figure 32: Photoelectron spectrometer with electron energy analyzer for XPS [66]

XPS is used for atomic elemental identification and quantification (down to 0.1-1 at%), chemical state determination via binding energy shifts, non-destructive thickness measurement of thin oxide layers (e.g., native oxides on metals), and surface analysis [66].

In this study, XPS analysis of the samples was performed using an SSI-X-probe 100/206 spectrometer (Surface Science Instruments), equipped with an 8-eV flood gun for surface charge neutralization. Samples placed on an adhesive support were loaded into a Macor® carousel fitted with a nickel grid to minimize charging effects. Measurements were carried out at room temperature under a chamber pressure of 10^{-6} Pa. Data processing was performed using Casa XPS software (Casa Software Ltd., Teignmouth, UK), applying a Gaussian/Lorentzian (85/15) peak decomposition and a Shirley-type background subtraction. All XPS spectra were calibrated by setting the C-(C,H) component of the C 1s peak to 284.8 eV.

2.10.6 Diffuse reflectance spectroscopy (DRS)

DRS is a technique used to measure the light reflected from powdered or rough solid materials. The principle of DRS is based on the interaction of incident light with a particulate sample (Figure 33). Unlike transmission spectroscopy, DRS measures the light that is scattered back from the sample's surface. The key quantity is reflectance (R), defined as the ratio of reflected radiant flux to incident radiant flux. In powdered samples, diffuse reflectance predominates over specular (mirror-like) reflection, and its magnitude depends mainly on the sample's chemical composition rather than surface state.

The technique uses an integrating sphere to collect the diffusely reflected light, and the spectrum is typically recorded as reflectance versus wavelength [67]. The most widely used theoretical framework for DRS is the Kubelka-Munk (K-M) theory. When a sample is infinitely thick (i.e., additional thickness leads to no change in reflectance), the Kubelka-Munk (K-M) function establishes a relationship between the reflectance (R_∞), the absorption coefficient (K), and the scattering coefficient (S) as follows [67]:

$$F(R_\infty) = \frac{(1-R_\infty)^2}{2R_\infty} = \frac{K}{S} \ldots\ldots\ldots\ldots (2.12)$$

This function, or the apparent absorbance $[\log(1/R_\infty)]$, serves as a proxy for the true absorption spectrum. The scattering coefficient S depends on particle size; fine particles (0.1-1 μm) are preferred to minimize artifacts. For mixtures, the K and S coefficients are additive functions of the component concentrations, allowing quantitative analysis.

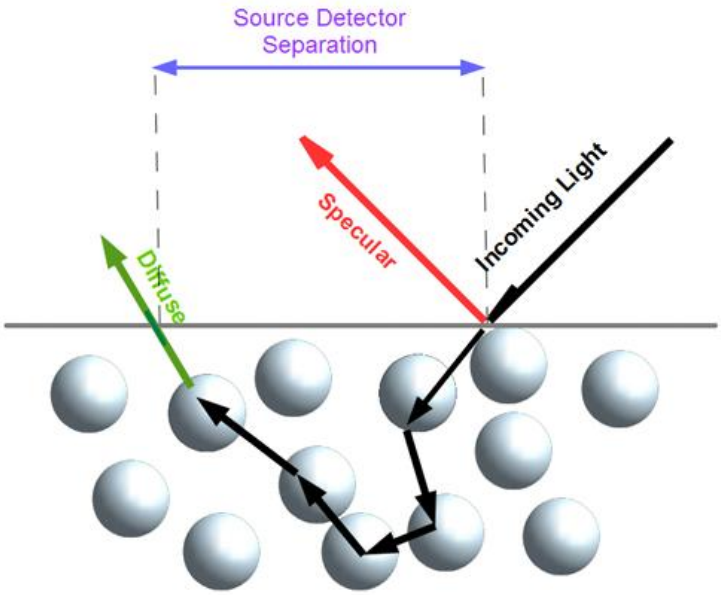

Figure 33: DRS mechanisms [67]

In this work, DRS measurements of the sample were conducted over a wavelength range of 200 to 800 nm using a PerkinElmer Lambda 1050 UV-Vis/NIR spectrophotometer, which was fitted with a Spectralon-coated integrating sphere and equipped with photomultiplier (PMT) and InGaAs detectors. The acquired spectra were converted using the Kubelka-Munk function to enable band gap determination and facilitate comparisons among samples. Barium sulfate ($BaSO_4$) served as the reference standard.

2.11 Photocatalytic experiments

In this master's thesis, the photocatalytic degradation of the azo dye RB5 was carried out using all synthesized samples within a photocatalytic reactor. The experimental setup and the individual components of the reactor are illustrated in Figure 34. For each test, 10 mg of a sample was added to 10 mL of RB5 dye contained in a test tube sealed with a cap. The test tubes were placed inside a cylindrical glass reactor that houses a centrally positioned halogen lamp (300 W, 220 V), which emits light across a continuous spectrum from 395 to 800 nm. A UV cut-off filter was applied, as verified using a Hamamatsu Mini-Spectrometer TM-UV/vis C10082MD. The reactor temperature was maintained at a constant 20 °C by means of a recirculating water-cooling system, and the lamp itself was cooled through a similar setup. To prevent interference from external light, the outer surface of the reactor was wrapped in aluminum foil [68].

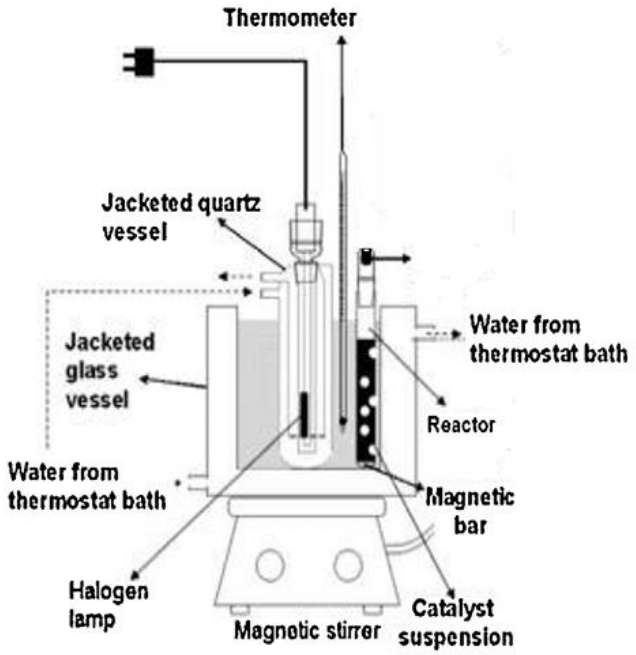

Figure 34: Photocatalytic reactor setup and arrangement [68]

Before starting the experiment, 20 ppm initial concentration of RB5 was made separately and total 8 samples were analyzed. 10 mg of each sample were taken in glass tube having 2 replica and 10 ml of dye was added. After that the tube was sealed with magnetic stirrer inside and placed in the reactor. The reaction time was 8 h total and after each 0,2,4,6 and 8 h, the residual concentration of the dye was recorded by collecting samples. It is to be mentioned that the solution was magnetically stirred in the absence of light for 30 min to establish adsorption-desorption equilibrium before starting the photocatalytic test. Figure 35 shows the procedure of the photocatalytic experiment.

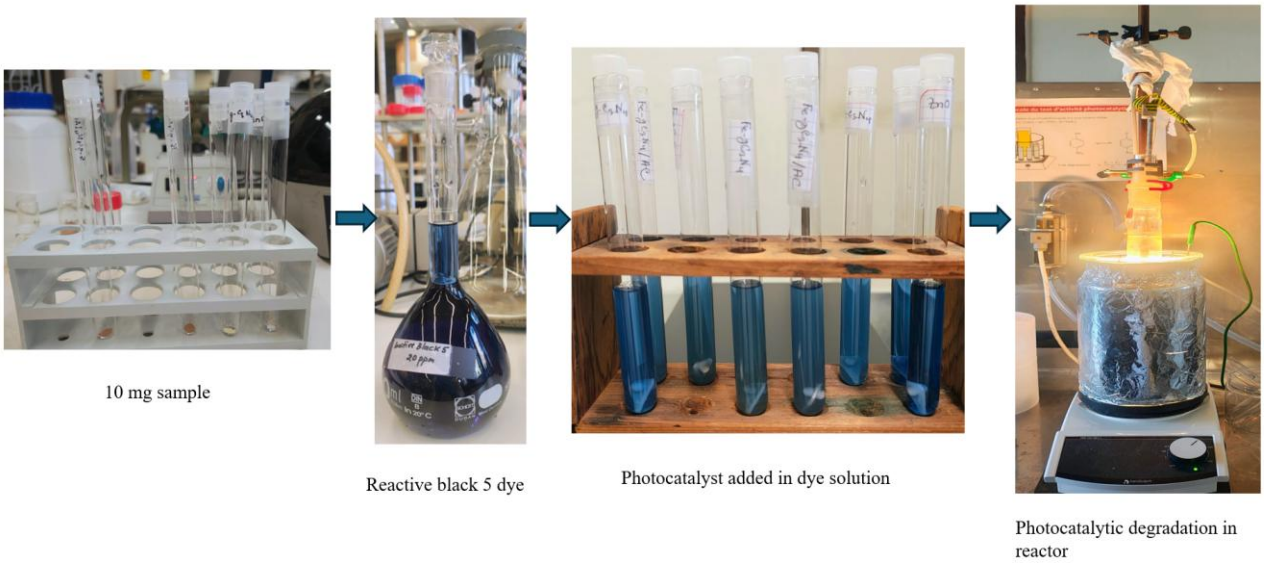

Figure 35: Photocatalytic degradation experiment of RB5

During the experiment, samples were collected at 0,2,4,6 and 8 h and the residual concentration of the dye was recorded by UV-Vis spectrophotometry (Genesis 10S, Thermo Scientific) at 600 nm. After that, the residual concentration was determined using the calibration curve of RB5 shown in Figure 47. The percentage degradation efficiency of the photocatalyst was calculated using the following formula:

$$\%\, Degradation = \frac{C_0 - C_t}{C_0} \times 100 \quad \ldots\ldots\ldots\ldots\ldots\ldots \quad (2.13)$$

where C_0 is the initial concentration of the dye (mg/L) and C_t is the concentration of the dye at time t after treatment (mg/L). For the sample [Fe/g-C_3N_4]/ZnO/AC, the experiment was also run for 2 h separately to record the residual concentration after 0.5, 1,1.5 and 2 h.

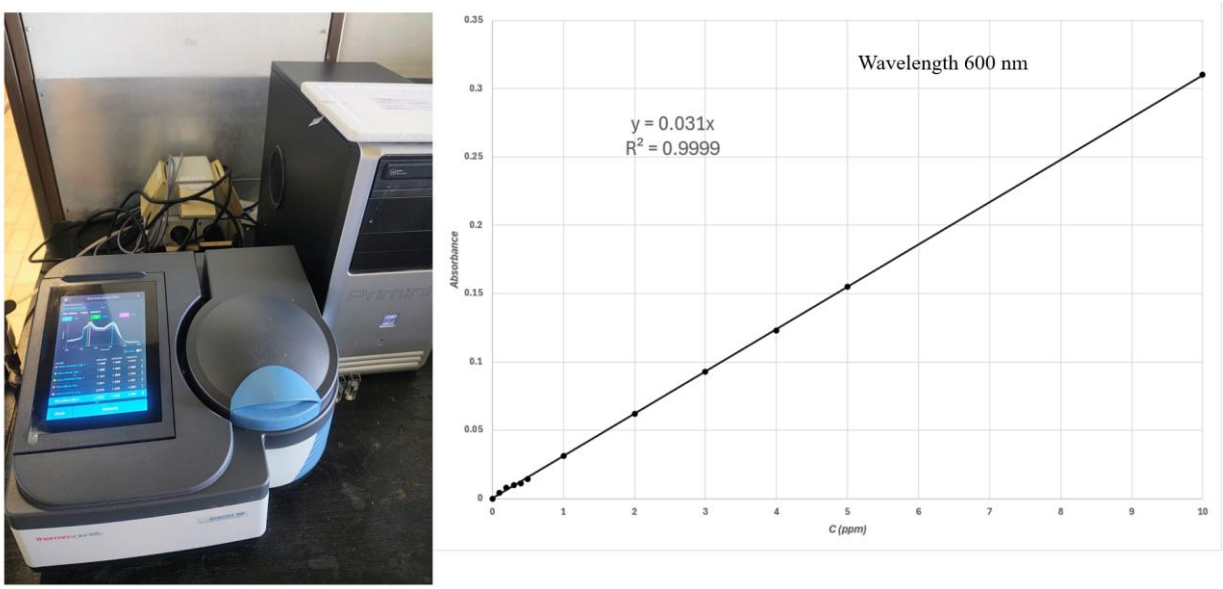

Figure 36: UV-Vis spectrophotometer and calibration curve of RB5 dye

Chapter 3: Results and discussion

3.1 SEM images analysis

Figure 37 (a) shows the SEM micrograph of raw halloysite clay which is characterized by its short-tube, spheroidal and tubular structure and coincides with the study of [41, 69]. But after undergoing the acid treatment (Figure 37(b)), the texture of the materials changed completely, and the activated clay has a rough and spongy texture. Such texture is a characteristic form of very porous solids in accordance with the high specific surface area (270 m^2/g) of these materials and found in other study [70-72].

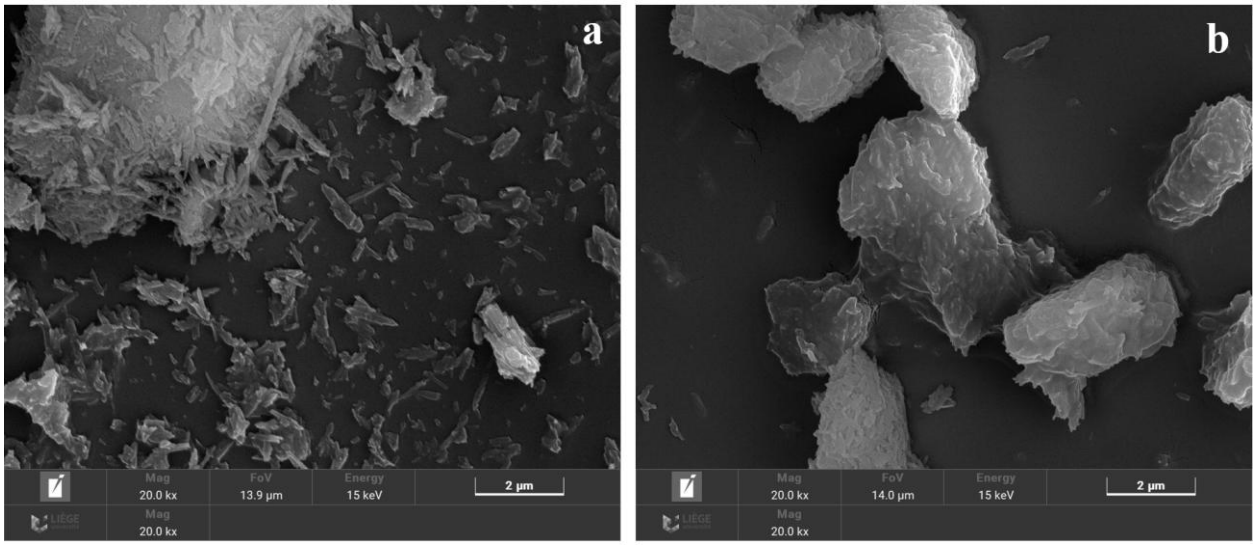

Figure 37 : SEM images of (a) Raw clay (RC) and (b) Activated clay (AC)

Figure 38 (a) represents the SEM image of g-C_3N_4, which exhibits a layered and stacked sheet-like structure with relatively smooth and compact surfaces [58]. The agglomerated lamellar morphology is the feature of bulk g-C_3N_4 formed during thermal polymerization. The sheet appears densely packed with limited porosity which may restrict the availability of active surfaces sites and hinder charge transfer during photocatalysis. In contrast, Figure 38(b) presents the SEM image of Fe/g-C_3N_4, which exhibits a more wrinkled, loosely packed, and exfoliated layered morphology than pure g-C_3N_4. After Fe doping, the stacked layers became less compact and exhibit increased surface roughness and structural distortion. This morphological change suggests that Fe species are successfully introduced into the g-C_3N_4 matrix, preventing excessive layer aggregation and creating more exposed active sites. These effects of metal doping also agree with the study of [58-60].

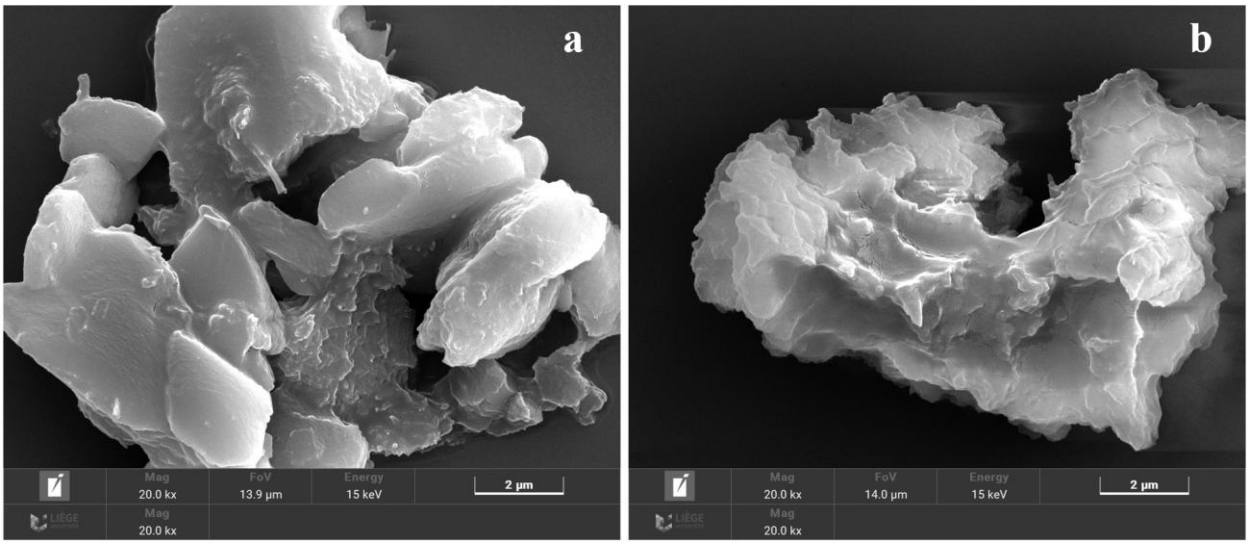

Figure 38: SEM micrographs of (a) g-C_3N_4 and (b) Fe/g-C_3N_4

Figure 39 represents the SEM images of ZnO nano particles, and it is seen that all the nano particles are agglomerated into irregular clustered structures with rough surfaces [49]. The image also shows the presence of rod-like and irregular granular ZnO particles distributed over the surface having densely packed, forming micro-sized aggregates due to the high energy of ZnO nanoparticles. Such agglomeration is commonly observed in ZnO nanoparticles synthesized through precipitation methods [49-51].

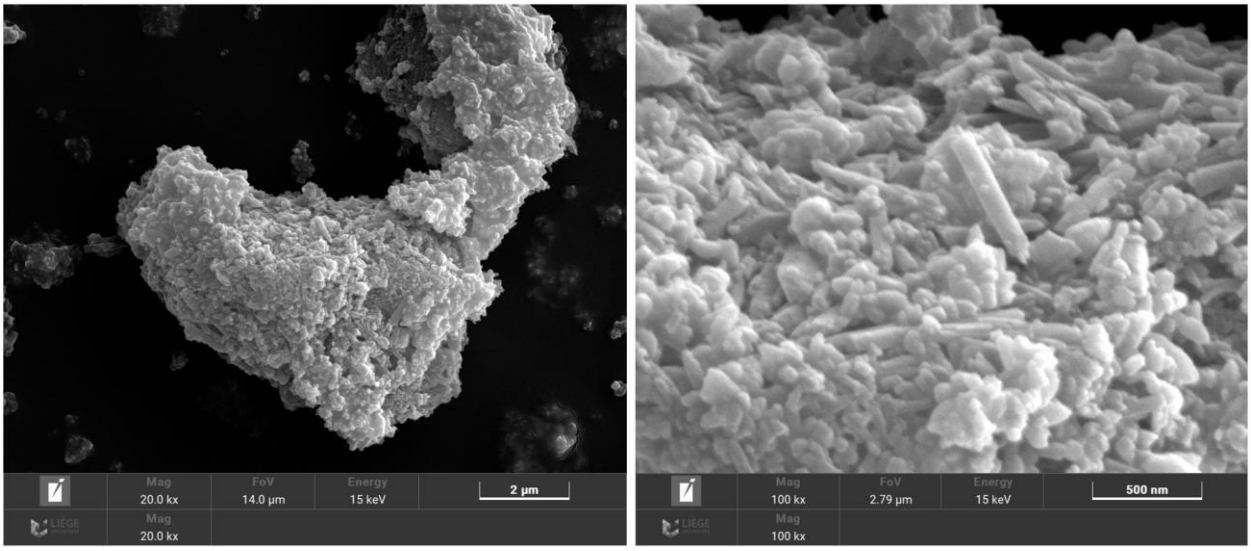

Figure 39: SEM images of ZnO nano particles

Figure 40 shows the SEM images of ZnO/AC composite, and the surface of this composite seem to be rough. It is seen from the images of activated clay that it is likely to have a porous or layered matrix after acid treatment and ZnO nano particles are distributed across the clay surface, appearing as rod-like, spherical or irregular shapes. The activated clay displays a roughened surface with high porosity which enhances the dispersion and anchoring of ZnO nano particles without significant aggregation. This is also noticed for other ZnO/clay composite in the study of [73-77].

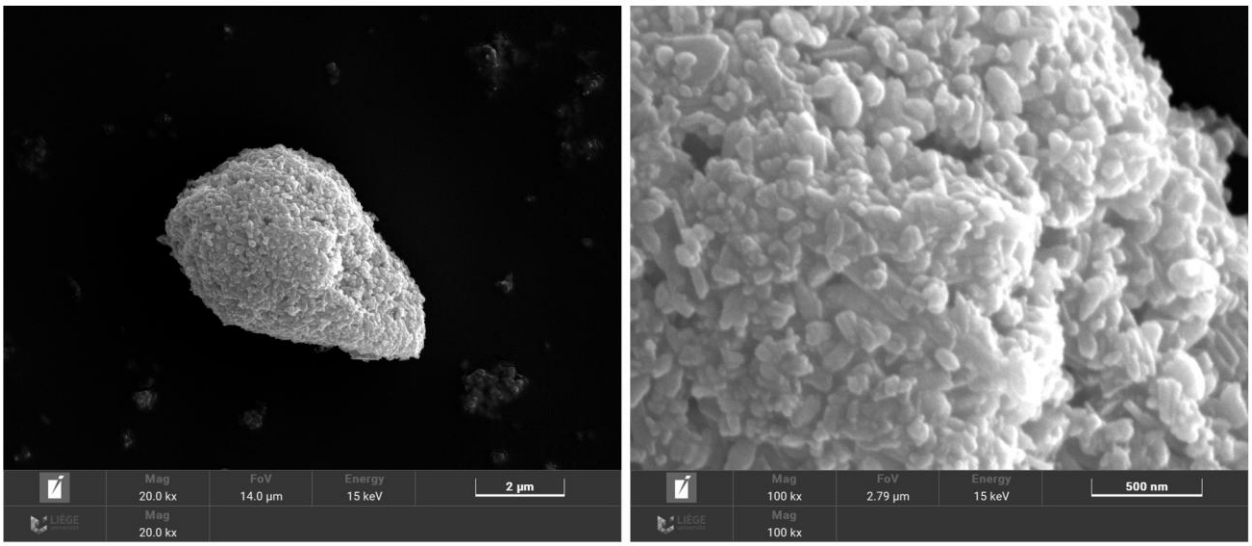

Figure 40: SEM images of ZnO/AC composite

Figure 41 highlights the SEM images of [Fe/g-C_3N_4]/ZnO composite which confirmed that pure and Fe doped g-C_3N_4 has sheet-like structure while ZnO showed smaller and irregular particles. The higher-magnification image reveals that the ZnO nanoparticles are uniformly dispersed across the surface of the Fe/g-C_3N_4 nanosheets, demonstrating effective deposition with minimal agglomeration. The image also denotes the intimate interfacial contact between two components showing wrinkled, thin Fe/g-C_3N_4 sheets decorated with nanoscale ZnO crystallites embedded on their surface and edges. Overall morphology suggests a well-structured composite with high specific surface area (15 m^2/g) compared to Fe/g-C_3N_4 and strong component interaction making it a good heterojunction formation. Other studies of [78-81] also reported similar observations with g-C_3N_4/ZnO composite.

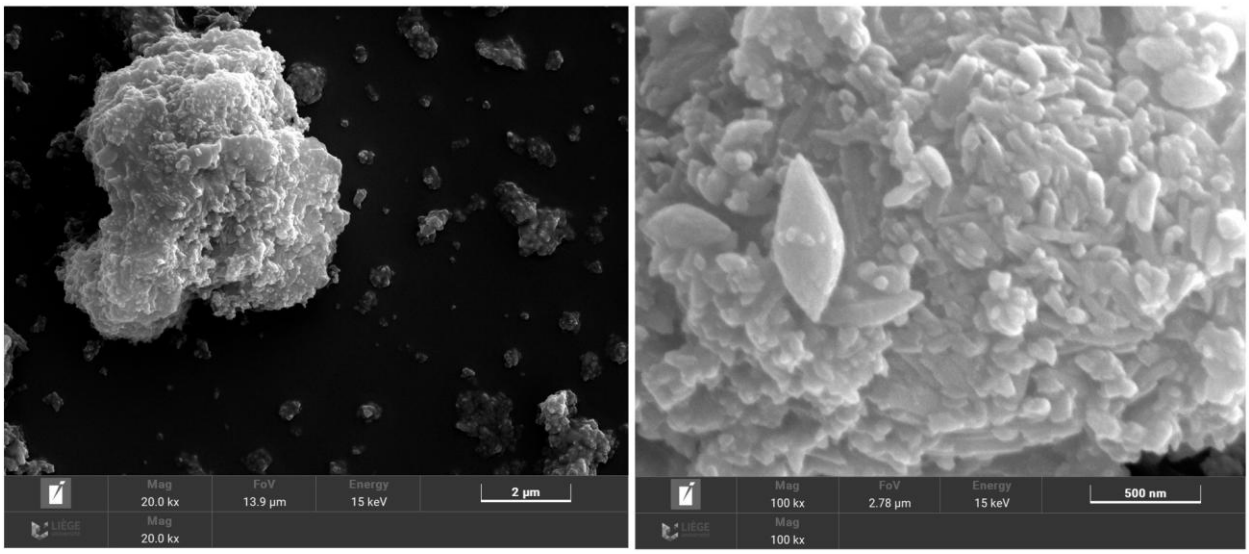

Figure 41 : SEM images of [Fe/g-C_3N_4]/ZnO composite

Figure 42 shows the SEM micrographs of ternary composite composites [Fe/g-C_3N_4]/ZnO/AC. It is observed that the activated clay forms tubular, irregular shaped and layered matrix with a rough surface resulting from acid treatment. The Fe/g-C_3N_4 also appears to be thin wrinkled sheet-like structures distributed over the clay surface while ZnO nanoparticles are well distributed across the whole matrix. At higher magnification image, it is even more evident that spherical and irregular ZnO nanoparticles are densely decorated on both the Fe/g-C_3N_4 sheets and on the clay, surface forming a nice heterostructure. No significant agglomeration of ZnO is observed which indicates uniform dispersion. The Fe/g-C_3N_4 serve as bridge to enhance electron transfer between the clay support and ZnO while the activated clay provides a stable, high-surface area platform. Different studies [76, 82-84] also observed this type of ZnO based ternary composite.

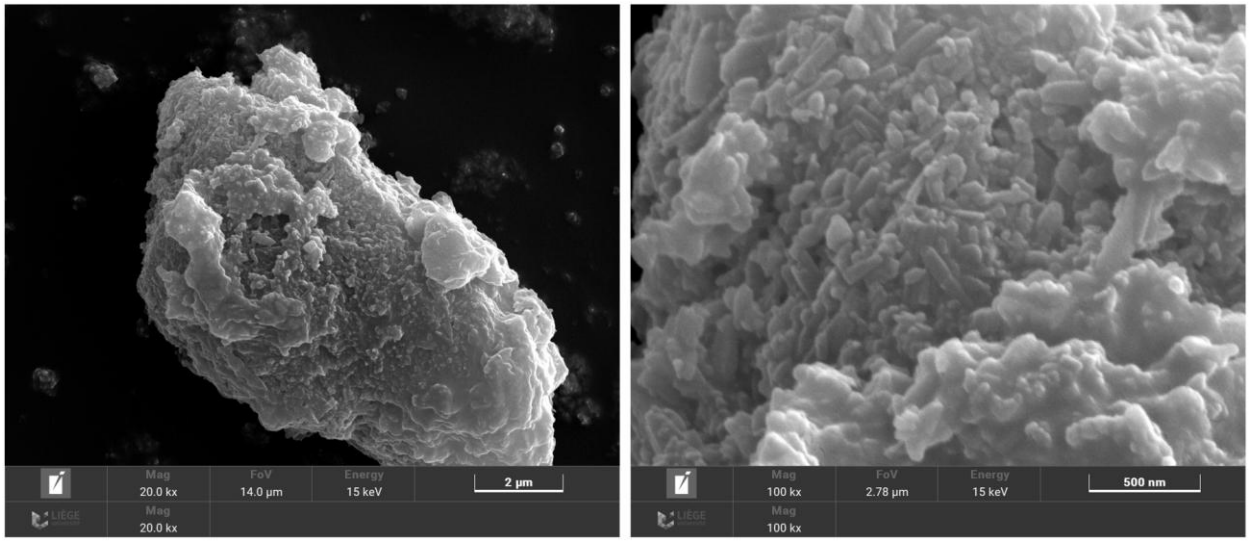

Figure 42 : SEM images of [Fe/g-C_3N_4]/ZnO/AC ternary composite

3.2 XRD analysis

From Figure 43, the dehydrated state and tubular structure of the raw clay (RC) halloysite (7 Å) are confirmed by the diffraction angles seen at 2θ = 12.09˚, 20.24˚ and 24.85˚. A prominent peak at 62.78˚ confirms the tubular morphology characteristics of halloysite nanotubes [41, 85]. The absence of peaks at 2θ = 8.8˚ in the XRD patterns provides additional evidence of the dehydrated state [86, 87]. The observed characteristics reflection 2θ values corresponding planes at 12˚ (001), 20˚ (100), 25˚ (002), 35˚ (110), 55˚ (210) and 63˚ (300) are consistent with earlier report of halloysite-7 Å (JCPDS card no. 29-1487) [87, 88]. After calcinating at 800 ˚C, the XRD pattern of meta-halloysite (MH 800) showed a broad diffraction peak observed in the range of 25-30˚ (2θ). The pattern also displays some noise and most of the characteristic peaks of halloysite nanotube have disappeared. This broad diffraction peak, identified as minor quartz, is probably due to the progressive amorphization of the halloysite nanotube structure [88-90]. This behavior is often attributed to dihydroxylation, a process where hydroxyl groups (OH) are released from material's structure at elevated temperature.

At higher temperatures, these hydroxyl groups start to dehydroxylate, leading to the loss of these characteristic peaks in the spectrum. These hydroxyl groups are often associated with the crystal lattice of mineral, and the dihydroxylation process somewhat alters the original crystalline structure producing meta-halloysite [90]. These findings affirm that halloysite nanotube is amorphous at temperature of 800 ˚C [90-93]. In addition to the signals of halloysite, several diffraction peaks corresponding to monoclinic halloysite (H) and cubic silicon oxide (denoted as Q) were also identified.

Again, for the activated clay (AC) with acid treatment, there was no noticeably different peak compared to the characteristic peaks of calcined halloysite clay. However, same broad diffraction peak was observed in the range of 25-30˚ (2θ) just like calcined halloysite with a little increase in intensity after HCl treatment [90-92, 94]. This obtained result is most likely due to structures' progressive amorphization. The current XRD results strongly support the fact that the crystal structure is maintained after acid treatment [91-94].

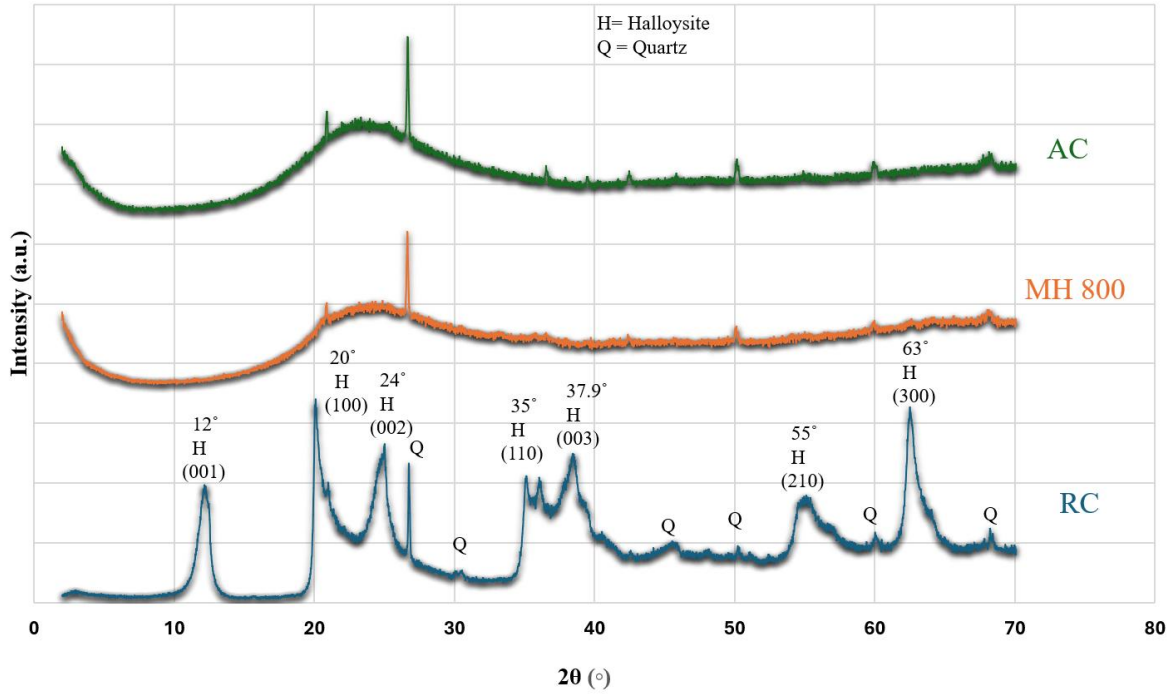

Figure 43: XRD spectra of RC, MH800 and AC

For g-C_3N_4 and Fe/g-C_3N_4 samples, two typical peaks were observed in the XRD patterns in Figure 44. The high intensity peak at 27.4˚ is ascribed to interplanar stacking of aromatic system, which is indexed to the (002) peak and corresponds to an interlayer distance of 0.326 nm [95, 96]. The peak around 13.2˚ is indexed as the (100) peak and can be associated with an in-plane structural packing motif [95, 96]. But with Fe doping, the diffraction peak intensity of the (002) facet gradually weakened. Since the delocalized π-bond of g-C_3N_4 possesses high electron density, which can provide electrons to d orbitals of Fe(III) ions, there is a strong mutual attraction between Fe(III) ions and g-C_3N_4. As a result, the crystal plane spacing (002) becomes smaller with Fe(III) ions content. This result implies that Fe(III) ions have been inserted into the interlayer of g-C_3N_4 [97]. Furthermore, several weak diffraction peaks appear in the range of 30°-70° for the Fe/g-C_3N_4 sample and these peaks can be indexed to the crystalline planes of FeOOH, indicating the formation of iron oxyhydroxide nanoparticles on the surface of g-C_3N_4. The low intensity of these peaks suggests that FeOOH is present in small quantities and is highly dispersed with in the g-C_3N_4 matrix [58].

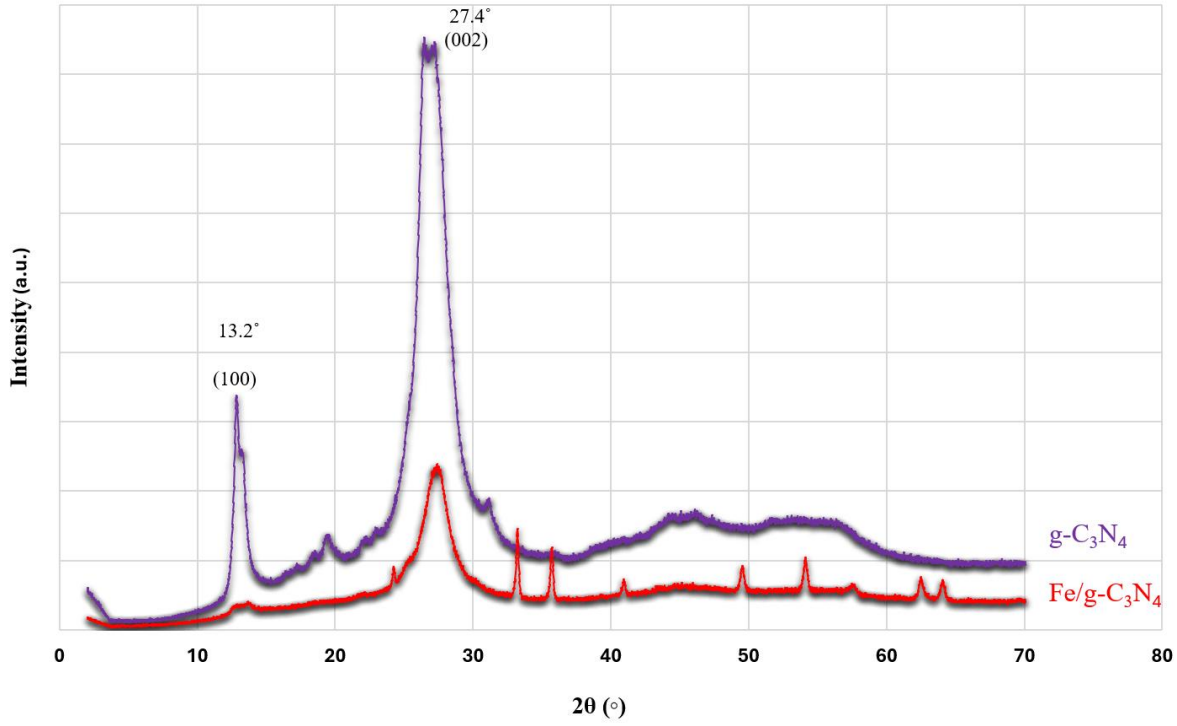

Figure 44: XRD spectra of g-C_3N_4 and Fe/g-C_3N_4 samples

In Figure 45, the XRD patterns of AC and Fe/g-C_3N_4 samples show their characteristics diffraction peaks as described above. But for the [Fe/g-C_3N_4]/AC composite, the characteristics g-C_3N_4 peaks at 13° and 27.5° are weaker compared to pure Fe/g-C_3N_4 sample. Furthermore, between 30° and 70° for 2θ, the characteristic FeOOH peaks remain visible, while the broad clay peak is also present confirming the presence of an amorphous clay matrix. All these observations should indicate that Fe/g-C_3N_4 particles are highly dispersed on the activated clay support without destroying its original structure. The amorphous clay can shield or dilute the crystalline signal of g-C_3N_4 compound. This decreased intensity is not a sign of degradation, but rather of good dispersion and successful integration of Fe/g-C_3N_4 onto the AC support [98, 99].

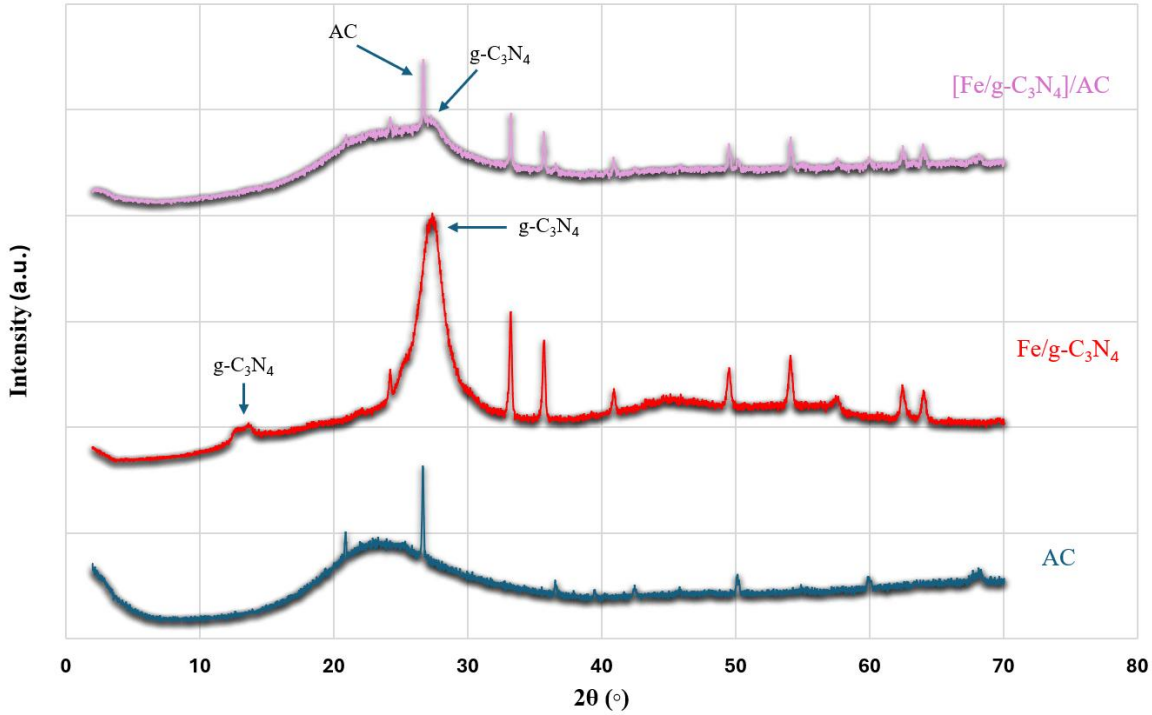

Figure 45: XRD spectra of AC, Fe/g-C_3N_4 and [Fe/g-C_3N_4]/AC samples

In Figure 46 for ZnO/AC composite, the characteristics ZnO peaks remain visible, but their intensity slightly decreases compared to ZnO sample, which is due to the dispersion of ZnO nanoparticles on the activated clay support matrix and the dilution effect introduced by the amorphous clay support. The sample also represents a broad hump between 20°-30° which is the characteristic peak for AC shown in Figure 57. A similar decrease of ZnO peaks intensity has been reported in ZnO/clay composite due to the high dispersion of ZnO nanoparticles into a clay matrix [84]. In the [Fe/g-C_3N_4]/ZnO and [Fe/g-C_3N_4]/ZnO/AC composites, the main diffraction peaks of ZnO-wurtzite are still present, indicating that the crystal structure of ZnO is preserved after doping with Fe/g-C_3N_4 and activated clay. Between 20° and30° for 2θ, a broad hump is due to the presence of amorphous structure of activated clay and to the presence of g-C_3N_4. These peaks are much weaker because activated clay and g-C_3N_4 present a lower crystallinity compared to the crystallinity degree of ZnO. This also confirms that ZnO nanoparticles are more visible (or present at the surface) compared to the other compounds as observed in Figure 42 (SEM picture) [76, 84].

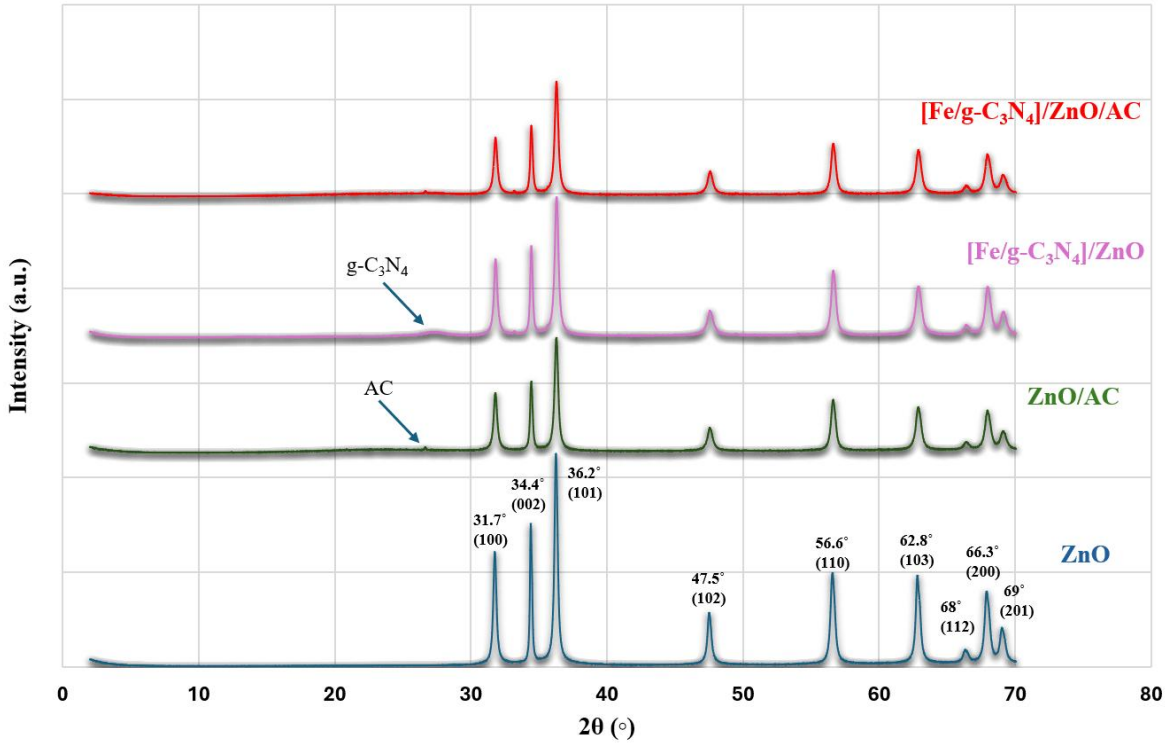

Figure 46: XRD spectra of ZnO, ZnO/AC, [Fe/g-C_3N_4]/ZnO and [Fe/g-C_3N_4]/ZnO/AC samples

3.3 Textural properties

The textural properties of all the synthesized materials were presented in Table 2. Among all the samples, activated clay (AC) shows the highest specific surface area, S_{BET}, equal to 270 m^2/g and a total pore volume, V_t, equal to 0.48 cm^3/g which indicates a highly porous structure compared to the S_{BET} and V_t values of the raw halloysite clay non activated (55 m^2/g and 0.19 cm^3/g respectively). On the other hand, the samples ZnO, g-C_3N_4 and Fe/g-C_3N_4 are non-porous materials (S_{BET} < 20 m^2/g). For the other binary and ternary samples, which contain 5 mg of AC, the S_{BET} and V_t values evolve between the values for each pure material contained in the composite.

Table 2: Textural properties of samples

Sample	S_{BET} (m^2/g)	S_{meso} (m^2/g)	S_{micro} (m^2/g)	V_t (cm^3/g)
RC (raw clay)	55	50	< 5	0.19
MH800	50	50	< 5	0.22
AC (activated clay)	270	145	125	0.48
g-C_3N_4	< 5	< 5	< 5	0.02
Fe/g-C_3N_4	< 5	< 5	< 5	0.02
[Fe/g-C_3N_4]/AC	80	60	20	0.21
ZnO	15	15	< 5	0.08
ZnO/AC	100	60	40	0.22
[Fe/g-C_3N_4]/ZnO	15	10	< 5	0.08
[Fe/g-C_3N_4]/ZnO/AC	40	35	5	0.14

S_{BET}: specific surface area obtained by BET method; S_{meso}: specific surface area determined by Broekhoff-de-Boer theory; S_{micro}: specific surface area determined by Dubinin theory; V_t: specific liquid volume adsorbed at saturation pressure of nitrogen.

Figure 47 shows the adsorption-desorption isotherms for raw clay (RC), thermal treated clay (MH800), and activated clay (AC). The isotherms of RC and MH800 samples are characteristic of the Type IV isotherms: these isotherms present hysteresis close to $p/p_0 = 1$, characteristic of the presence of high mesopores [64]. The isotherm of AC sample is a mixture between the Type 1 and Type IV isotherms: at very low pressure, the adsorbed volume increases very quickly, characteristic of the presence of micropores, and at higher p/p_0 values, a hysteresis appears, characteristic of the presence of mesopores. All these observations are in correlation with the S_{BET}, S_{meso} and S_{micro} values for these 3 samples (Table 2). So, the acidic activation treatment improves the porosity of the clay [76].

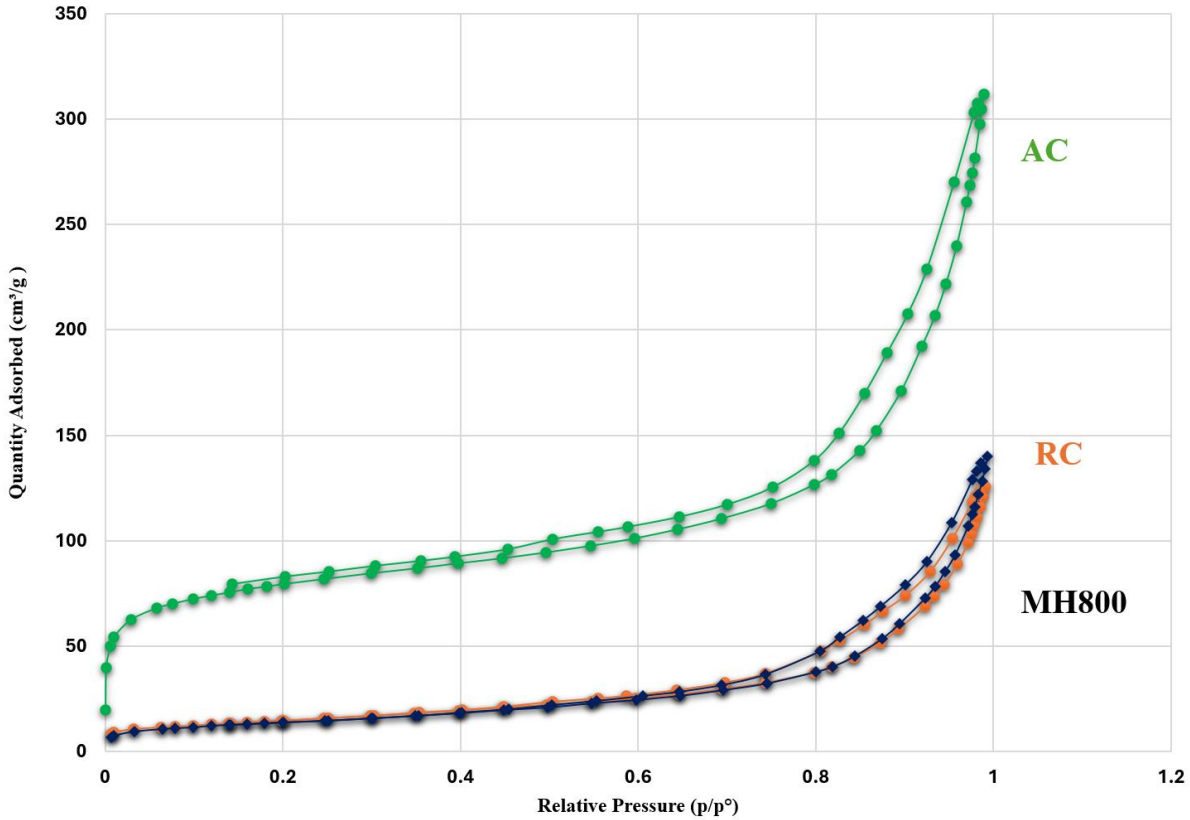

Figure 47: Nitrogen adsorption-desorption isotherms of RC, MH800 and AC samples

Figure 48 shows the adsorption-desorption isotherms of g-C_3N_4, Fe/g-C_3N_4 and [Fe/g-C_3N_4]/AC samples. The isotherms of g-C_3N_4 and Fe/g-C_3N_4 samples are characteristic of non-porous materials [64]. The isotherm of [Fe/g-C_3N_4]/AC sample is characteristic of the Type IV isotherm: at high p/p_0 values, a hysteresis appears, characteristic of the presence of mesopores. All these observations are in correlation with the S_{BET}, S_{meso} and S_{micro} values for these 3 samples (Table 2).

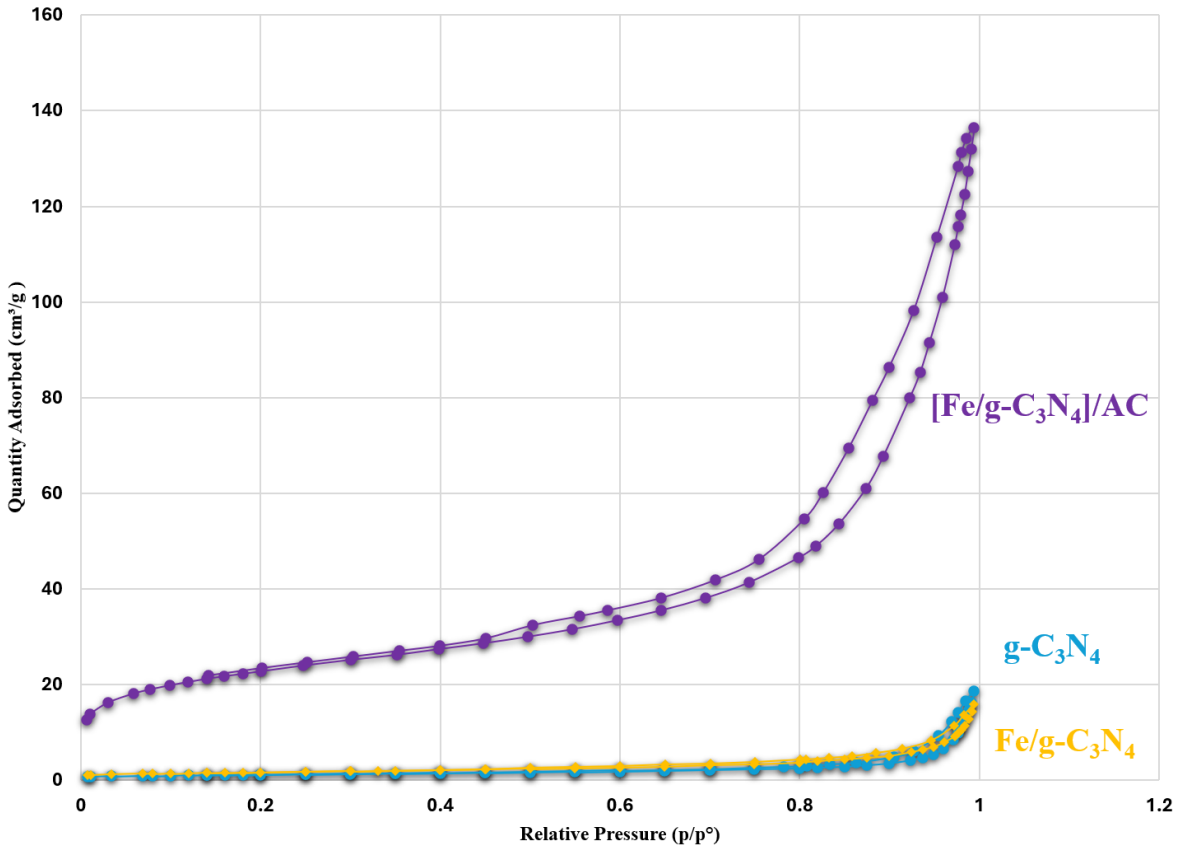

Figure 48: Nitrogen adsorption-desorption isotherms of g-C_3N_4, Fe/g-C_3N_4 and [Fe/g-C_3N_4]/AC samples

Figure 49 shows the adsorption-desorption isotherms of ZnO, ZnO/AC, [Fe/g-C_3N_4]/ZnO and [Fe/g-C_3N_4]/ZnO/AC samples. The isotherms of ZnO and [Fe/g-C_3N_4]/ZnO samples are characteristic of non-porous materials [64]. The isotherms of ZnO/AC and [Fe/g-C_3N_4]/ZnO /AC samples are characteristic of the Type IV isotherm: at high p/p_0 values, a hysteresis appears, characteristic of the presence of mesopores [64]. All these observations are in correlation with the S_{BET}, S_{meso} and S_{micro} values for these 4 samples (Table 2).

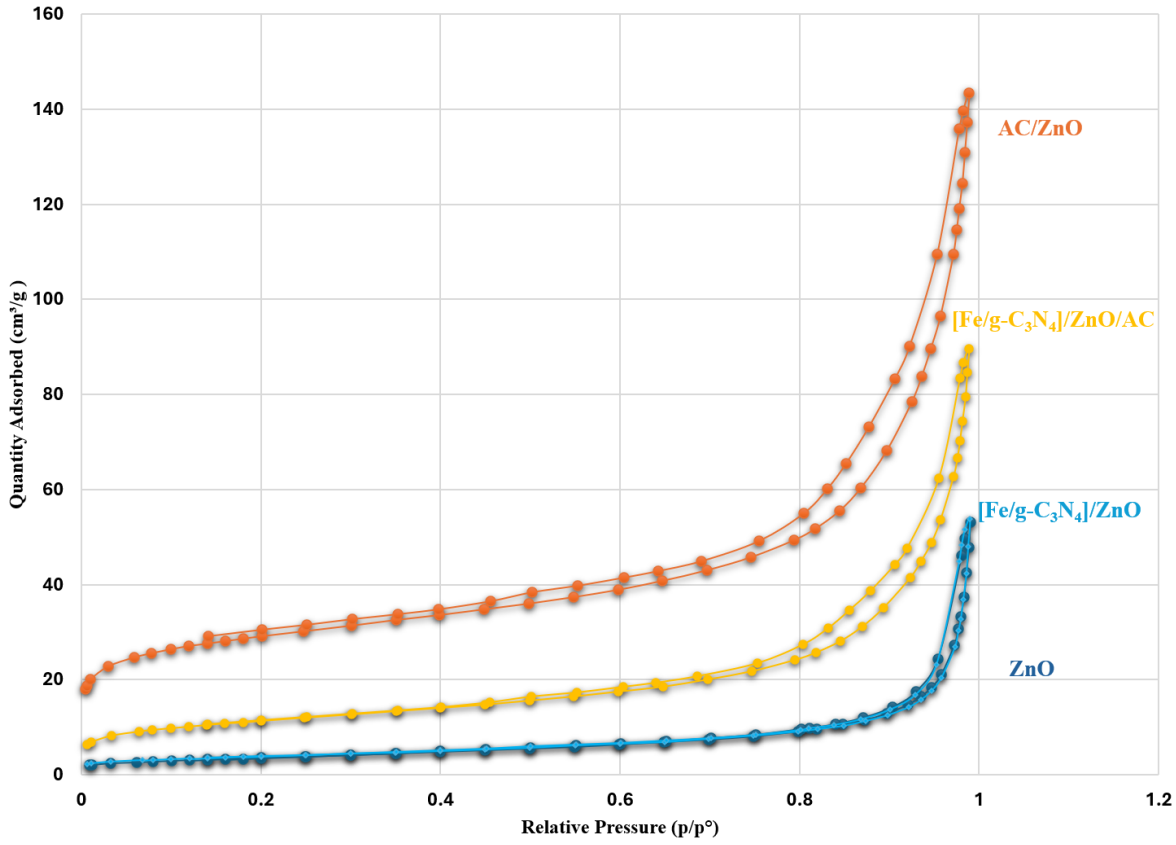

Figure 49: Nitrogen adsorption-desorption isotherms of ZnO, ZnO/AC, [Fe/g-C_3N_4]/ZnO and [Fe/g-C_3N_4]/ZnO/AC samples

3.4 Zeta potential analysis

The zeta potential analysis of the ten samples reveals a wide range of surface charges measured at *pH* values between 5.40 and 8.04, providing big differences in their electrostatic properties and interfacial interactions (Table 3). The zeta potential of RC is equal to −21.72 mV: the negative charge originates from the silanol groups (Si–O^-) on the outer surface of the halloysite nanotubes [100]. For MH 800 sample, the zeta potential slightly decreased to −22.59 mV, suggesting the formation of additional negatively charged surface sites caused by dehydroxylation and structural modification of the clay during calcination [101]. Activated clay (AC) showed a zeta potential equal to −20.62 mV, confirming that acid activation does not significantly change the negative nature of the clay surface, although slight charge reduction may occur due to leaching of structural cations and modification of surface hydroxyl groups [76].

Table 3: Zeta potential of the samples

Sample name	Zeta potential (mV)
Raw clay (RC)	−21.72
MH 800	−22.59
Activated clay (AC)	−20.62
g-C_3N_4	−30.16
Fe/g-C_3N_4	−21.13
[Fe/g-C_3N_4]/AC	−30.20
ZnO	+ 29.50
ZnO/AC	+7.30
[Fe/g-C_3N_4]/ ZnO	+21.62
[Fe/g-C_3N_4]/ZnO/AC	+ 18.88

The g-C_3N_4 sample presented a strongly negative zeta potential of −30.16 mV, which can be attributed to the high electron density and nitrogen-containing functional groups present in the carbon nitride structure [102]. But after Fe incorporation, the Fe/g-C_3N_4 sample showed a less negative zeta potential (−21.13 mV), indicating partial charge neutralization caused by the coordination between Fe^{3+} ions and nitrogen sites in the carbon nitride framework [103]. The [Fe/g-C_3N_4]/AC composite exhibited a more negative surface charge (−30.20 mV), suggesting that the combined contribution of negatively charged clay and nitrogen functional groups increases the overall surface electron density [76].

On the opposite, pure ZnO sample exhibits a strongly positive zeta potential of +29.50 mV, resulting from protonation of surface hydroxyl groups [104]. When ZnO is immobilized on activated clay (ZnO/AC sample), the zeta potential drops dramatically to +7.30 mV, demonstrating significant charge neutralization through electrostatic interaction between the positive ZnO nanoparticles and the negative clay support [76]. The [Fe/g-C_3N_4]/ZnO composite maintains a strong positive charge of +21.62 mV, showing that ZnO nanoparticles dominate the surface charge behavior of the composite. Indeed, ZnO nanoparticles are located at the surface of the composite [102]. Finally, the ternary [Fe/g-C_3N_4]/ZnO/AC composite displays a positive potential of +18.88 mV, representing a balanced contribution from all three components where ZnO's positive charge is partially neutralized by the combined negative charges of AC and Fe/g-C_3N_4, confirming successful heterostructure formation to enhance adsorption and photocatalytic activity toward anionic dye pollutants [76].

These zeta potential variations directly correlate with the electrostatic assembly mechanisms and interfacial charge transfer processes that are essential for enhanced photocatalytic performance, as the positive surface charges of ZnO-containing composites favor adsorption of anionic dye pollutants, while the charge neutralization between components indicates intimate heterojunction formation that promotes charge separation [105, 106].

3.5 DRS analysis

Figure 50 shows the DRS spectrum of pure ZnO, which exhibited a well-defined absorption edge in the UV region approx. 380-400 nm, followed by a rapid decrease in reflectance and the band gap of ZnO was found to be 3.26 eV (Table 4). This is the usual characteristics behavior of ZnO due to its wide band gap semiconductor (~3.2–3.3 eV) corresponding to the electronic transition from the valence band to the conduction band [76, 107]. The steep drop indicates strong UV absorption and minimal absorption in the visible region, which is typical because pure ZnO is mostly inactive under visible light. This sharp absorption edge also denotes high crystallinity and uniform particle size distribution of the synthesized ZnO nanoparticles.

Table 4: Band gap of all samples

Sample	Band gap (eV)
g-C_3N_4	2.78 (direct)
g-C_3N_4	2.47 (indirect)
Fe/g-C_3N_4	2.36 (direct)
Fe/g-C_3N_4	0.61 (indirect)
ZnO	3.26
ZnO/AC	3.25
[Fe/g-C_3N_4]/ZnO	3.20 (direct)
[Fe/g-C_3N_4]/ZnO	2.94 (indirect)
[Fe/g-C_3N_4]/ZnO/AC	3.24 (direct)
[Fe/g-C_3N_4]/ZnO/AC	3.01 (indirect)

For the activated clay (AC), a broad absorption profile was observed across the UV-visible region with relatively lower intensity compared to ZnO sample and no sharp absorption edge was also not seen, which confirms the non-semiconducting/insulating nature of the activated clay. This diffuse absorption pattern is typical for amorphous aluminosilicate materials, where the absorption arises from the structural defects, impurities and charge transfer transition within the clay lattice [108, 109]. Such behavior is widely reported since clay minerals lack a defined band gap and mainly act as support materials rather than photoactive materials [110].

The ZnO/AC composite shows an intermediate behavior between ZnO and AC samples, which demonstrated a slight, red shift absorption edge compared to pure ZnO, extending further into the visible light region. This shift suggests successful electronic interactions between ZnO nanoparticles and clay support matrix. The band gap of the composite was found to be 3.25 eV which is slightly reduced compared to pure ZnO (Table 4). The enhanced visible-light absorption capability of the composite can be attributed to the formation of the interface states and defect levels introduced by the clay structure, which effectively reduce the band gap of ZnO [108]. Consistent observations have been documented for ZnO nanocomposites supported on clay, where the clay matrix functions as an enhancer of surface activity, thereby modifying the optical properties of the ZnO nanoparticles [76].

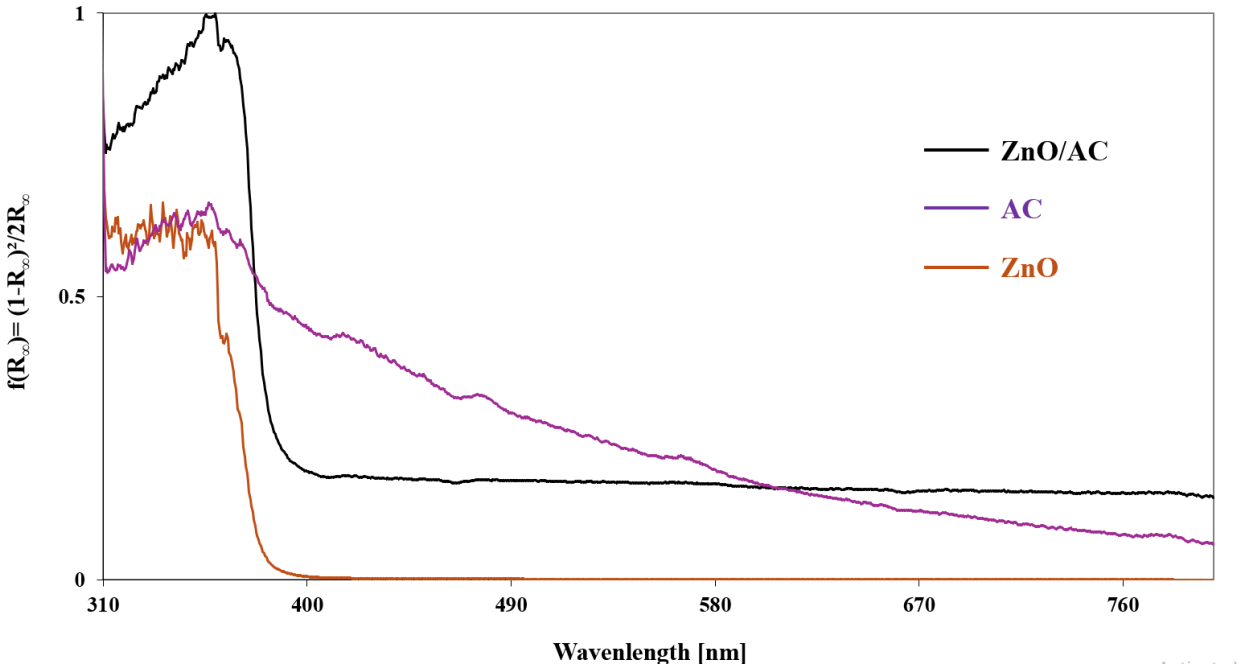

Figure 50: UV-Vis DRS curves of ZnO/AC, AC and ZnO samples

Pure g-C_3N_4 exhibits a typical absorption edge between 430-450 nm, corresponding to a band gap of 2.78 eV (direct) and 2.47 eV (indirect) shown in Figure 51. This absorption edge confirms that g-C_3N_4 is a visible-light responsive semiconductor indicating typical π–π* electronic transitions in the conjugated structure and limited absorption beyond approximately 450 nm. This behavior is consistent with literature for pure g-C_3N_4 [110, 111].

But upon Fe doping (Fe/g-C_3N_4) the absorption edge shifts toward longer wavelengths with a significant increase in visible-light absorption, which is attributed to the formation of impurity energy levels with the band structure [112]. The absorption edge showed a clear red shift and a broader absorption tail compared to pure g-C_3N_4 sample with significantly enhanced absorption intensity across the entire visible region 450-650 nm. This shift indicates successful incorporation of Fe^{3+} ions into the g-C_3N_4 matrix. The band gap also reduced after Fe doping in both case indirect (0.61 eV) and direct (2.36 eV) which is due to the introduction of iron creating intermediate energy level within the band gap of g-C_3N_4. It facilitates the sub-band gap transitions and improves visible-light harvesting. Similar observations such as red shift, reduced band gap and visible-light enhancement are widely reported by [113, 114] for Fe doped g-C_3N_4. Additionally, Fe act as a charge carrier mediator, improving the light absorption and potentially reducing electron-hole recombination.

Furthermore, the [Fe/g-C_3N_4]/AC composite shows a broadened absorption spectrum and enhanced light harvesting capability, indicating strong interfacial interactions between the semiconductor and the clay support. This clay supported facilitates improved photons utilization and is consistent with previously reported Fe-doped g-C_3N_4 and clay-based composite systems, in which band gap narrowing and enhanced visible-light absorption were observed [115].

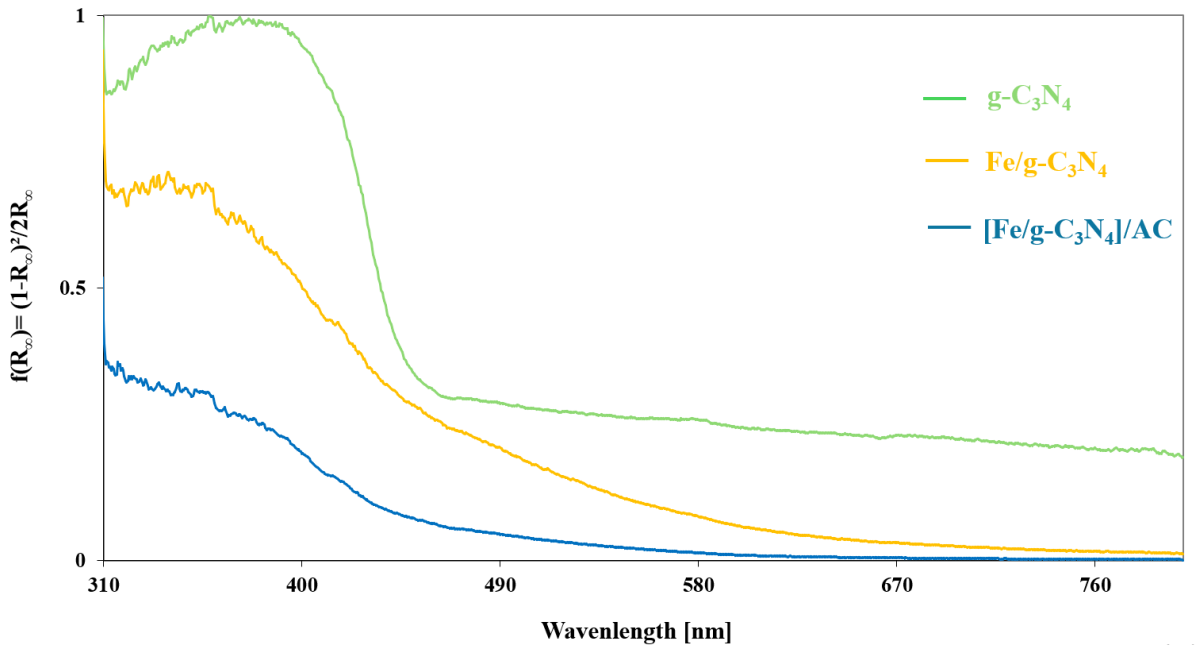

Figure 51: UV-Vis DRS curves of [Fe/g-C_3N_4]/AC, Fe/g-C_3N_4 and g-C_3N_4 samples

In Figure 52, it was observed that pure ZnO sample exhibits a characteristic absorption edge in the UV region (approx. 380 nm), indicating its wide band gap and limited visible-light activity while the ZnO/AC composite shows a slight enhancement in absorption due to improved dispersion of ZnO nanoparticles and surface interactions between ZnO and AC.

In contrast, the [Fe/g-C_3N_4]/ZnO composite showed a significant red shift and enhanced visible-light absorption having a band gap of 3.20 eV (direct) and 2.94 eV (indirect). As a significant shift of the absorption edge toward longer wavelengths along with strong visible-light absorption tail (400–600 nm) and narrowing band gap is observed for this composite which also confirms the formation of a heterojunction between ZnO and Fe/g-C_3N_4 and the Fe-induced defect states. This type of characteristic is also noticed in the work of [116] where ZnO based binary composite exhibits a red shift absorption edge compared to both individual components.

Furthermore, the ternary composite [Fe/g-C_3N_4]/ZnO/AC showed an absorption edge like ZnO with somewhat less band gap than ZnO. However, the band gap for this composite was found to be 3.24 eV (direct) and 3.01 eV (indirect) which is little more than [Fe-g-C_3N_4]/ZnO composite. This behavior indicates a synergistic interaction among the three components of the composite. The combination of ZnO (UV-active) and Fe-g-C_3N_4 (visible-active) broadens the absorption range, enabling better solar light utilization where the formation of a heterojunction promotes efficient charge separation and suppresses electron-hole recombination. Meanwhile, the activated clay enhances surface area, dispersion, and adsorption capacity, further facilitating charge transfer and improving overall photocatalytic performance. This type of enhanced optical response is consistent for ZnO based ternary composite and observed in the work of [84] where the formation of ZnO/Fe_3O_4/g-C_3N_4 composite leads to band gap narrowing and improved visible-light utilization.

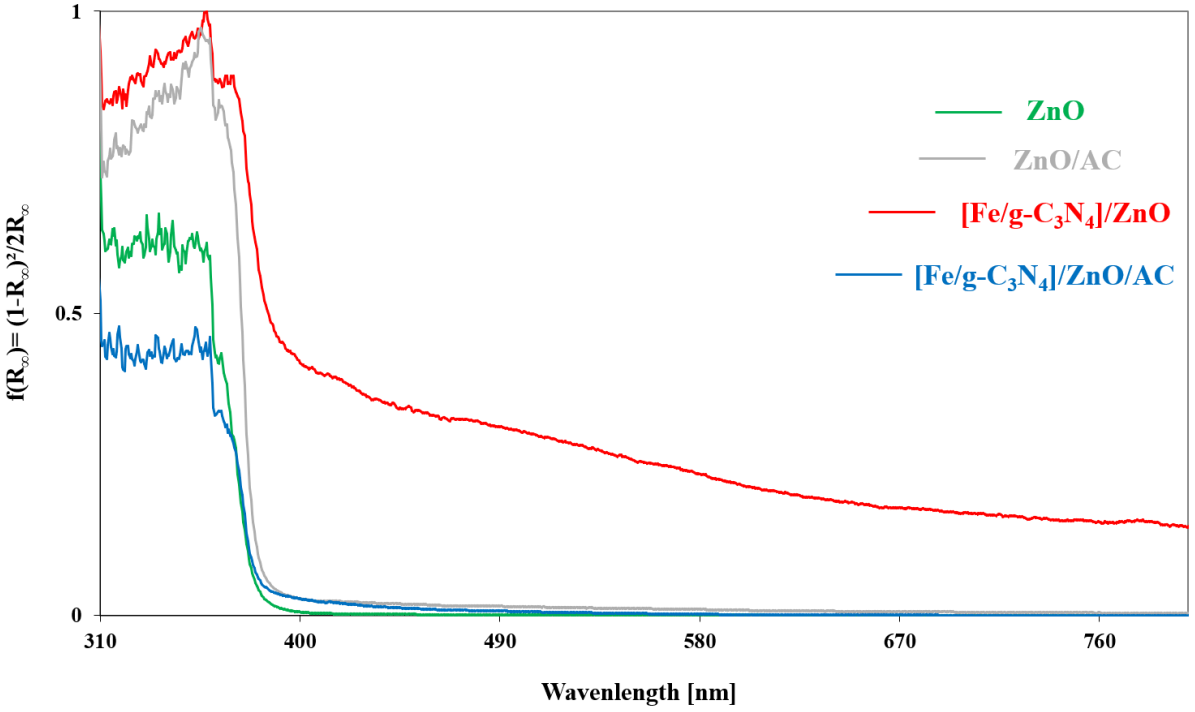

Figure 52: UV-Vis DRS curves of [Fe/g-C_3N_4]/ZnO/AC, [Fe/g-C_3N_4]/ZnO, ZnO/AC and ZnO samples

3.6 XPS analysis

Figure 53 (a) shows the XPS survey spectra of g-C_3N_4 and Fe/g-C_3N_4 samples. The presence of C, N, and O elements were confirmed in sample g-C_3N_4, while Fe/g-C_3N_4 sample additionally exhibited Fe 2p peaks, confirming successful incorporation of Fe species into the g-C_3N_4 framework. For the pure g-C_3N_4 sample, the high-resolution N 1s spectrum revealed three distinct peaks at 399.1 eV, 400.2 eV, and 405.0 eV. According to the literature, these peaks correspond to sp^2-hybridized nitrogen atoms in triazine rings (C=N–C), tertiary nitrogen N–$(C)_3$ groups, and amino functions (–NH_2), respectively. A weak shake-up peak was also observed at 405.0 eV, which is attributed to π–π* excitation in the conjugated aromatic structure of graphitic carbon nitride. The C 1s spectrum showed peaks centered at 284.8, 286.2, 288.6, and 289.1 eV, corresponding to graphitic carbon (C–C/C=C), C–O or C–N bonding, N=C–N coordination in the heptazine ring, and surface oxygenated carbon species, respectively. These features are characteristic of polymeric graphitic carbon nitride [58].

After Fe incorporation, noticeable shifts in binding energies were observed in Figure 53 (b). The Fe/g-C_3N_4 sample exhibited an Fe $2p_{3/2}$ peak at 710.7 eV, confirming the presence of Fe species, mainly Fe^{3+}/Fe^{2+} oxide states. The N 1s peaks exhibited slight low-shifts and intensity redistributions compared to pure g-C_3N_4. The peak at 398.8 eV (attributed to C=N–C) decreased in relative intensity, suggesting coordination interactions between Fe ions and the lone pair electrons of nitrogen atoms in the heptazine units. This observation is consistent with previous reports where Fe^{3+} ions are embedded into the g-C_3N_4 framework through Fe–N coordination bonds. The O 1s spectrum of g-C_3N_4 exhibited a peak at 533.1 eV attributed to adsorbed water or surface hydroxyl groups. After Fe doping, the O 1s peak shifted to lower binding energy 531.1 eV, suggesting the presence of Fe–O–H or Fe–O–C interactions and altered surface electronic density. Furthermore, the Fe/g-C_3N_4 sample showed increased oxygen content and modified carbon environments, suggesting that Fe doping introduced surface defects and promoted charge redistribution within the g-C_3N_4 structure. Similar trends are also observed in the study of [110]. Such electronic interactions are beneficial for suppressing electron–hole recombination and improving photocatalytic performance.

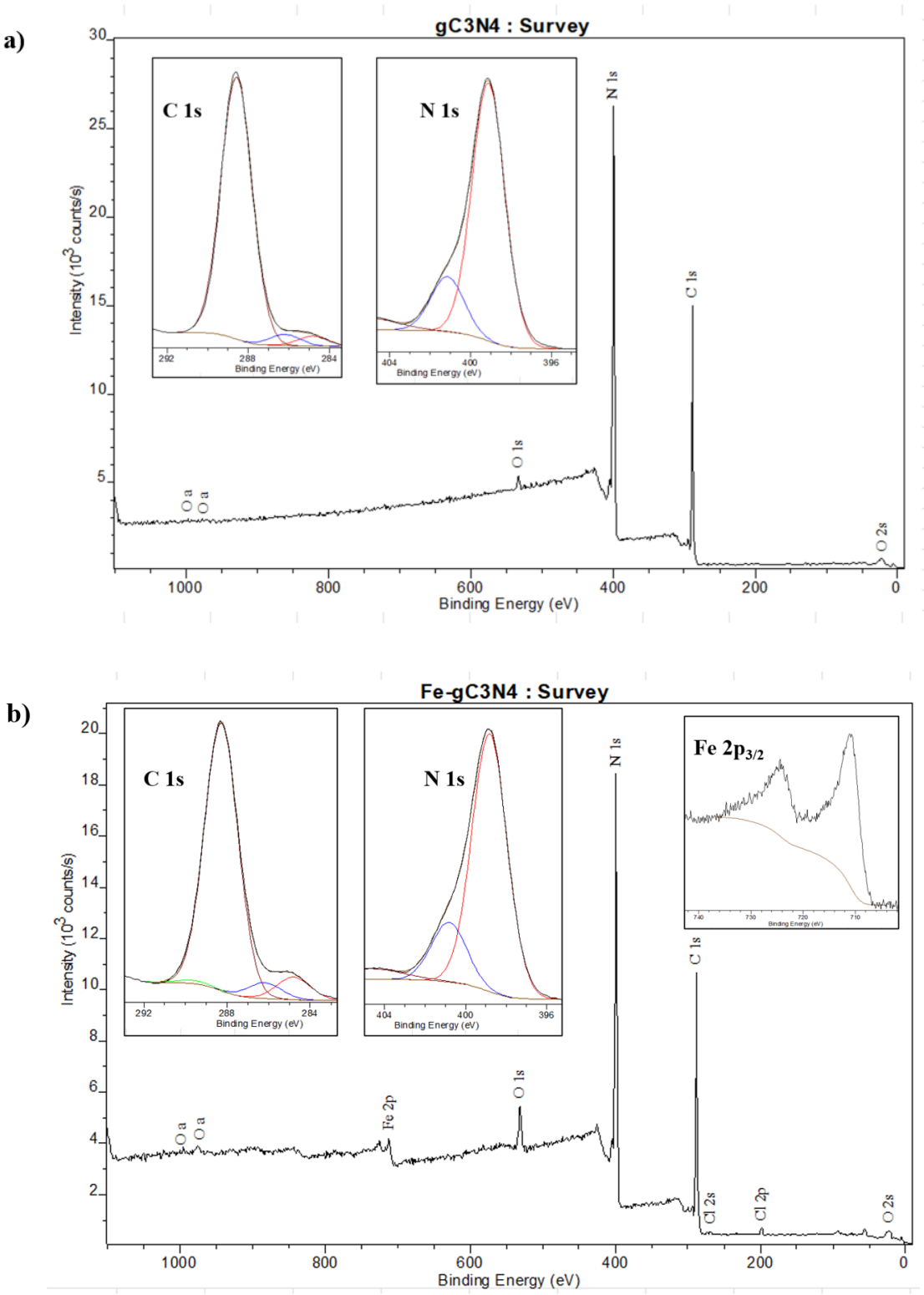

Figure 53: XPS spectra of (a) g-C_3N_4 and (b) Fe/g-C_3N_4 samples

In Figure 54 (a), the XPS spectrum of AC mainly consisted of O 1s and Si 2p peaks, confirming the aluminosilicate structure of halloysite clay [117]. The Si 2p peak observed at 103.8 eV corresponds to Si–O–Si bonding of silicate layers, while the O 1s peak at 533.1 eV is attributed to lattice oxygen and surface hydroxyl groups [118]. The low carbon contribution observed at 284.8-288.7 eV originated from adventitious carbon and surface functional groups formed during activation treatment. The high oxygen and silicon atomic percentages further confirm the silica-rich nature of halloysite activated clay. However, the absence of an Al peak in the XPS spectrum of acid-treated halloysite activated clay can be attributed mainly to the dealumination effect caused by acid treatment. During acid activation, strong acids selectively leach aluminum species from the octahedral layers of halloysite, resulting in significant removal of surface Al atoms and enrichment of silica (SiO_2) on the surface. Since XPS is a surface-sensitive technique that analyzes only the top few nanometers of the material, the reduction of surface aluminum concentration below the detection limit can lead to the disappearance or very weak intensity of the Al 2p peak. The dominant Si 2p and O 1s peaks observed after treatment therefore indicate that the clay surface became highly silica-rich after acid leaching [41].

Upon incorporation of Fe/g-C_3N_4 to form the [Fe/g-C_3N_4]/AC composite, significant changes in elemental composition and binding energies were observed in Figure 54 (b). The appearance of Fe $2p_{3/2}$ at 712.3 eV confirmed successful immobilization of Fe/g-C_3N_4 onto the clay surface. But the Si 2p peak was observed and shifted from 103.8 to 105.2 eV, indicating strong interfacial interaction between halloysite and Fe/g-C_3N_4. But the Fe 2p signal in the composite (712.3 eV) was slightly lower than in pure Fe/g-C_3N_4 (Figure 53), possibly due to dilution by the AC matrix. The O 1s peak also shifted toward higher binding energy (534.2 eV), suggesting the formation of interfacial hydrogen bonding or Fe–O–Si interactions between clay hydroxyl groups and Fe/g-C_3N_4. Moreover, the N 1s signals at 398.6 and 400.8 eV confirmed the successful incorporation of g-C_3N_4 onto the activated clay matrix. The increase in carbon and nitrogen contents in the composite compared with AC demonstrates effective loading of Fe/g-C_3N_4 onto the clay support. The interactions between the clay surface and Fe/g-C_3N_4 likely improved dispersion of active sites and facilitated interfacial charge transfer, which can enhance photocatalytic activity and stability. Similar observations have been reported for g-C_3N_4/clay composites where electrostatic interactions and hydrogen bonding facilitate heterojunction formation [47, 119].

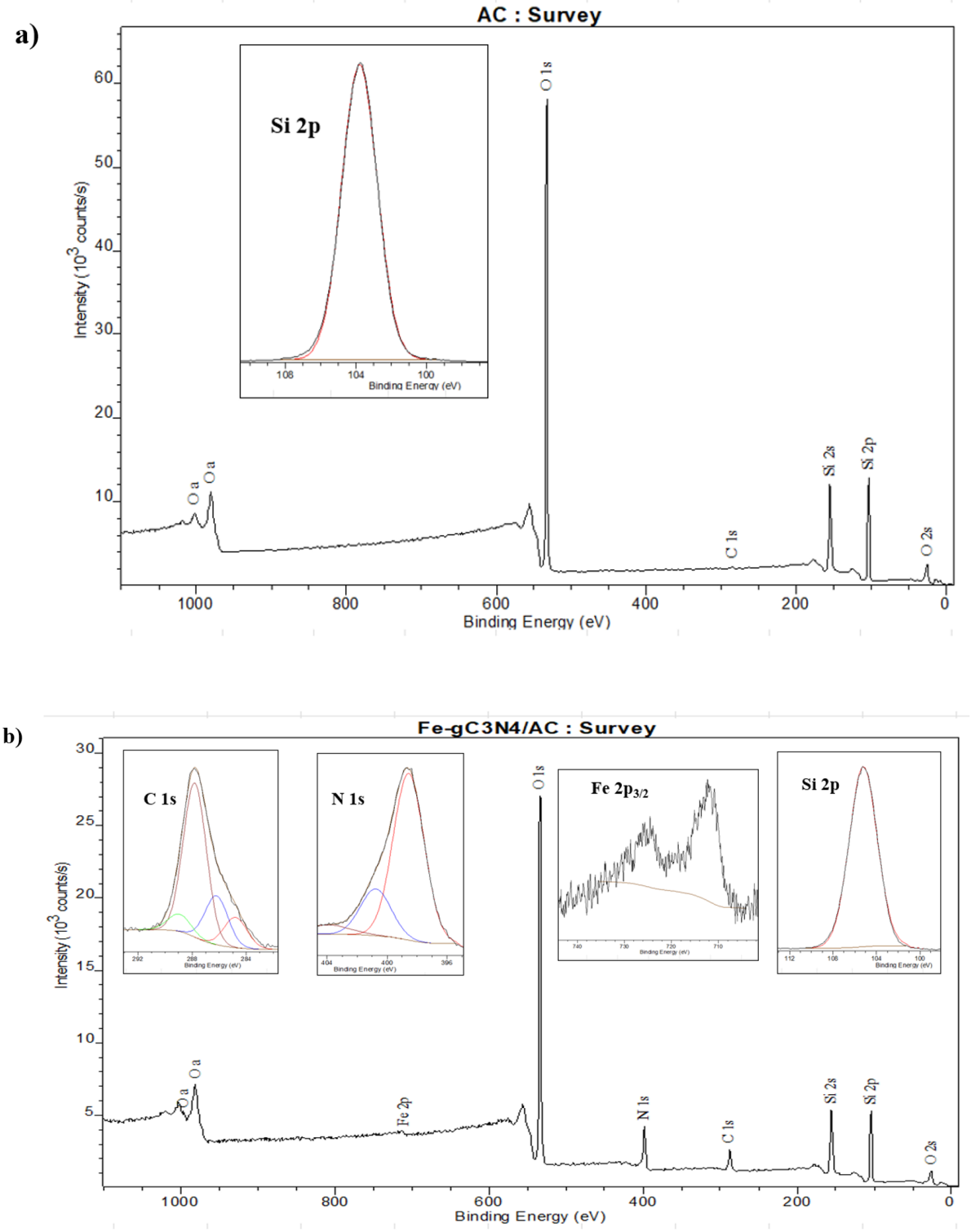

Figure 54: XPS spectra of (a)AC and (b) [Fe/g-C_3N_4]/AC samples

Figure 55 (a) represent the XPS spectrum of pristine ZnO which exhibited characteristic Zn $2p_{3/2}$ and O 1s peaks at 1021.7 and 530.6 eV, respectively, confirming the formation of Zn^{2+} species in ZnO. The binding energy separation between Zn 2p peaks corresponds to the typical ZnO wurtzite structure [120]. The O 1s peak mainly originated from lattice oxygen in Zn–O bonds. Minor carbon peaks observed at 284.8-289.2 eV were associated with surface adsorbed carbon species.

For the ZnO/AC composite (Figure 55 (b)), the Zn $2p_{3/2}$ peak slightly shifted to 1021.8 eV, while the O 1s peak shifted to 533.2 eV. These increase shifts in binding energy indicate that the surface hydroxyl groups and silanol groups (Si–OH) present in activated clay interact with ZnO, electrons are partially transferred from ZnO toward the clay surface, and Zn atoms become slightly electron deficient. The appearance of a strong Si 2p peak at 103.9 eV further confirmed successful deposition of ZnO on the clay surface. The increased oxygen contribution suggests the presence of additional surface hydroxyl groups and interfacial oxygen species, which may enhance adsorption and photocatalytic reactions.

In the [Fe/g-C_3N_4]/ZnO binary composite (Figure 55 (c)), Zn $2p_{3/2}$ and Fe $2p_{3/2}$ peaks appeared at 1021.6 and 710.0 eV, respectively, confirming coexistence of ZnO and Fe/g-C_3N_4. The N 1s peaks at 398.8 and 400.8 eV verified the presence of graphitic carbon nitride in the composite. Compared with pure ZnO and g-C_3N_4 samples, decrease shifts in Zn 2p, Fe 2p, and O 1s binding energies were observed, indicating strong interfacial electronic coupling between ZnO and Fe/g-C_3N_4. A decrease in binding energy indicates an increase in electron density around the atom. This occurs when electron transfer from Fe/g-C_3N_4 toward ZnO may occur under equilibrium conditions. Since g-C_3N_4 is rich in nitrogen atoms with lone-pair electrons, it can donate electron density to ZnO at the interface. As a result, Zn atoms become more electron rich, the electrostatic attraction between Zn nuclei and core electrons decreases, lower energy is required to remove the core electrons, and the Zn 2p peak shifts toward lower binding energy. Similarly, oxygen atoms near oxygen vacancies or defect sites may also show reduced binding energy due to localized electron accumulation. Such coupling facilitates charge transfer across the heterojunction interface and suppresses recombination of photogenerated electron–hole pairs. The increased carbon and nitrogen contents also confirm intimate integration of the two semiconductors.

The ternary [Fe/g-C_3N_4]/ZnO/AC composite (Figure 55 (d)) exhibited all characteristic peaks of Zn, Fe, C, N, O, Si, and Cl, demonstrating successful formation of the ternary heterostructure. The Zn $2p_{3/2}$ peak appeared at 1021.8 eV and the Fe $2p_{3/2}$ peak at 710.9 eV, while the O 1s peak shifted to 532.7 eV. The simultaneous presence of Si 2p at 103.5 eV and N 1s peaks at 398.4 and 400.5 eV confirms incorporation of both halloysite clay and Fe/g-C_3N_4 into the ZnO matrix. The Zn 2p binding energy in the ternary composite (1021.8 eV) is slightly higher than in pure ZnO (1021.6 eV), indicating electron transfer from ZnO to the other components.

Compared with the binary composites, additional shifts in binding energies were observed, suggesting strong interfacial interactions among ZnO, Fe/g-C_3N_4, and AC. These shifts indicate redistribution of electron density and formation of heterojunction interfaces, which can improve charge separation efficiency. These shifts occur because, upon composite formation, electrons redistribute between ZnO and the coupled materials until their Fermi levels reach equilibrium. Additionally, the formation of interfacial bonds such as Zn–O–Si, Zn–O–Fe, or Zn–N modifies the chemical environment of Zn and O atoms, causing changes in the core electron binding energies. The ternary composite also exhibited higher oxygen and silicon contents due to the clay support, while maintaining significant Zn and Fe signals. The synergistic interaction among ZnO, Fe/g-C_3N_4, and activated clay is expected to enhance visible-light absorption, increase active surface sites, and promote interfacial charge migration, leading to superior photocatalytic activity compared with the individual and binary systems. These observations align with reports on ternary composite systems where synergistic effects enhance charge carrier separation [76, 82-84, 120].

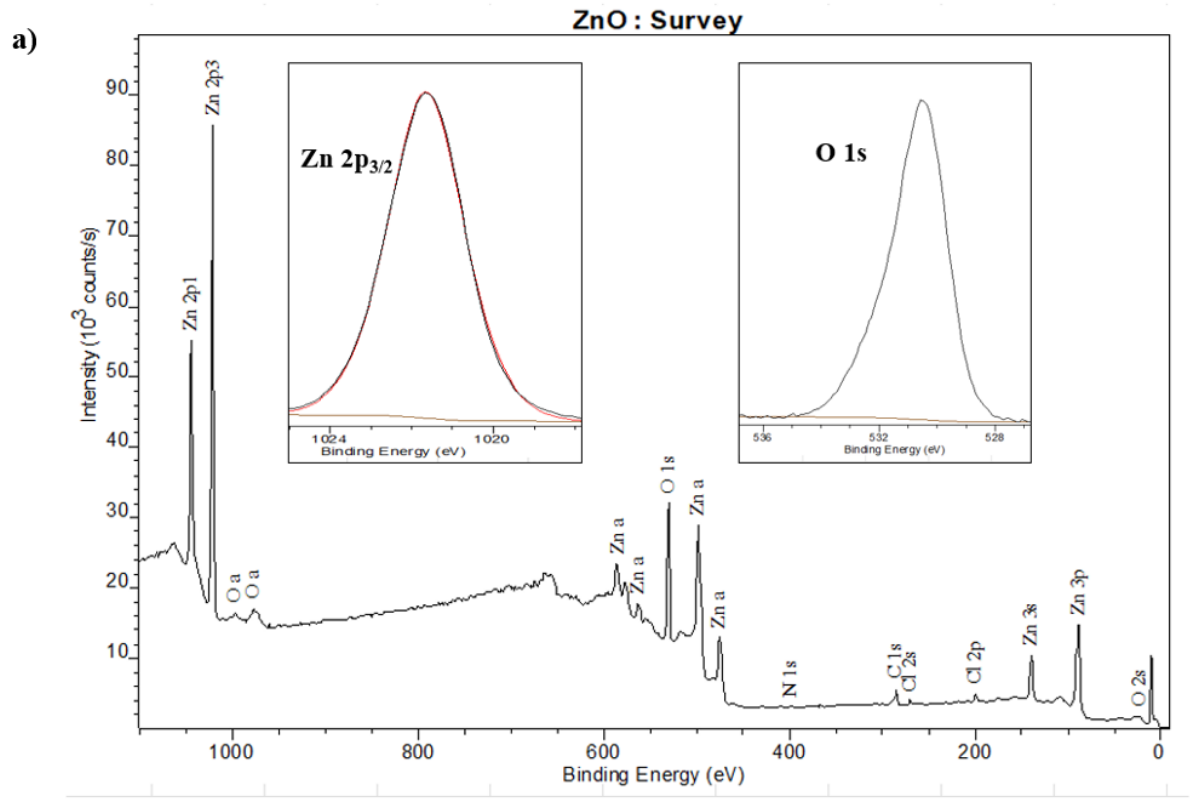

b)

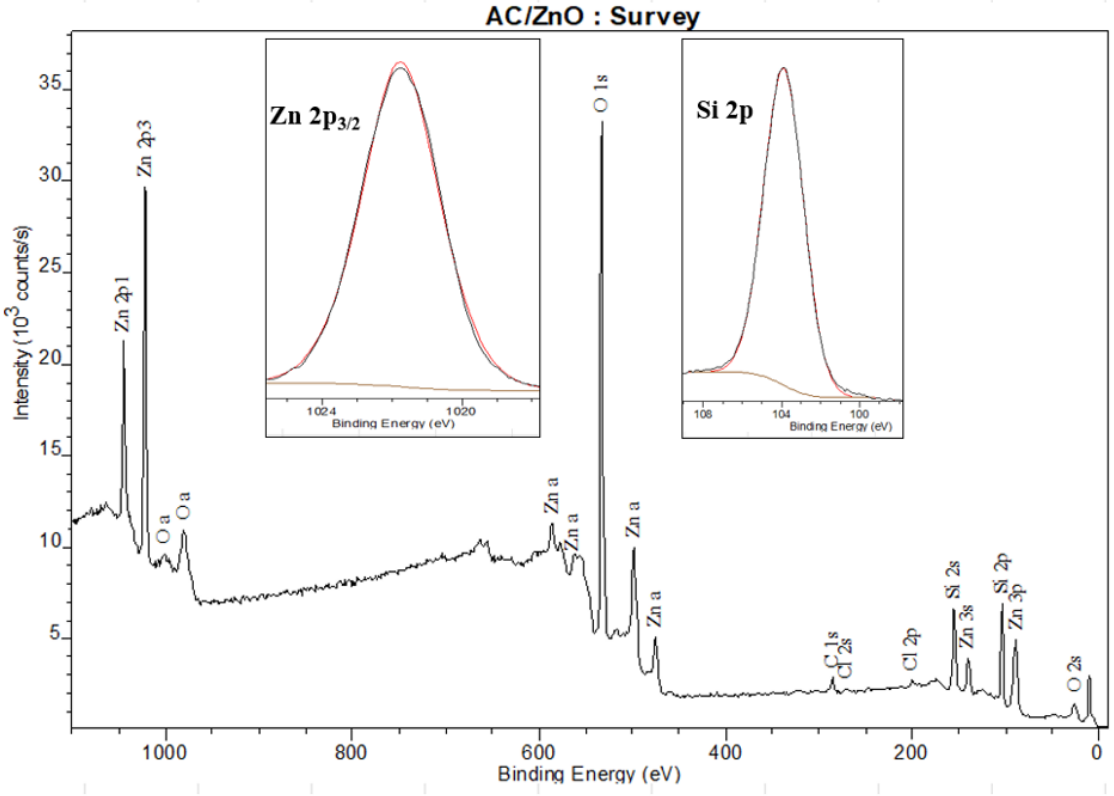
AC/ZnO : Survey
Zn 2p3
Zn 2p1
O 1s
Zn 2p3/2
Si 2p
Intensity (10^3 counts/s)
Binding Energy (eV)
O a
Zn a
Fe 2p
N 1s
Cl 2p
Si 2s
Si 2p
Zn 3s
Zn 3p
O 2s

c)

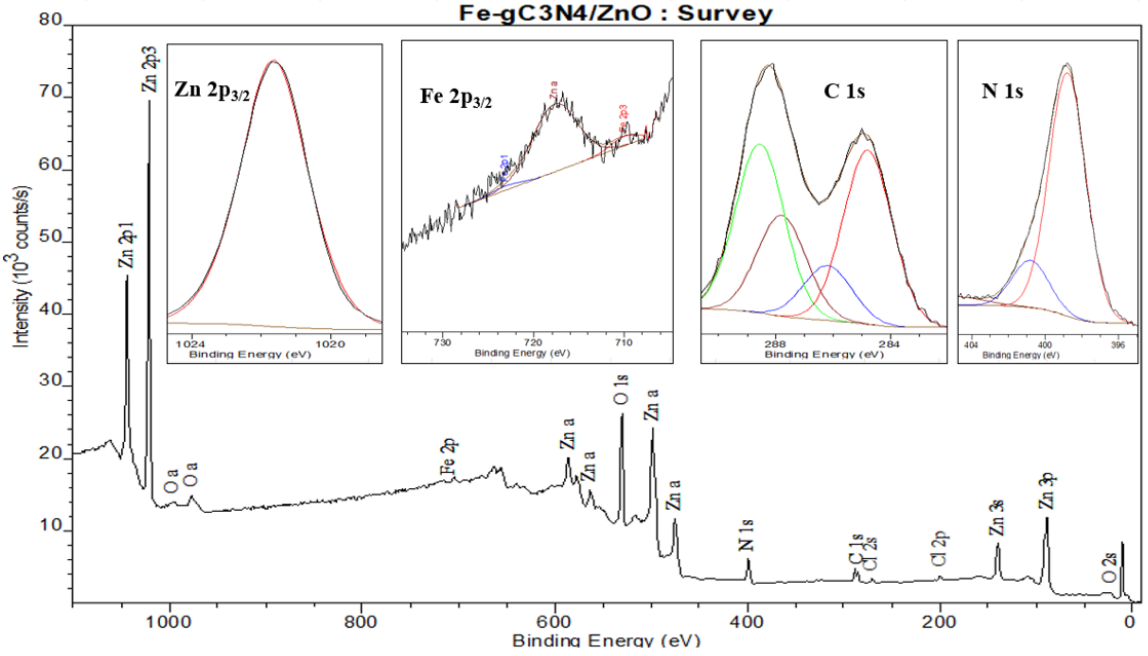
Fe-gC3N4/ZnO : Survey
Zn 2p3
Zn 2p1
Zn 2p3/2
Fe 2p3/2
C 1s
N 1s
O 1s
Intensity (10^3 counts/s)
Binding Energy (eV)
O a
Zn a
Fe 2p
N 1s
Cl 2p
Zn 3s
Zn 3p
O 2s

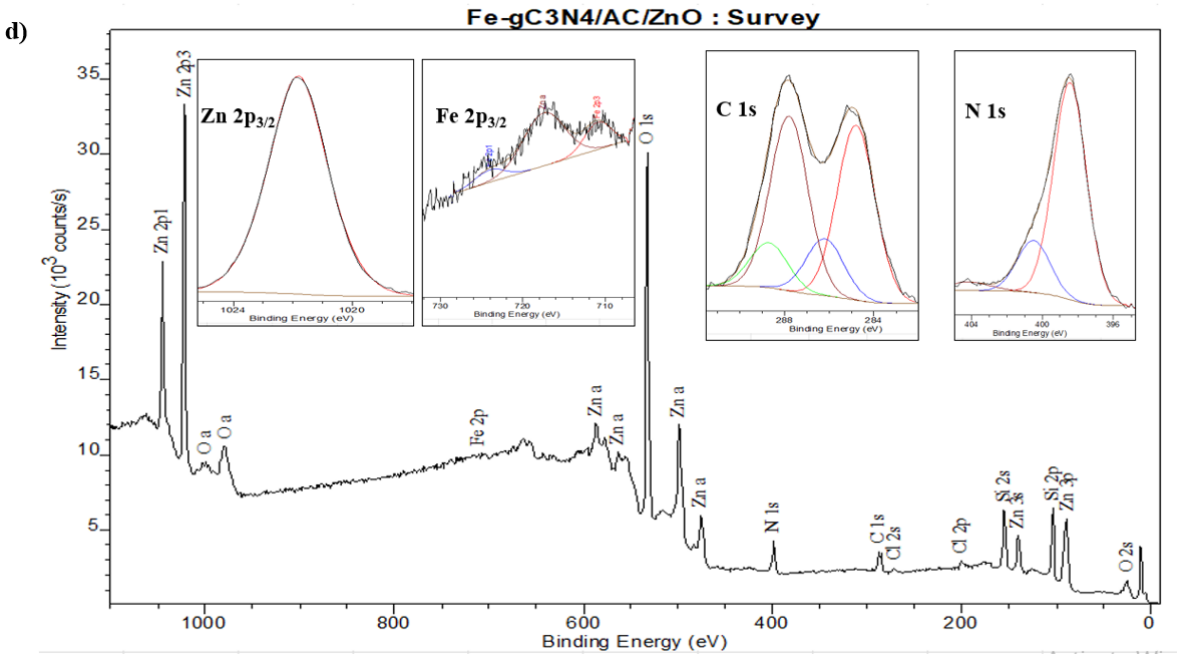

Figure 55: XPS spectra of (a) ZnO, (b) ZnO/AC, (c) [Fe/g-C_3N_4]/ZnO and (d) [Fe/g-C_3N_4]/ZnO/AC samples

3.7 Photocatalytic degradation analysis

Figure 56 shows the visual observations during the degradation of RB5 for all the samples at time = 0, 2, 4, 6 and 8 h where Figure 57 (a) presented the evolution of RB5 concentration as a function of time, and Figure 57 (b) presented the percentage (%) of RB5 degradation as a function of time. Before photocatalytic degradation, the samples were kept in the dark for 30 min to establish adsorption-desorption equilibrium. In this initial stage, dye removal is primarily due to surface adsorption rather than photocatalytic activity. Pure g-C_3N_4 sample exhibited very low adsorption (only 3 %), indicating limited surface-active sites. In contrast, ZnO and ZnO/AC samples showed a higher level of adsorption (around 15%), which can be attributed to ZnO surface positive charges, which interact with anionic RB5. Among all samples, [Fe/g-C_3N_4]/ZnO showed the highest initial adsorption percentage (22%), suggesting improved surface interaction, a greater number of active sites, and stronger dye affinity. Activated carbon (AC) typically enhances RB5 adsorption percentage due to its large specific surface area and porous volume, and its ability to form π–π interactions with the aromatic rings of RB5 dye molecules.

Figure 56: Visual observations of degradation of azo dye RB5 at definite time interval

Once exposed to light, all samples exhibited significantly photocatalytic degradation performance. This is attributed to the generation of electron–hole pairs and reactive oxygen species (including •OH and $O_2^{\bullet-}$ radicals), which promote the oxidative breakdown of RB5 molecules. Graphitic Carbon Nitride (g-C_3N_4) showed after 8 h, a RB5 degradation percentage equal to 82%. This result could be due to rapid charge recombination and low specific surface area (< 5 m^2/g, Table 2). Fe/g-C_3N_4 sample exhibited a similar final degradation percentage (80 %). Indeed, Fe doping can improve visible-light absorption and reduce charge recombination, but an excess of Fe^{3+} ions may act as recombination centers or block active sites [58]. In contrast, the [Fe/g-C_3N_4]/AC composite shows the lowest RB5 degradation percentage (58 %), as excessive activated carbon likely shields light penetration, reduces photon absorption, covers catalytic sites, and causes inefficient electron transfer, indicating a non-optimized heterostructure [47,119].

Zinc oxide (ZnO) sample showed photocatalytic performance after 8 h, equal to 83%, attributed to its high oxidation ability and efficient radical generation, though it still suffers from photo-corrosion and charge recombination [74]. The addition of activated carbon (ZnO/AC) significantly boosts degradation to 99 % by enhancing dye adsorption, dispersion, electron transport, and recombination suppression, creating a synergistic effect. The [Fe/g-C_3N_4]/ZnO sample achieved excellent RB5 degradation percentage (100 % after 8 h)) by promoting charge separation, extending light absorption, and increasing reactive radical production. Finally, the ternary composite [Fe/g-C_3N_4]/ZnO/AC delivered the highest efficiency (100 % after 6.5 h)) by combining AC's adsorption, Fe/g-C_3N_4's visible-light response, and ZnO's oxidation ability, where AC acts as an electron acceptor and an adsorption platform, leading to rapid mineralization and strong synergistic interactions among all three components.

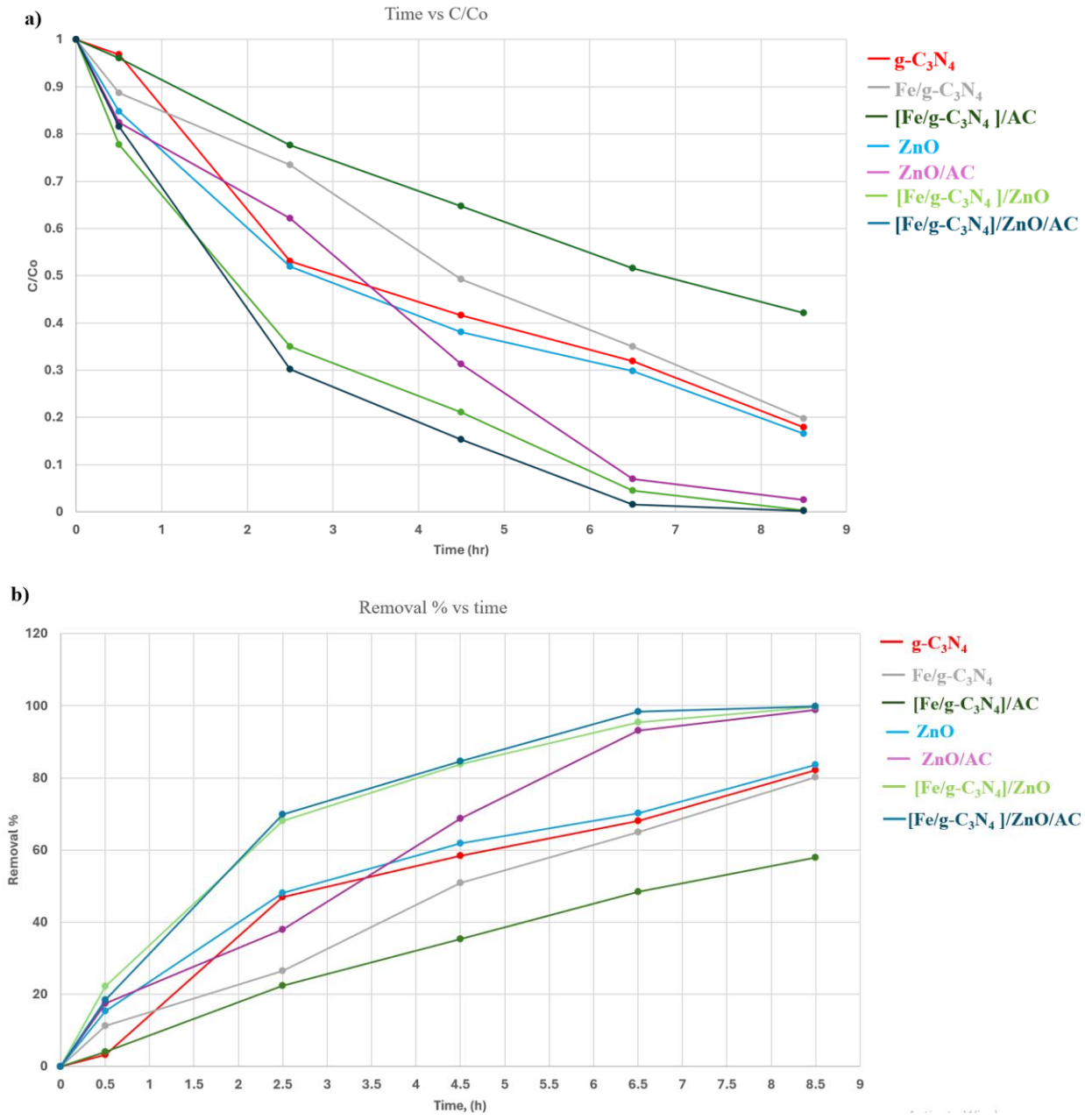

Figure 57: Degradation curves of RB5 (a) C/C_0 vs time and (b) removal % vs time

The enhanced photocatalytic activity of the [Fe/g-C_3N_4]/ZnO/AC ternary composite toward RB5 azo dye degradation is driven by synergistic interactions among the three components can be explained and shown in Figure 58. First ZnO with a band gap equal to 3.26 eV absorbs UV light ($\lambda < 380$ nm) and generates electron-hole pairs:

$$\mathrm{ZnO} + h\nu \rightarrow \mathrm{ZnO}(e^-_{\mathrm{CB}} + h^+_{\mathrm{VB}}) \ldots\ldots. (3.1)$$

Then Fe/g-C_3N_4 with an indirect band gap equal to 2.36 eV due to Fe doping absorbs visible light ($\lambda > 400$ nm) and generates electron-hole pairs:

$$\mathrm{Fe/g\ C_3N_4} + h\nu \rightarrow \mathrm{Fe/g\text{-}C_3N_4}(e^-_{\mathrm{CB}} + h^+_{\mathrm{VB}}) \ldots\ldots\ldots (3.2)$$

The heterojunction interfaces between ZnO and Fe/g-C_3N_4 facilitate efficient charge transfer. Due to appropriate band alignment, photogenerated electrons from the conduction band (CB) of Fe/g-C_3N_4 migrate to the CB of ZnO, while holes from the valence band (VB) of ZnO transfer to the VB of Fe/g-C_3N_4. This spatial separation suppresses electron-hole recombination. Here, activated clay (AC) acts as a high-surface-area support that disperses ZnO and Fe/g-C_3N_4 nanoparticles, preventing agglomeration. It serves as an electron acceptor/conductive bridge that traps and shuttles electrons, further reducing recombination. It also acts as adsorption enhancer that concentrates RB5 dye molecules near active sites via electrostatic and hydrophobic interactions (zeta potential data confirms surface charge favorable for anionic RB5 adsorption, Table 3). The separated electrons and holes react with adsorbed water, dissolved oxygen, and surface hydroxyl groups to produce highly reactive radicals.

Electrons (e^-) reduce dissolved oxygen to superoxide radicals ($O_2^{\bullet -}$):

$$e^- + O_2 \rightarrow O_2^{\cdot -} \ldots\ldots. (3.3)$$

Holes (h^+) oxidize water or hydroxyl ions to hydroxyl radicals (•OH):

$$h^+ + H_2O \rightarrow \cdot OH + H^+ \ldots\ldots\ldots (3.4)$$

$$h^+ + OH^- \rightarrow \cdot OH \ldots\ldots\ldots\ldots (3.5)$$

The Fe^{3+}/Fe^{2+} redox couple in Fe/g-C_3N_4 further promotes Fenton-like reactions, generating additional •OH radicals:

$$Fe^{2+} + H_2O_2 \rightarrow Fe^{3+} + \cdot OH + OH^- \ldots\ldots\ldots (3.6)$$

$$Fe^{3+} + e^- \rightarrow Fe^{2+} \ldots\ldots\ldots\ldots (3.7)$$

The highly oxidizing •OH and $O_2^{\bullet -}$ radicals attack the azo bonds (-N=N-) of RB5 molecules, which are the chromophore centers responsible for RB5 color. This attack leads to the cleavage of azo bonds by breakdown into smaller aromatic intermediates and resulting in ring opening and mineralization into harmless products:

$$\mathrm{RB5} + \cdot OH / O_2^{\cdot -} \rightarrow \mathrm{Intermediates} \rightarrow CO_2 + H_2O + SO_4^{2-} + NO_3^- \ldots\ldots (3.8)$$

Table 5: Synergistic role of each component in ternary composite

Component	Role in mechanism
ZnO	UV light absorption; primary source of electron-hole pairs
Fe/g-C_3N_4	Visible-light harvesting; Fe doping introduces mid-gap states and Fenton-like activity; extends absorption range; promotes charge separation
AC	High surface area for dye adsorption; electron conductive support; prevents agglomeration; enhances mass transfer

These results demonstrate that heterojunction engineering significantly improves photocatalytic activity by combining semiconductors to enhance charge separation. The inclusion of activated carbon further boosts adsorption and electron transport. Among all composites, the ternary [Fe/g-C_3N_4]/ZnO/AC photocatalyst completely degraded RB5 after 6.5 h due to the synergistic combination of enhanced adsorption capacity, improved charge separation, and efficient interfacial electron transfer between Fe/g-C_3N_4, ZnO, and activated clay. The heterojunction structure effectively suppressed electron-hole recombination, leading to enhanced production of reactive oxidative species responsible for dye degradation.

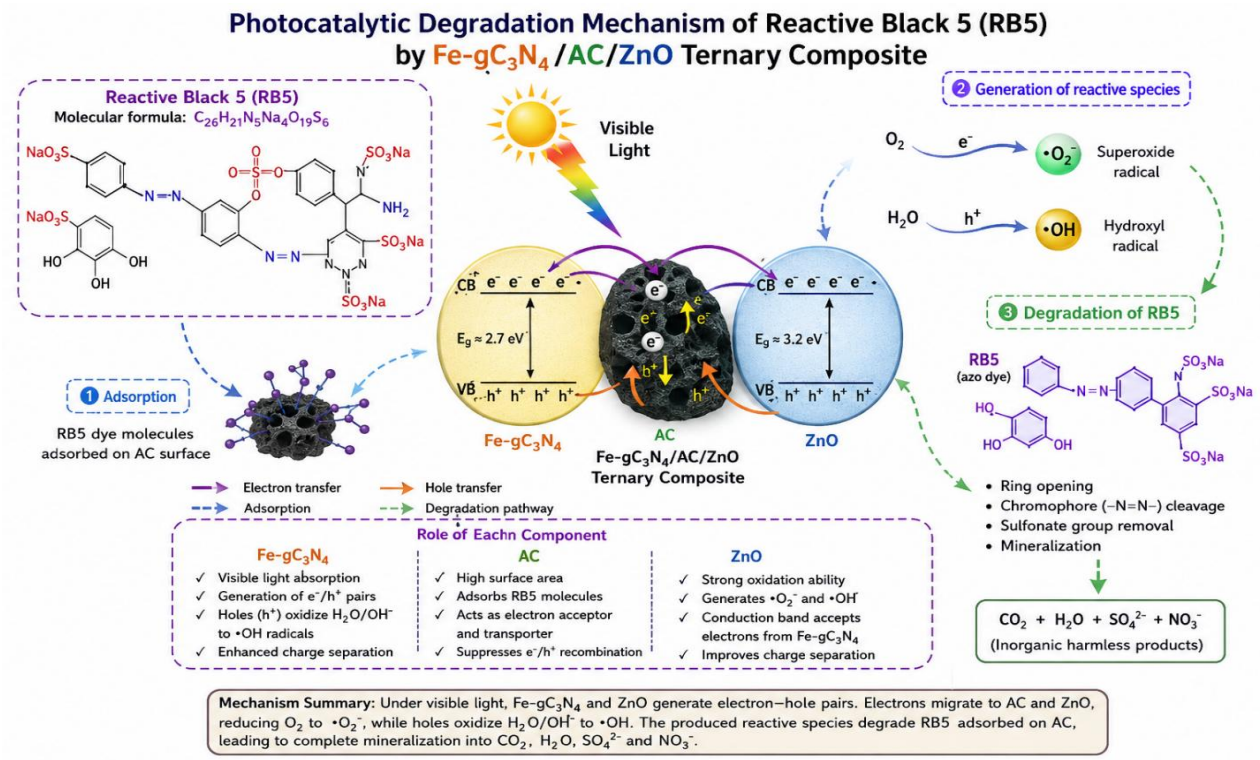

Figure 58: Expected mechanism of ternary composite in degrading RB5 dye in photocatalysis (generated by AI)

Therefore, for the ternary composite [Fe/g-C_3N_4]/ZnO/AC, the experiment was run again, and residual concentrations were recorded at 0, 0.5, 1.5, 2, 4, 6 and 8 h. The degradation kinetic for the photocatalytic process is often described by the Langmuir-Hinshelwood (L-H) model, which reduces to a pseudo-first-order equation at low dye concentrations:

$$\ln(C/C_0) = -kt \quad \text{(3.9)}$$

In this expression, C_0 and C represent the initial dye concentration and the concentration at time t, respectively, while k is the apparent first-order rate constant expressed in h^{-1}, and t denotes the irradiation time (h). First at 0, 0.5, 1.5, 2, 4, 6 and 8 h, the data are shown in Figure 59 (a) and in Figure 59 (b), only the first points (0-2 h) are presented. Figure 59 (a) shows the plot of $-\ln(C/C_0)$ versus irradiation time, with error bars representing the standard deviation (SD) of duplicate measurements at each time point summarized in Table 6. demonstrates good reproducibility. The coefficient of variation (CV) values ranged from 0% to 2.4% across all time points, with the majority below 2%, confirming high experimental precision and minimal random error. The small SD values (e.g., 0.0095 at 0.5 h, 0.0144 at 2 h) indicate that the duplicate runs were highly consistent.

At 4 h, the experimental value (1.897) deviates noticeably from the linear prediction, but the low SD (0.0285) and CV (1.5%) confirm a systematic kinetic deviation rather than random error. But at 6 h, the higher SD (0.0945) and CV (2.2%) suggest slight variability in recovery between duplicates, possibly due to differences in intermediate desorption or local *pH*. The near-zero SD at 8 h (0.0003) reflects identical endpoints due to reaction completion. These low error margins confirm good reproducibility of the Fe-g-C_3N_4 photocatalyst.

$$\bar{x} = \frac{x_1 + x_2}{2} \quad \text{(3.10)}$$

$$SD = \sqrt{\frac{\sum(x_i - \bar{x})^2}{n-1}} \quad \text{(3.11)}$$

$$CV(\%) = \frac{SD}{\bar{x}} \times 100 \quad \text{(3.12)}$$

Table 6: Kinetics data

Time (h)	-ln (C/Co) (1st)	-ln C/Co (2nd)	Average	Standard deviation, (SD)	coefficient of variation, (CV)
0	0.000	0.000	0.000	0.0000	0
0.5	0.387	0.400	0.394	0.0095	2.4%
1	0.596	0.607	0.601	0.0078	1.3%
1.5	0.863	0.877	0.870	0.0099	1.1%
2	1.197	1.217	1.207	0.0144	1.2%
4	1.877	1.917	1.897	0.0285	1.5%
6	4.135	4.269	4.202	0.0945	2.2%
8	6.215	6.215	6.215	0.0003	0.0%

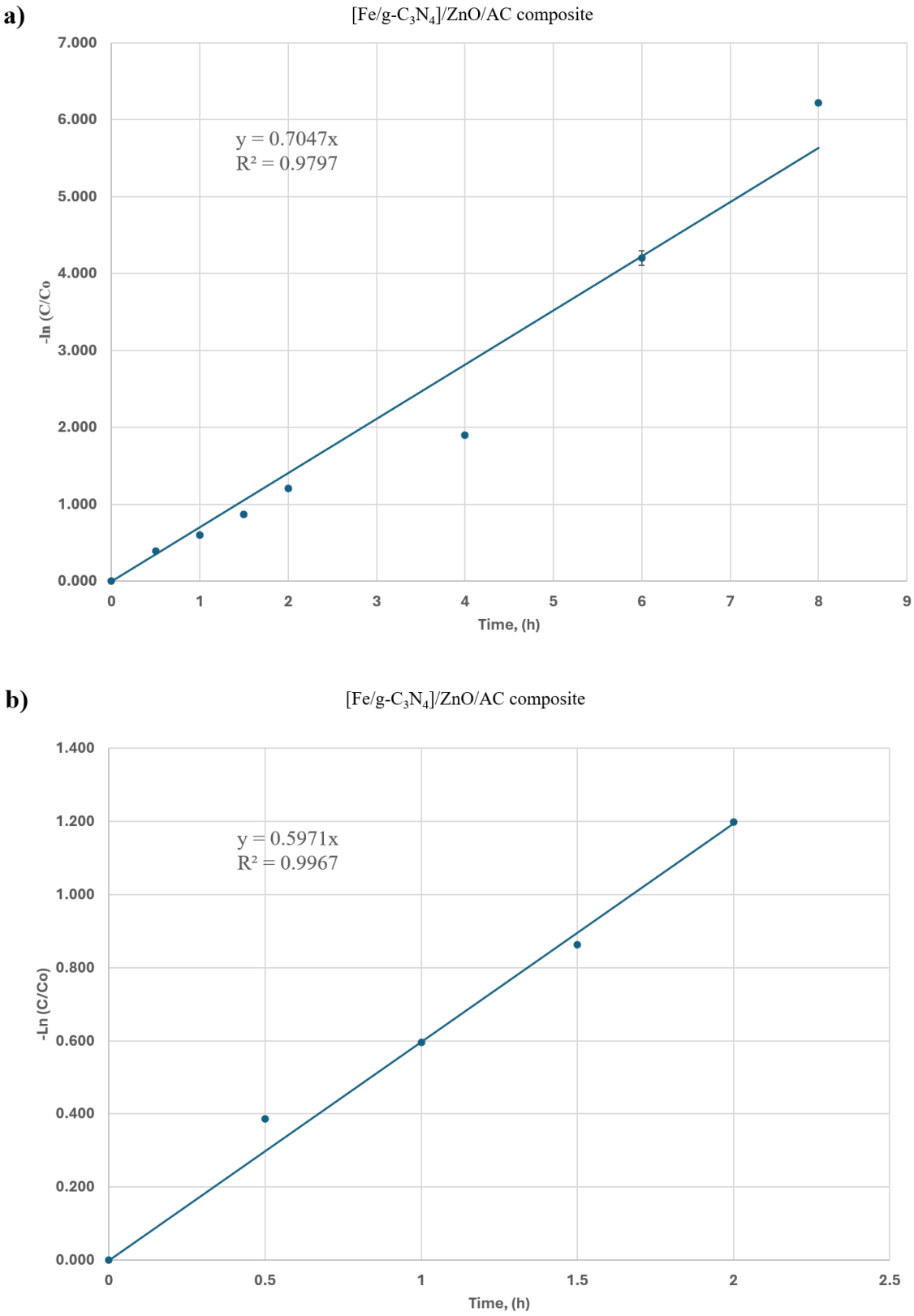

Figure 59: Pseudo-first-order kinetic of ternary composite after (a) 8 h and (b) 2 h

The kinetic analysis of the [Fe/g-C_3N_4]/ZnO/AC composite for 8 h yields a rate constant k = 0.704 h^{-1}, which is relatively high and indicates rapid RB5 degradation, efficient photocatalytic activity, fast generation of reactive oxygen species, and effective charge separation. The correlation coefficient $R^2 = 0.9797$, being very close to 1, confirms excellent linear fitting and strong agreement with pseudo-first-order kinetics, indicating that the degradation process is predominantly controlled by surface photocatalytic reactions. The pseudo-first-order behavior implies that the concentration of active radicals (•OH and O_2•$^-$) remains nearly constant during irradiation, so the degradation rate depends primarily on the RB5 concentration. Initially, abundant dye molecules allow rapid degradation, but as time increases and the dye concentration decreases, fewer molecules remain available for oxidation, causing the rate to gradually slow down and producing the observed logarithmic kinetic behavior. However, a closer inspection of the data reveals that the 4-hour data point lies slightly away from the fitted linear trendline. Possible explanations for this deviation include experimental variability in sampling or UV-Vis measurements, or minor inconsistencies during filtration and sample handling. The relatively higher standard deviation at 4 h suggests a transient, non-systematic fluctuation rather than a true trend change, especially since the 6 h point returns to the overall kinetic trend. Another possibility is a temporary shift in the reaction regime, where the system transitions from early-stage surface adsorption and radical attack to a stage influenced by intermediate byproducts competing for reactive species (•OH, •O_2^-). Additionally, partial degradation of RB5 may produce intermediates that temporarily re-adsorb on the catalyst surface, blocking active sites and causing a short-lived reduction in apparent rate before steady-state conditions are re-established. Minor variations in light intensity could also contribute, though this is less likely given the overall reproducibility of the dataset.

On the other hand, during the 2 h of irradiation, the kinetic analysis of the [Fe/g-C_3N_4]/ZnO/AC ternary composite shows a much better fit (R^2 = 0.9967) compared to the full eight-hour dataset (R^2 = 0.9797), indicating that pseudo-first-order kinetics are followed almost perfectly during the initial degradation stage. The rate constant derived from the first two hours is k = 0.597 h^{-1}, which represents the true initial degradation rate. During this early period, the dye concentration remains relatively high, active sites are freely available, light penetration is effective, radical generation is stable, and adsorption-desorption equilibrium is maintained, so the degradation rate depends primarily on dye concentration. After longer irradiation times, however, the dye concentration becomes very low, intermediate products accumulate, active sites may become partially occupied, and mass transfer limitations increase, causing slight deviations from ideal first-order behavior. The relatively high rate-constant (0.597 h^{-1}) reflects rapid photocatalytic degradation due to synergistic interactions among Fe-doped g-C_3N_4, ZnO, and activated clay, which improve visible-light absorption, charge separation, electron transfer, and reactive oxygen species formation.

Chapter 4: Conclusion and Perspectives

4.1 Conclusion

This study deals with successful formation of ZnO-based binary and ternary photocatalytic composite materials along with activated halloysite as clay support for enhancing the photocatalytic degradation of azo dyes Rb5 compared to mere ZnO. Halloysite nano clay was chemically acid treated to produce activated clay (AC), Fe-doped g-C_3N_4 was synthesized and ZnO nano particles was produced by precipitation method. Then different combination of binary and ternary composite was formed namely ZnO/AC, [Fe/g-C_3N_4]/ZnO, [Fe/g-C_3N_4]/AC and [Fe/g-C_3N_4]/ZnO/AC.

The SEM analysis confirms the successful fabrication of all synthesized photocatalysts. Pure g-C_3N_4 exhibits a compact, stacked layered structure, while Fe doping induces a wrinkled, exfoliated morphology with increased surface roughness and exposed active sites. The ZnO nanoparticles appear as agglomerated irregular clusters, but when incorporated into binary ([Fe/g-C_3N_4]/ZnO) and ternary ([Fe/g-C_3N_4]/ZnO/AC) composites, they become uniformly dispersed without significant aggregation. The ternary composite demonstrates the optimal heterostructure, where Fe/g-C_3N_4 sheets and ZnO nanoparticles are densely decorated onto the rough, porous activated clay matrix, promoting intimate interfacial contact and enhanced charge transfer pathways for improved photocatalytic performance.

XRD analysis confirms that raw halloysite exhibits characteristic dehydrated tubular structure, which becomes amorphous after calcination at 800 °C, while acid-treated activated clay maintains this amorphous structure with slightly increased intensity. For g-C_3N_4, Fe doping weakens the peak intensity and introduces small, highly dispersed FeOOH nanoparticles, confirming Fe^{3+} intercalation into the g-C_3N_4 interlayers. In the binary and ternary composites ([Fe/g-C_3N_4]/AC, ZnO/AC, [Fe/g-C_3N_4]/ZnO, and [Fe/g-C_3N_4]/ZnO/AC), the characteristic diffraction peaks of individual components become weaker or appear as broad humps due to the dilution effect from the amorphous clay matrix and good dispersion of nanoparticles, confirming successful integration without destroying original crystal structures, with ZnO remaining highly crystalline and surface-exposed as observed in SEM.

The textural properties revealed that activated clay (AC) exhibits the highest specific surface area (270 m^2/g) and total pore volume (0.48 cm^3/g) with a mixed Type I/IV isotherm, confirming successful generation of both microporous and mesoporous structures after acid treatment, whereas raw clay (55 m^2/g) and calcined clay (50 m^2/g) show only Type IV isotherms with mesopores. Pure g-C_3N_4, Fe/g-C_3N_4, and ZnO are non-porous materials (S_{BET} < 20 m^2/g) with negligible porosity. For binary and ternary composites containing activated clay, such as [Fe/g-C_3N_4]/AC (80 m^2/g), ZnO/AC (100 m^2/g), and [Fe/g-C_3N_4]/ZnO/AC (40 m^2/g), the surface area and pore volume increase significantly compared to their non-porous counterparts, and their Type IV isotherms confirm the presence of mesopores inherited from the clay support, which facilitates better dispersion of active components and improved accessibility of active sites.

Zeta potential measurement indicates that clay and g-C_3N_4-based samples are negatively charged (−20 to −30 mV), while ZnO-containing composites are positively charged (+7 to +29 mV). The ternary [Fe/g-C_3N_4]/ZnO/AC composite exhibits a positive potential (+18.88 mV), confirming successful heterostructure formation. These opposite surface charges promote electrostatic attraction of anionic RB5 dye and facilitate interfacial charge transfer for enhanced photocatalysis.

DRS analysis shows that pure ZnO exhibits a wide band gap (3.26 eV) with UV absorption only, while pure g-C_3N_4 shows visible-light absorption (2.78 eV direct). Fe doping significantly narrows the band gap of g-C_3N_4 (to 0.61 eV indirect) and induces a red shift with enhanced visible-light absorption due to Fe^{3+}-induced intermediate energy levels. The binary [Fe/g-C_3N_4]/ZnO and ternary [Fe/g-C_3N_4]/ZnO/AC composites demonstrate intermediate band gaps (3.20–2.94 eV) with broadened visible-light absorption, confirming successful heterojunction formation that extends light utilization from UV to visible region for improved photocatalytic performance.

XPS spectrum analysis ensure successful incorporation of Fe^{3+}/Fe^{2+} into the g-C_3N_4 framework via Fe–N coordination bonds, evidenced by the appearance of Fe 2p peaks and binding energy shifts in N 1s and C 1s spectra. For the activated clay, acid treatment causes dealumination, leaving a silica-rich surface (Si 2p, O 1s) with no detectable Al peak. In the binary and ternary composites ([Fe/g-C_3N_4]/AC, ZnO/AC, [Fe/g-C_3N_4]/ZnO, and [Fe/g-C_3N_4]/ZnO/AC), binding energy shifts in Zn 2p, Fe 2p, O 1s, and Si 2p indicate strong interfacial electronic interactions and electron redistribution among components, confirming successful heterojunction formation that facilitates charge transfer and suppresses electron-hole recombination.

Finally, in the photocatalytic degradation of RB5 among all synthesized samples, the ternary composite [Fe/g-C_3N_4]/ZnO/AC exhibited the best photocatalytic performance, achieving 100% degradation of RB5 dye in just 6.5 hours, followed by [Fe/g-C_3N_4]/ZnO (100% at 8 h. Kinetic analysis of the optimal ternary composite followed pseudo-first-order kinetics with a rate constant of 0.704 h^{-1} (R^2 = 0.979) over 8 hours, with an even better fit (R^2 = 0.996, k = 0.597 h^{-1}) during the initial 2-hour period, confirming rapid charge separation, enhanced visible-light absorption, and synergistic interactions among ZnO (UV-active), Fe/g-C_3N_4 (visible-active, Fe^{3+}/Fe^{2+} redox), and AC (adsorption/electron conductive support).

To conclude it can be said that the higher efficiency of the ternary composite results from the synergistic interactions between i.e ZnO provides UV activity, Fe/g-C_3N_4 enables visible-light harvesting and charge separation, while AC enhances adsorption and electron transfer-collectively suppressing the recombination and accelerating reactive oxygen species generation. Therefore, ZnO-based heterojunction composite can be promising photocatalyst for enhanced photocatalytic degradation of azo dyes.

4.2 Perspectives

While this study demonstrates the promising potential of the [Fe/g-C_3N_4]/ZnO/AC ternary composite for azo dye degradation, several terms remain for future exploration and practical application. Firstly, as this study was performed on synthetic solution of azo dye, therefore future studies should test the composite on real textile wastewater containing mixed dyes, salts, surfactants, and variable *pH* to evaluate its industrial robustness. This study also leaves the room to systematically investigate the composite's reusability, recyclability, component leaching, and regeneration for cost-effectiveness, while employing advanced techniques such as time-resolved photoluminescence (TRPL), electrochemical impedance spectroscopy (EIS), and radical trapping to clarify charge transfer pathways and dominant reactive species. Secondly, industrial applications will require transitioning from batch to continuous flow systems and immobilizing the powdered composite onto fixed beds or membranes to ease separation and handling and the composite's versatility should also be tested against other persistent pollutants like pharmaceuticals, PFAS, pesticides, and other organic chemicals. Thirdly further optimization of metal doping concentration and component mass ratios could enhance efficiency and lower the band gap, while life cycle assessment and cost-benefit analysis are needed to evaluate economic feasibility and environmental footprint at larger scales. To summarize, the [Fe/g-C_3N_4]/ZnO/AC ternary composite can be a highly promising clay-supported heterojunction photocatalyst for solar-driven azo dye degradation, and with continued research, it holds significant potential for real-world wastewater treatment.

Appendices

4.3 SEM images of sample

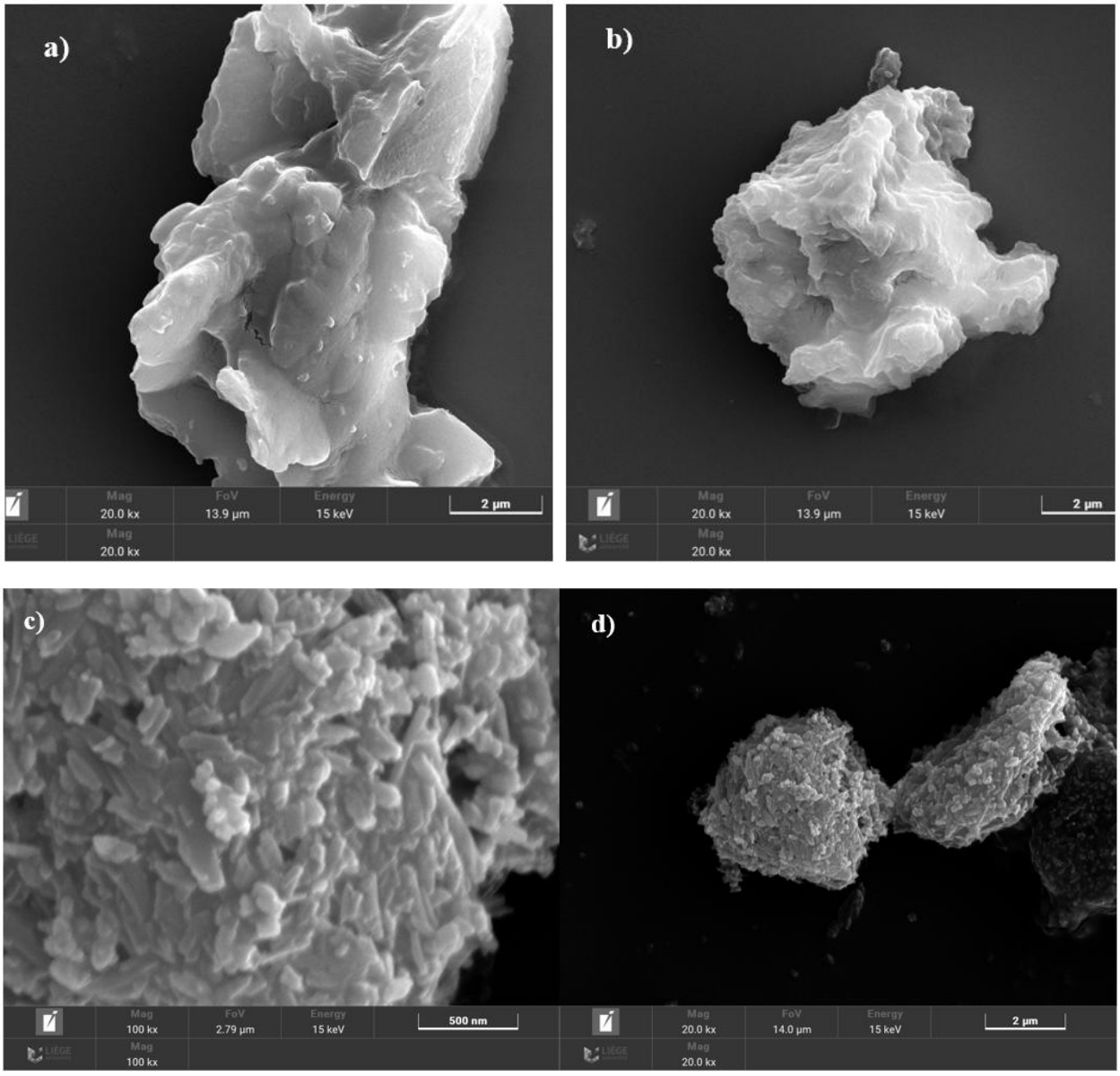

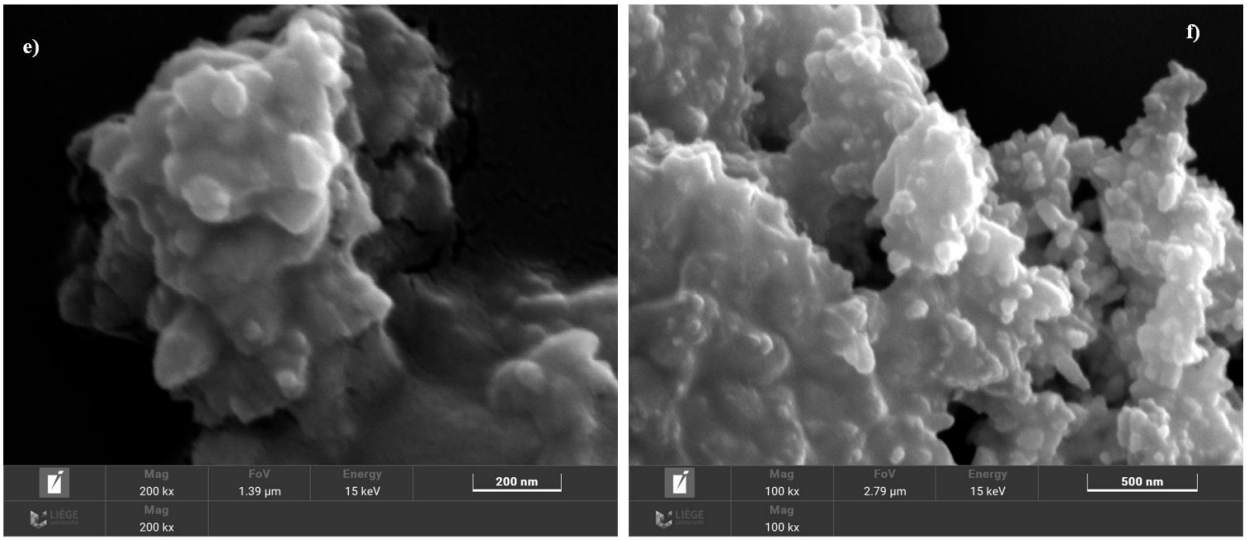

Figure 4.1: SEM images of a) g-C_3N_4 b) Fe/g-C_3N_4 c, d) ZnO/AC, e) [Fe/g-C_3N_4]/ZnO and f) [Fe/g-C_3N_4]/ZnO/AC

4.4 Optical properties

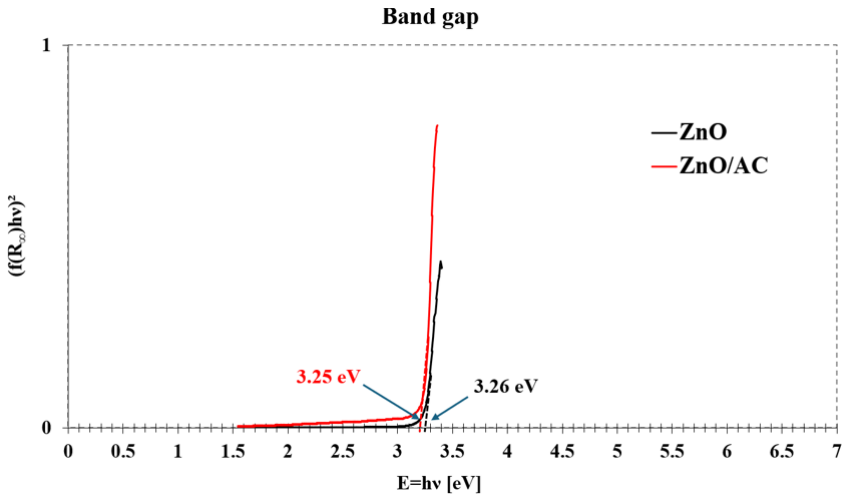

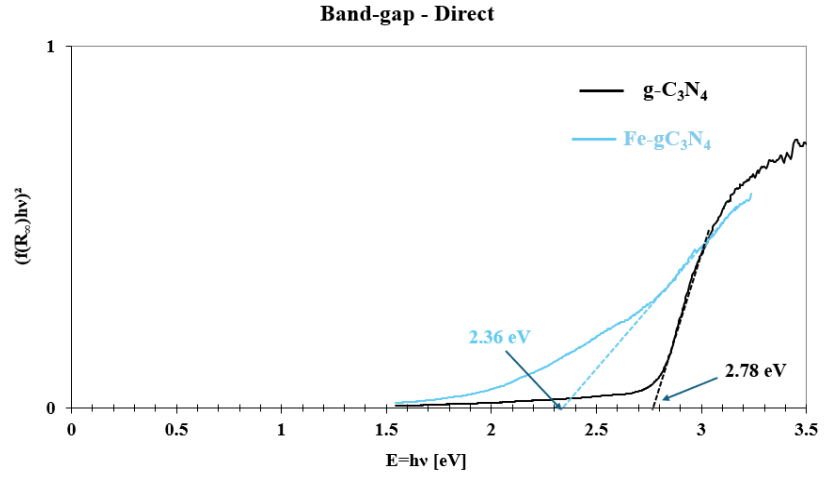

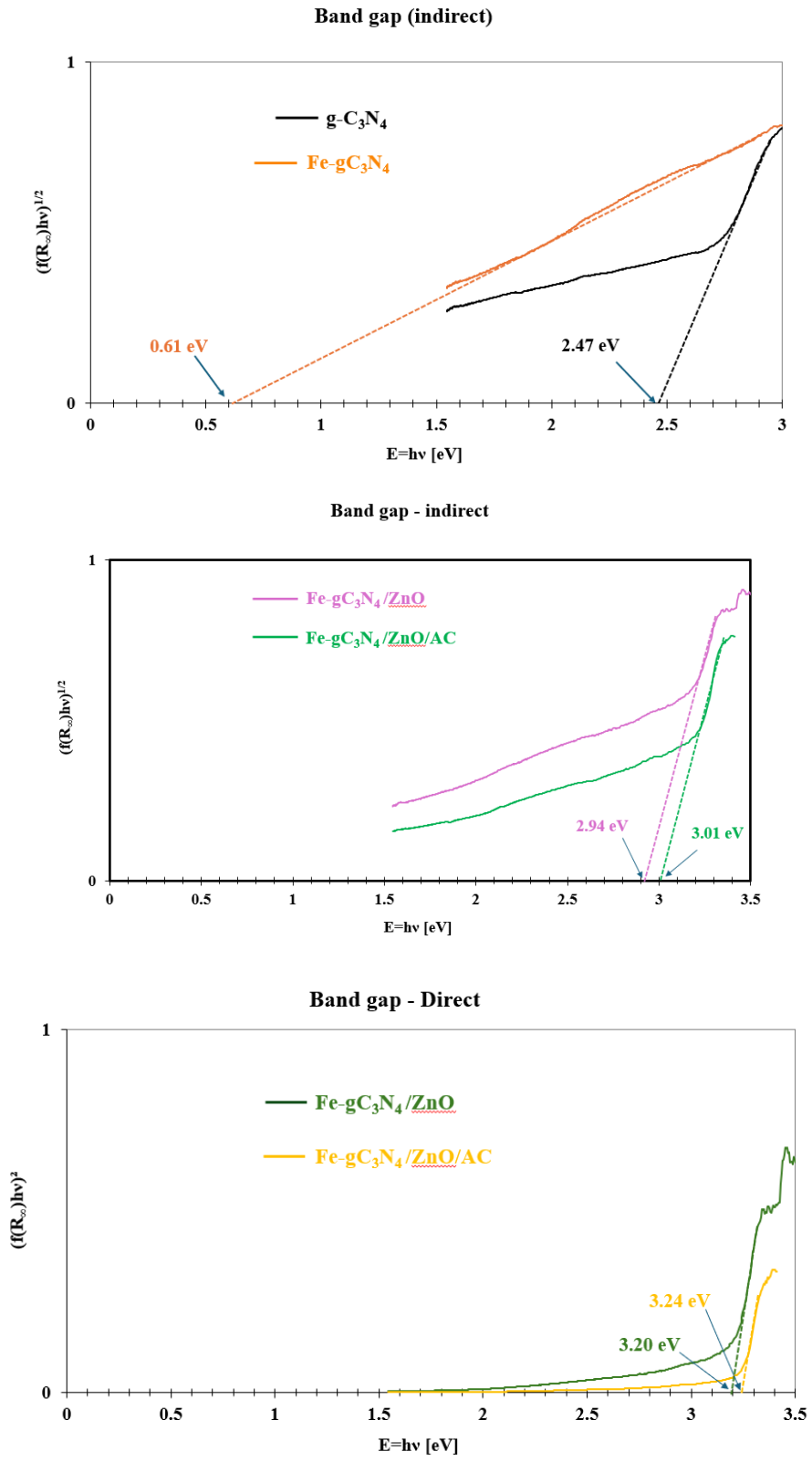

Figure 4.2: Direct and indirect Band gap of ZnO and ZnO/AC, g-C_3N_4 and Fe/g-C_3N_4, [Fe/g-C_3N_4]/ZnO and [Fe/g-C_3N_4]/ZnO/AC

4.5 Photocatalytic test

RB 5		Dark				Dark				visible light radiation			
Sample		0 h	C	C/C0	%D/%AD	30min	C	C/C0	%AD	2h	C	C/C0	%D
AC		0.617	20	1	0	0.59	19.032	0.952	4.84				
gCN		0.617	20	1	0	0.6	19.355	0.968	3.23	0.329	10.61	0.531	46.94
FegCN		0.617	20	1	0	0.55	17.742	0.887	11.29	0.456	14.71	0.735	26.45
FegCN/AC		0.617	20	1	0	0.595	19.194	0.960	4.03	0.481	15.52	0.776	22.42
ZnO		0.617	20	1	0	0.525	16.935	0.847	15.32	0.322	10.39	0.519	48.06
ZnO/AC		0.617	20	1	0	0.511	16.484	0.824	17.58	0.385	12.42	0.621	37.90
FegCN/ZnO		0.617	20	1	0	0.482	15.548	0.777	22.26	0.198	6.39	0.319	68.06
FegCN/ZnO/AC		0.617	20	1	0	0.505	16.290	0.815	18.55	0.187	6.03	0.302	69.84

RB 5		visible light radiation				visible light radiation				visible light radiation			
Sample		4h	C	C/C0	%D	6h	C	C/C0	%D	8h	C	C/C0	%D
AC													
gCN		0.258	8.32	0.416	58.39	0.198	6.39	0.319	68.06	0.111	3.581	0.179	82.10
FegCN		0.305	9.84	0.492	50.81	0.217	7.00	0.350	65.00	0.123	3.968	0.198	80.16
FegCN/AC		0.401	12.94	0.647	35.32	0.32	10.32	0.516	48.39	0.261	8.419	0.421	57.90
ZnO		0.236	7.61	0.381	61.94	0.185	5.97	0.298	70.16	0.102	3.290	0.165	83.55
ZnO/AC		0.194	6.26	0.313	68.71	0.043	1.39	0.069	93.06	0.007	0.226	0.011	98.87
FegCN/ZnO		0.1	3.23	0.161	83.87	0.028	0.90	0.045	95.48	0.002	0.065	0.003	99.68
FegCN/ZnO/AC		0.095	3.06	0.153	84.68	0.01	0.32	0.016	98.39	0.001	0.032	0.002	99.84

g-CN			Fe-gCN			Fe-gCN/AC			ZnO		
	Time (t)	C/Co		Time (t)	C/Co		Time (t)	C/Co		Time (t)	C/Co
	0	1		0	1		0	1		0	1
	0.5	0.968		0.5	0.887		0.5	0.96		0.5	0.847
	2.5	0.531		2.5	0.735		2.5	0.776		2.5	0.519
	4.5	0.416		4.5	0.492		4.5	0.647		4.5	0.381
	6.5	0.319		6.5	0.35		6.5	0.516		6.5	0.298
	8.5	0.179		8.5	0.198		8.5	0.421		8.5	0.165

Sample	Time	% remova		Time (t)	%removal		Time (t)	%removal		Time (t)	%removal
gCN	0	0		0	0		0	0		0	0
	0.5	3.23		0.5	11.29		0.5	4.03		0.5	15.32
	2.5	46.94	Fe-gCN	2.5	26.45	Fe-gCN/AC	2.5	22.42	ZnO	2.5	48.06
	4.5	58.39		4.5	50.81		4.5	35.32		4.5	61.94
	6.5	68.06		6.5	65		6.5	48.39		6.5	70.16
	8.5	82.1		8.5	80.16		8.5	57.9		8.5	83.55

										New ternary	
Time (t)	C/Co		Time (t)	C/Co		Time (t)	C/Co		Time (t)	C/Co	time	C/Co
0	1		0	1		0	1		0	1	0	1
0.5	0.847	ZnO/AC	0.5	0.824	Fe-gCN/ZnO	0.5	0.777	Fe-gCN/ZnO/AC	0.5	0.815	0.5	0.815
2.5	0.519		2.5	0.621		2.5	0.35		2.5	0.302	1	0.679
4.5	0.381		4.5	0.313		4.5	0.211		4.5	0.153	1.5	0.551
6.5	0.298		6.5	0.069		6.5	0.045		6.5	0.016	2	0.422
8.5	0.165		8.5	0.025		8.5	0.003		8.5	0.002	2.5	0.302
											4.5	0.153
											6.5	0.016
Time (t)	%removal		Time (t)	% remova		Time (t)	% remova		Time (t)	% removal	8.5	0.002
0	0		0	0		0	0		0	0		
0.5	15.32	ZnO/AC	0.5	17.58	Fe-gCN/ZnO	0.5	22.26	Fe-gCN/ZnO/AC	0.5	18.55		
2.5	48.06		2.5	37.9		2.5	68.06		2.5	69.84		
4.5	61.94		4.5	68.71		4.5	83.87		4.5	84.68		
6.5	70.16		6.5	93.06		6.5	95.48		6.5	98.39		
8.5	83.55		8.5	98.87		8.5	99.68		8.5	99.84		

	Time (hr)	initial con.	Abs	Final con.	C/Co	% AD/D%	ln (C/Co)	2nd C/Co	ln C/Co
ternary composite Kinetics	0	20	0.617	20	1	0	0.000	1.000	0.000
	0.5	20	0.505	16.29	0.815	18.55	0.205	0.810	0.211
	1	20	0.42	13.58	0.679	32.10	0.387	0.670	0.400
	1.5	20	0.341	11.02	0.551	44.90	0.596	0.545	0.607
	2	20	0.261	8.44	0.422	57.80	0.863	0.416	0.877
	2.5	20	0.187	6.03	0.302	69.85	1.199	0.296	1.217
	4.5	20	0.095	3.06	0.153	84.70	1.877	0.147	1.917
	6.5	20	0.01	0.32	0.016	98.40	4.135	0.014	4.269
	8.5	20	0.001	0.032	0.002	99.84	6.438	0.002	6.215

Figure 4.3: Absorbance, residual concentration, degradation (%) and Kinetics data of sample

Bibliography

[1] S. Benkhaya, S. M'rabet, and A. El Harfi, "Classifications, properties, recent synthesis and applications of azo dyes," *Heliyon*, vol. 6, no. 1, p. e03271, Jan. 2020, doi: 10.1016/j.heliyon.2020.e03271.

[2] P. K. Singh and R. L. Singh, "Bio-removal of Azo Dyes: A Review," *Int J Appl Sci Biotechnol*, vol. 5, no. 2, pp. 108–126, Jun. 2017, doi: 10.3126/ijasbt.v5i2.16881.

[3] P. Barciela, A. Perez-Vazquez, and M. A. Prieto, "Azo dyes in the food industry: Features, classification, toxicity, alternatives, and regulation," *Food and Chemical Toxicology*, vol. 178, p. 113935, Aug. 2023, doi: 10.1016/j.fct.2023.113935.

[4] L. Emanuele and M. D'Auria, "The Use of Heterocyclic Azo Dyes on Different Textile Materials: A Review," *Organics*, vol. 5, no. 3, pp. 277–289, Aug. 2024, doi: 10.3390/org5030015.

[5] A. Strebel, M. Behringer, H. Hilbig, A. Machner, and B. Helmreich, "Anionic azo dyes and their removal from textile wastewater through adsorption by various adsorbents: a critical review," *Front. Environ. Eng.*, vol. 3, p. 1347981, Jan. 2024, doi: 10.3389/fenve.2024.1347981.

[6] S. Singh, P. Singh, A. Saifi, S. G. Pratap, and P. K. Singh, "Plant-based Enzyme-mediated Biodegradation of Azo dyes: A Review," *IJPE*, vol. 7, no. 03, pp. 187–201, Nov. 2021, doi: 10.18811/ijpen.v7i03.2.

[7] R. Krishnamoorthy *et al.*, "Long-Term Exposure to Azo Dyes from Textile Wastewater Causes the Abundance of Saccharibacteria Population," *Applied Sciences*, vol. 11, no. 1, p. 379, Jan. 2021, doi: 10.3390/app11010379.

[8] F. M. Drumond Chequer, D. Junqueira, and D. P. De Oliveir, "Azo Dyes and Their Metabolites: Does the Discharge of the Azo Dye into Water Bodies Represent Human and Ecological Risks?," in *Advances in Treating Textile Effluent*, P. Hauser, Ed., InTech, 2011. doi: 10.5772/19872.

[9]"https://vinosupraja.com/blogs/news/sustainable-fashion-alert-how-azo-dyes-are-polluting-our-water?srsltid=AfmBOop5HIWwvA5YYhvwec4f-QRqdst3xzpL9w6x9MDk3Lg7Yc_2tfeB."

[10] S. Dutta, B. Gupta, S. K. Srivastava, and A. K. Gupta, "Recent advances on the removal of dyes from wastewater using various adsorbents: a critical review," *Mater. Adv.*, vol. 2, no. 14, pp. 4497–4531, 2021, doi: 10.1039/D1MA00354B.

[11] R. D. Saini, "Textile Organic Dyes: Polluting effects and Elimination Methods from Textile Wastewater".

[12] I. K. Konstantinou and T. A. Albanis, “TiO2-assisted photocatalytic degradation of azo dyes in aqueous solution: kinetic and mechanistic investigations,” *Applied Catalysis B: Environmental*, vol. 49, no. 1, pp. 1–14, Apr. 2004, doi: 10.1016/j.apcatb.2003.11.010.

[13] K.-T. Chung and C. E. Cerniglia, “Mutagenicity of azo dyes: Structure-activity relationships,” *Mutation Research/Reviews in Genetic Toxicology*, vol. 277, no. 3, pp. 201–220, Sep. 1992, doi: 10.1016/0165-1110(92)90044-A.

[14] A. E. Ali *et al.*, “Removal of Azo Dyes from Aqueous Effluent Using Bio-Based Activated Carbons: Toxicity Aspects and Environmental Impact,” *Separations*, vol. 10, no. 9, p. 506, Sep. 2023, doi: 10.3390/separations10090506.

[15] V. Vaiano and I. De Marco, “Removal of Azo Dyes from Wastewater through Heterogeneous Photocatalysis and Supercritical Water Oxidation,” *Separations*, vol. 10, no. 4, p. 230, Mar. 2023, doi: 10.3390/separations10040230.

[16] S. Nethaji, A. Sivasamy, and A. B. Mandal, “Adsorption isotherms, kinetics and mechanism for the adsorption of cationic and anionic dyes onto carbonaceous particles prepared from Juglans regia shell biomass,” *Int. J. Environ. Sci. Technol.*, vol. 10, no. 2, pp. 231–242, Mar. 2013, doi: 10.1007/s13762-012-0112-0.

[17] Sharma, A.; Rani, S.; Bansal, A.; Sood, A. Effect of mordant combination on silk dyeing with apricot dye. In Natural Dyes: Scope Challenges; Daniel, M., Bhattacharya, S.D., Arya, A., Raole, V.M., Eds.; Scientific Publishers (India): Jodhpur, India, 2006; pp. 137–143.

[18] Y.-Y. Lau, Y.-S. Wong, T.-T. Teng, N. Morad, M. Rafatullah, and S.-A. Ong, “Coagulation-flocculation of azo dye Acid Orange 7 with green refined laterite soil,” *Chemical Engineering Journal*, vol. 246, pp. 383–390, Jun. 2014, doi: 10.1016/j.cej.2014.02.100.

[19] Y. Mittal, S. Dash, P. Srivastava, P. M. Mishra, T. M. Aminabhavi, and A. K. Yadav, “Azo dye containing wastewater treatment in earthen membrane based unplanted two chambered constructed wetlands-microbial fuel cells: A new design for enhanced performance,” *Chemical Engineering Journal*, vol. 427, p. 131856, Jan. 2022, doi: 10.1016/j.cej.2021.131856.

[20] M. Solís, A. Solís, H. I. Pérez, N. Manjarrez, and M. Flores, “Microbial decolouration of azo dyes: A review,” *Process Biochemistry*, vol. 47, no. 12, pp. 1723–1748, Dec. 2012, doi: 10.1016/j.procbio.2012.08.014.

[21] L. G. Devi and M. L. ArunaKumari, “Enhanced photocatalytic performance of Hemin (chloro (protoporhyinato)iron(III)) anchored TiO2 photocatalyst for methyl orange degradation: A surface modification method,” *Applied Surface Science*, vol. 276, pp. 521–528, Jul. 2013, doi: 10.1016/j.apsusc.2013.03.127.

[22] J. Zhang, S. Wang, Y. Guo, D. Xu, Y. Gong, and X. Tang, “Experimental study on supercritical water oxidation of CI Reactive Orange 7 dye wastewater using response surface methodology,” *Coloration Technology*, vol. 128, no. 4, pp. 323–330, Aug. 2012, doi: 10.1111/j.1478-4408.2012. 00384.x.

[23] R. Al-Tohamy *et al.*, "A critical review on the treatment of dye-containing wastewater: Ecotoxicological and health concerns of textile dyes and possible remediation approaches for environmental safety," *Ecotoxicology and Environmental Safety*, vol. 231, p. 113160, Feb. 2022, doi: 10.1016/j.ecoenv.2021.113160.

[24] Z. Tong, P. Zheng, B. Bai, H. Wang, and Y. Suo, "Adsorption Performance of Methyl Violet via α-Fe2O3@Porous Hollow Carbonaceous Microspheres and Its Effective Regeneration through a Fenton-Like Reaction," *Catalysts*, vol. 6, no. 4, p. 58, Apr. 2016, doi: 10.3390/catal6040058.

[25] L. Wang, J. Zhang, R. Zhao, C. Li, Y. Li, and C. Zhang, "Adsorption of basic dyes on activated carbon prepared from Polygonum orientale Linn: Equilibrium, kinetic and thermodynamic studies," *Desalination*, vol. 254, no. 1–3, pp. 68–74, May 2010, doi: 10.1016/j.desal.2009.12.012.

[26] S. Sharma, R. Saxena, and G. Gaur, "Study of Removal Techniques for Azo Dyes by Biosorption: A Review," *IOSRJAC*, vol. 7, no. 10, pp. 06–21, 2014, doi: 10.9790/5736-071010621.

[27] A. E. Al Prol, "Study of Environmental Concerns of Dyes and Recent Textile Effluents Treatment Technology: A Review," *AJFAR*, pp. 1–18, Jun. 2019, doi: 10.9734/ajfar/2019/v3i230032.

[28] "Chen, Y., Tsao, T.M., & Wang, M. (2011). Removal of Crystal Violet and Methylene Blue from Aqueous Solution using Soil Nano-Clays".

[29] A. Gurses, C. Dogar, M. Yalcin, M. Acikyildiz, R. Bayrak, and S. Karaca, "The adsorption kinetics of the cationic dye, methylene blue, onto clay," *Journal of Hazardous Materials*, vol. 131, no. 1–3, pp. 217–228, Apr. 2006, doi: 10.1016/j.jhazmat.2005.09.036.

[30] M. Guin, N. Singh, and A. De, "Clay and clay minerals: A brief review from fundamentals to applications," *Zas Mat*, vol. 66, no. 4, pp. 737–763, Dec. 2025, doi: 10.62638/ZasMat1138.

[31] Bergaya, F., Theng, B. K. G., & Lagaly, G. (Eds.). (2006). Handbook of clay science, Developments in Clay Science, Vol. 1, Elsevier.

[32] A. A. Adeyemo, I. O. Adeoye, and O. S. Bello, "Adsorption of dyes using different types of clay: a review," *Appl Water Sci*, vol. 7, no. 2, pp. 543–568, May 2017, doi: 10.1007/s13201-015-0322-y.

[33] G. D. Yuan, B. K. G. Theng, G. J. Churchman, and W. P. Gates, "Clays and Clay Minerals for Pollution Control," in *Developments in Clay Science*, vol. 5, Elsevier, 2013, pp. 587–644. doi: 10.1016/B978-0-08-098259-5.00021-4.

[34] Y. M. Vargas-Rodríguez *et al.*, "Adsorption Studies of Aqueous Solutions of Methyl Green for Halloysite Nanotubes: Kinetics, Isotherms, and Thermodynamic Parameters," *AJN*, vol. 9, no. 1, pp. 1–11, Mar. 2021, doi: 10.12691/ajn-9-1-1.

[35] I. Ali, Mohd. Asim, and T. A. Khan, "Low cost adsorbents for the removal of organic pollutants from wastewater," *Journal of Environmental Management*, vol. 113, pp. 170–183, Dec. 2012, doi: 10.1016/j.jenvman.2012.08.028.

[36] A. S. Özcan, B. Erdem, and A. Özcan, "Adsorption of Acid Blue 193 from aqueous solutions onto Na–bentonite and DTMA–bentonite," *Journal of Colloid and Interface Science*, vol. 280, no. 1, pp. 44–54, Dec. 2004, doi: 10.1016/j.jcis.2004.07.035.

[37] A. Awasthi, P. Jadhao, and K. Kumari, "Clay nano-adsorbent: structures, applications and mechanism for water treatment," *SN Appl. Sci.*, vol. 1, no. 9, p. 1076, Sep. 2019, doi: 10.1007/s42452-019-0858-9.

[38] E. Durgut, M. Cinar, M. Terzi, I. Kursun Unver, Y. Yildirim, and O. Ozdemir, "Evaluation of Different Dispersants on the Dispersion/Sedimentation Behavior of Halloysite, Kaolinite, and Quartz Suspensions in the Enrichment of Halloysite Ore by Mechanical Dispersion," *Minerals*, vol. 12, no. 11, p. 1426, Nov. 2022, doi: 10.3390/min12111426.

[39] *Lázaro, Blanca Bauluz. "Halloysite and kaolinite: two clay minerals with geological and technological importance." (2015).*

[40] *Churchman, G. Properties and Processes, Handbook of Soil Sciences, 2nd ed.; Sumner, M.E., Ed.; CRC Press: Boca Raton, FL, USA, 1999; pp. F3–F76, 2nd Chapter*.

[41] M. T. A. Aydın, "A spectroscopic study on the effect of acid concentration on the physicochemical properties of calcined halloysite nanotubes," *J Aust Ceram Soc*, vol. 60, no. 2, pp. 629–642, Apr. 2024, doi: 10.1007/s41779-024-01003-z.

[42] F. N. Türk, M. Ş. A. Eren, and H. Arslanoğlu, "Adsorption of Reactive Black 5 dye from aqueous solutions with a clay halloysite having a nanotubular structure: Interpretation of mechanism, kinetics, isotherm and thermodynamic parameters," *Inorganic Chemistry Communications*, vol. 171, p. 113600, Jan. 2025, doi: 10.1016/j.inoche.2024.113600.

[43] PubChem [Internet]. Bethesda (MD): National Library of Medicine (US), National Center for Biotechnology Information; 2004-. PubChem Compound Summary for CID 135442967, C.I. Reactive Black 5; [cited 2026 June 4]. Available from: https://pubchem.ncbi.nlm.nih.gov/compound/C.I.-Reactive-Black-5

[44] Y. Deng and R. Zhao, "Advanced Oxidation Processes (AOPs) in Wastewater Treatment," *Curr Pollution Rep*, vol. 1, no. 3, pp. 167–176, Sep. 2015, doi: 10.1007/s40726-015-0015-z.

[45] S. Satyam and S. Patra, "The Evolving Landscape of Advanced Oxidation Processes in Wastewater Treatment: Challenges and Recent Innovations," *Processes*, vol. 13, no. 4, p. 987, Mar. 2025, doi: 10.3390/pr13040987.

[46] J. Mukherjee *et al.*, "Advanced oxidation process for the treatment of industrial wastewater: A review on strategies, mechanisms, bottlenecks and prospects," *Chemosphere*, vol. 345, p. 140473, Dec. 2023, doi: 10.1016/j.chemosphere.2023.140473.

[47] C. Chuaicham *et al.*, "Recent Clay-Based Photocatalysts for Wastewater Treatment," *Separations*, vol. 10, no. 2, p. 77, Jan. 2023, doi: 10.3390/separations10020077.

[48] A. Ibhadon and P. Fitzpatrick, "Heterogeneous Photocatalysis: Recent Advances and Applications," *Catalysts*, vol. 3, no. 1, pp. 189–218, Mar. 2013, doi: 10.3390/catal3010189.

[49] S. Raha and Md. Ahmaruzzaman, “ZnO nanostructured materials and their potential applications: progress, challenges and perspectives,” *Nanoscale Adv.*, vol. 4, no. 8, pp. 1868–1925, 2022, doi: 10.1039/D1NA00880C.

[50] A. Kołodziejczak-Radzimska and T. Jesionowski, “Zinc Oxide—From Synthesis to Application: A Review,” *Materials*, vol. 7, no. 4, pp. 2833–2881, Apr. 2014, doi: 10.3390/ma7042833.

[51] X.-Q. Zhou *et al.*, “Zinc Oxide Nanoparticles: Synthesis, Characterization, Modification, and Applications in Food and Agriculture,” *Processes*, vol. 11, no. 4, p. 1193, Apr. 2023, doi: 10.3390/pr11041193.

[52] R. Ghamarpoor, A. Fallah, and M. Jamshidi, “A Review of Synthesis Methods, Modifications, and Mechanisms of ZnO/TiO_2 -Based Photocatalysts for Photodegradation of Contaminants,” *ACS Omega*, vol. 9, no. 24, pp. 25457–25492, Jun. 2024, doi: 10.1021/acsomega.3c08717.

[53] S. Kundu, S. Haydar, and P. Mandal, “Zinc Oxide Nanoparticles: Different synthesis approaches and applications,” *NBUJPS*, vol. 13, no. 1, pp. 42–64, 2021, doi: 10.55734/NBUJPS.2021.v13i01.005.

[54] A. Baig, M. Siddique, and S. Panchal, “A Review of Visible-Light-Active Zinc Oxide Photocatalysts for Environmental Application,” *Catalysts*, vol. 15, no. 2, p. 100, Jan. 2025, doi: 10.3390/catal15020100.

[55] Y. Sun, W. Zhang, Q. Li, H. Liu, and X. Wang, “Preparations and applications of zinc oxide based photocatalytic materials,” *Advanced Sensor and Energy Materials*, vol. 2, no. 3, p. 100069, Sep. 2023, doi: 10.1016/j.asems.2023.100069.

[56] M. Ramalingam, V. K. Ponnusamy, and S. N. Sangilimuthu, “Electrochemical determination of 4-nitrophenol in environmental water samples using porous graphitic carbon nitride-coated screen-printed electrode,” *Environ Sci Pollut Res*, vol. 27, no. 15, pp. 17481–17491, May 2020, doi: 10.1007/s11356-019-05494-3.

[57] G. Mamba and A. K. Mishra, “Graphitic carbon nitride (g-C3N4) nanocomposites: A new and exciting generation of visible light driven photocatalysts for environmental pollution remediation,” *Applied Catalysis B: Environmental*, vol. 198, pp. 347–377, Dec. 2016, doi: 10.1016/j.apcatb.2016.05.052.

[58] Z. Lu, W. Song, and M. Liu, “Enhanced Visible-Light-Driven Photocatalytic Activity by Fe(Ⅲ)-Doped Graphitic C3N4,” *Molecules*, vol. 27, no. 20, p. 6986, Oct. 2022, doi: 10.3390/molecules27206986.

[59] J.-C. Wang, C.-X. Cui, Y. Li, L. Liu, Y.-P. Zhang, and W. Shi, “Porous Mn doped g-C3N4 photocatalysts for enhanced synergetic degradation under visible-light illumination,” *Journal of Hazardous Materials*, vol. 339, pp. 43–53, Oct. 2017, doi: 10.1016/j.jhazmat.2017.06.011.

[60] J. Xu, K.-Z. Long, Y. Wang, B. Xue, and Y.-X. Li, “Fast and facile preparation of metal-doped g-C3N4 composites for catalytic synthesis of dimethyl carbonate,” *Applied Catalysis A: General*, vol. 496, pp. 1–8, Apr. 2015, doi: 10.1016/j.apcata.2015.02.025.

[61] K. Akhtar, S. A. Khan, S. B. Khan, and A. M. Asiri, "Scanning Electron Microscopy: Principle and Applications in Nanomaterials Characterization," in *Handbook of Materials Characterization*, S. K. Sharma, Ed., Cham: Springer International Publishing, 2018, pp. 113–145. doi: 10.1007/978-3-319-92955-2_4.

[62] A. Ali, Y. W. Chiang, and R. M. Santos, "X-ray Diffraction Techniques for Mineral Characterization: A Review for Engineers of the Fundamentals, Applications, and Research Directions," *Minerals*, vol. 12, no. 2, p. 205, Feb. 2022, doi: 10.3390/min12020205.

[63] "https://myscope.training/XRD_Anatomy_of_an_X_ray_diffractometer___Intro."

[64] M. Thommes *et al.*, "Physisorption of gases, with special reference to the evaluation of surface area and pore size distribution (IUPAC Technical Report)," *Pure and Applied Chemistry*, vol. 87, no. 9–10, pp. 1051–1069, Oct. 2015, doi: 10.1515/pac-2014-1117.

[65] A. Serrano-Lotina, R. Portela, P. Baeza, V. Alcolea-Rodriguez, M. Villarroel, and P. Ávila, "Zeta potential as a tool for functional materials development," *Catalysis Today*, vol. 423, p. 113862, Nov. 2023, doi: 10.1016/j.cattod.2022.08.004.

[66] G. Greczynski and L. Hultman, "X-ray photoelectron spectroscopy: Towards reliable binding energy referencing," *Progress in Materials Science*, vol. 107, p. 100591, Jan. 2020, doi: 10.1016/j.pmatsci.2019.100591.

[67] J. Torrent and V. Barrón, "Diffuse Reflectance Spectroscopy," in *SSSA Book Series*, 1st ed., vol. 5, A. L. Ulery and L. Richard Drees, Eds., Wiley, 2008, pp. 367–385. doi: 10.2136/sssabookser5.5.c13.

[68] J. G. Mahy *et al.*, "Towards a large scale aqueous sol-gel synthesis of doped TiO2: Study of various metallic dopings for the photocatalytic degradation of p-nitrophenol," *Journal of Photochemistry and Photobiology A: Chemistry*, vol. 329, pp. 189–202, Oct. 2016, doi: 10.1016/j.jphotochem.2016.06.029.

[69] M. A. Abdel-Fadeel, N. S. Aljohani, S. R. Al-Mhyawi, R. F. Halawani, E. H. Aljuhani, and M. A. Salam, "A simple method for removal of toxic dyes such as Brilliant Green and Acid Red from the aquatic environment using Halloysite nanoclay," *Journal of Saudi Chemical Society*, vol. 26, no. 3, p. 101475, May 2022, doi: 10.1016/j.jscs.2022.101475.

[70] A.-B. Zhang *et al.*, "Effects of acid treatment on the physico-chemical and pore characteristics of halloysite," *Colloids and Surfaces A: Physicochemical and Engineering Aspects*, vol. 396, pp. 182–188, Feb. 2012, doi: 10.1016/j.colsurfa.2011.12.067.

[71] A. Mahajan and P. Gupta, "Halloysite nanotubes based heterogeneous solid acid catalysts," *New J. Chem.*, vol. 44, no. 30, pp. 12897–12908, 2020, doi: 10.1039/D0NJ02846K.

[72] I. Surya, A. Masa, H. Ismail, and N. Hayeemasae, "Acid-treated halloysite nanotubes filled natural rubber composites," *IOP Conf. Ser.: Mater. Sci. Eng.*, vol. 801, no. 1, p. 012087, May 2020, doi: 10.1088/1757-899X/801/1/012087.

[73] M. Alshabanat *et al.*, "Preparation and characterization of zno/bentonite nanocomposites for enhanced photocatalytic degradation of pesticides in contaminated water," *Sci Rep*, vol. 15, no. 1, p. 23816, Jul. 2025, doi: 10.1038/s41598-025-09449-2.

[74] H. Shaikh *et al.*, "Facile and Low-Cost Fabrication of ZnO/Kaolinite Composites by Modifying the Kaolinite Composition for Efficient Degradation of Methylene Blue Under Sunlight Illumination," *Catalysts*, vol. 15, no. 6, p. 566, Jun. 2025, doi: 10.3390/catal15060566.

[75] M. M, N. Raghavendra, N. R. Bhumika, C. H. Chaithra, B. N. Nagalaxmi, and K. N. Shravana Kumara, "Study of ZnO nanoparticle-supported clay minerals for electrochemical sensors, photocatalysis, and antioxidant applications," *ChemPhysMater*, vol. 3, no. 1, pp. 83–93, Jan. 2024, doi: 10.1016/j.chphma.2023.07.002

[76] P. Ngue Song *et al.*, "Synergistic visible-light photocatalysis by ZnO/black phosphorus nanohybrids immobilized on activated kaolinite," *Next Materials*, vol. 10, p. 101390, Jan. 2026, doi: 10.1016/j.nxmate.2025.101390

[77] P. Ngue Song, J. G. Mahy, A. Farcy, C. Calberg, N. Fagel, and S. D. Lambert, "Development of novel composite materials based on kaolinitic clay modified with ZnO for the elimination of azo dyes by adsorption in water," *Results in Surfaces and Interfaces*, vol. 16, p. 100255, Aug. 2024, doi: 10.1016/j.rsurfi.2024.100255.

[78] B. Sert, Z. Bilici, K. Ocakoglu, N. Dizge, T. S. Rad, and A. Khataee, "Preparation of S-Scheme g-C3N4/ZnO Heterojunction Composite for Highly Efficient Photocatalytic Destruction of Refractory Organic Pollutant," *Catalysts*, vol. 13, no. 3, p. 485, Feb. 2023, doi: 10.3390/catal13030485.

[79] P. Kalisamy *et al.*, "ZnO coupled F-doped g-C3N4: Z-scheme heterojunction for visible-light driven photocatalytic degradation reaction," *Inorganic Chemistry Communications*, vol. 135, p. 109102, Jan. 2022, doi: 10.1016/j.inoche.2021.109102.

[80] D. R. Paul, S. Gautam, P. Panchal, S. P. Nehra, P. Choudhary, and A. Sharma, "ZnO-Modified g-C_3 N_4: A Potential Photocatalyst for Environmental Application," *ACS Omega*, vol. 5, no. 8, pp. 3828–3838, Mar. 2020, doi: 10.1021/acsomega.9b02688.

[81] W. Liu, M. Wang, C. Xu, and S. Chen, "Facile synthesis of g-C3N4/ZnO composite with enhanced visible light photooxidation and photoreduction properties," *Chemical Engineering Journal*, vol. 209, pp. 386–393, Oct. 2012, doi: 10.1016/j.cej.2012.08.033.

[82] S. Ziaalmolki, B. Aslibeiki, M. Zarei, R. Torkamani, and T. Sarkar, "Enhanced visible-light-driven photocatalysis via magnetic nanocomposites: A comparative study of g-C3N4, g-C3N4/Fe3O4, and g-C3N4/Fe3O4/ZnO," *Materials Today Communications*, vol. 37, p. 107340, Dec. 2023, doi: 10.1016/j.mtcomm.2023.107340.

[83] M. Malik *et al.*, "Engineering of a Hybrid g-C3N4/ZnO-W/Cox Heterojunction Photocatalyst for the Removal of Methylene Blue Dye," *Catalysts*, vol. 13, no. 5, p. 813, Apr. 2023, doi: 10.3390/catal13050813.

[84] Z. Wu, X. Chen, X. Liu, X. Yang, and Y. Yang, "A Ternary Magnetic Recyclable ZnO/Fe3O4/g-C3N4 Composite Photocatalyst for Efficient Photodegradation of Monoazo Dye," *Nanoscale Res Lett*, vol. 14, no. 1, p. 147, Dec. 2019, doi: 10.1186/s11671-019-2974-2.

[85] Bordeepong, S.; Bhongsuwan, D.; Pungrassami, T.; Bhongsuwan, T. "Characterization of Halloysite from Thung Yai District, Nakhon Si Thammarat Province, Southern Thailand. Songklanakarin J. Sci. Technol." 2011, 33, 599–607.

[86] S. Sh. Zargarian, V. Haddadi-Asl, and H. Hematpour, “Carboxylic acid functionalization of halloysite nanotubes for sustained release of diphenhydramine hydrochloride,” *J Nanopart Res*, vol. 17, no. 5, p. 218, May 2015, doi: 10.1007/s11051-015-3032-3.

[87] S. R. Levis and P. B. Deasy, “Characterisation of halloysite for use as a microtubular drug delivery system,” *International Journal of Pharmaceutics*, vol. 243, no. 1–2, pp. 125–134, Aug. 2002, doi: 10.1016/S0378-5173(02)00274-0.

[88] J. Jin, Y. Zhang, J. Ouyang, and H. Yang, “Halloysite nanotubes as hydrogen storage materials,” *Phys Chem Minerals*, vol. 41, no. 5, pp. 323–331, May 2014, doi: 10.1007/s00269-013-0651-z.

[89] P. Yuan *et al.*, “Changes in Structure, Morphology, Porosity, and Surface Activity of Mesoporous Halloysite Nanotubes Under Heating,” *Clays and clay miner.*, vol. 60, no. 6, pp. 561–573, Dec. 2012, doi: 10.1346/CCMN.2012.0600602.

[90] K. Belkassa, F. Bessaha, K. Marouf-Khelifa, I. Batonneau-Gener, J. Comparot, and A. Khelifa, “Physicochemical and adsorptive properties of a heat-treated and acid-leached Algerian halloysite,” *Colloids and Surfaces A: Physicochemical and Engineering Aspects*, vol. 421, pp. 26–33, Mar. 2013, doi: 10.1016/j.colsurfa.2012.12.048.

[91] L. Deng *et al.*, “Effects of calcination and acid treatment on improving benzene adsorption performance of halloysite,” *Applied Clay Science*, vol. 181, p. 105240, Nov. 2019, doi: 10.1016/j.clay.2019.105240.

[92] S. Kadi, S. Lellou, K. Marouf-Khelifa, J. Schott, I. Gener-Batonneau, and A. Khelifa, “Preparation, characterisation and application of thermally treated Algerian halloysite,” *Microporous and Mesoporous Materials*, vol. 158, pp. 47–54, Aug. 2012, doi: 10.1016/j.micromeso.2012.03.014.

[93] S. Saklar and A. Yorukoglu, “Effects of acid leaching on halloysite,” *Physicochemical Problems of Mineral Processing; ISSN 2083-3989*, 2015, doi: 10.5277/PPMP150108.

[94] D. Garcia-Garcia, J. M. Ferri, L. Ripoll, M. Hidalgo, J. Lopez-Martinez, and R. Balart, “Characterization of selectively etched halloysite nanotubes by acid treatment,” *Applied Surface Science*, vol. 422, pp. 616–625, Nov. 2017, doi: 10.1016/j.apsusc.2017.06.104.

[95] S. C. Yan, Z. S. Li, and Z. G. Zou, “Photodegradation Performance of g-C_3N_4 Fabricated by Directly Heating Melamine,” *Langmuir*, vol. 25, no. 17, pp. 10397–10401, Sep. 2009, doi: 10.1021/la900923z.

[96] A. Thomas *et al.*, “Graphitic carbon nitride materials: variation of structure and morphology and their use as metal-free catalysts,” *J. Mater. Chem.*, vol. 18, no. 41, p. 4893, 2008, doi: 10.1039/b800274f.

[97] S. Tonda, S. Kumar, S. Kandula, and V. Shanker, “Fe-doped and -mediated graphitic carbon nitride nanosheets for enhanced photocatalytic performance under natural sunlight,” *J. Mater. Chem. A*, vol. 2, no. 19, p. 6772, 2014, doi: 10.1039/c3ta15358d.

[98] H. Shaikh *et al.*, "Facile and Low-Cost Fabrication of ZnO/Kaolinite Composites by Modifying the Kaolinite Composition for Efficient Degradation of Methylene Blue Under Sunlight Illumination," *Catalysts*, vol. 15, no. 6, p. 566, Jun. 2025, doi: 10.3390/catal15060566.

[99] R. Djefaflia, D. Lerari, and K. Bachari, "Covid-19 and nanoform zinc oxide interaction: a forcite module of materials studio software study," *Cla. Resear.*, vol. 38, no. 2, p. 43, 2019, doi: 10.5958/0974-4509.2019.00001.9.

[100] G. Calis-Ismetoglu and H. I. Unal, "Surface engineering of halloysite with graphene oxide via primary and secondary forces, characterizations, and electrokinetic properties," *Materials Today Communications*, vol. 35, p. 106101, Jun. 2023, doi: 10.1016/j.mtcomm.2023.106101.

[101] *Murray, H. H. (2007). Applied Clay Mineralogy: Occurrences, Processing and Applications of Kaolins, Bentonites, Palygorskite-Sepiolite, and Common Clays. In H. H. Murray (Ed.). Developments in Clay Science (Vol. 2, 180 p). Amsterdam: Elsevier.*

[102] C.-C. Wang, X.-H. Yi, and P. Wang, "Powerful combination of MOFs and C3N4 for enhanced photocatalytic performance," *Applied Catalysis B: Environmental*, vol. 247, pp. 24–48, Jun. 2019, doi: 10.1016/j.apcatb.2019.01.091.

[103] Y. Pang *et al.*, "Metal-doped carbon nitride: an all-in-one photocatalyst," *EES Catal.*, vol. 1, no. 6, pp. 810–831, 2023, doi: 10.1039/D3EY00123G.

[104] A. Farcy *et al.*, "Kinetic study of p-nitrophenol degradation with zinc oxide nanoparticles prepared by sol–gel methods," *Journal of Photochemistry and Photobiology A: Chemistry*, vol. 456, p. 115804, Nov. 2024, doi: 10.1016/j.jphotochem.2024.115804.

[105] S. A. Ansari, "Elemental semiconductor red phosphorus/ZnO nanohybrids as high performance photocatalysts," *Ceramics International*, vol. 49, no. 11, pp. 17746–17752, Jun. 2023, doi: 10.1016/j.ceramint.2023.02.140.

[106] Z. Ye *et al.*, "Well-dispersed nebula-like ZnO/CeO2@HNTs heterostructure for efficient photocatalytic degradation of tetracycline," *Chemical Engineering Journal*, vol. 304, pp. 917–933, Nov. 2016, doi: 10.1016/j.cej.2016.07.014.

[107] M. Kumar *et al.*, "Structural evolution and optical tailoring of Mg-doped ZnO: Insights into doping-induced modifications," *Sci Rep*, vol. 16, no. 1, p. 8919, Mar. 2026, doi: 10.1038/s41598-026-40403-y.

[108] H. Yu *et al.*, "Facile synthesis of ZnO/halloysite nanotube composite with greatly enhanced photocatalytic performance," *Colloids and Surfaces A: Physicochemical and Engineering Aspects*, vol. 688, p. 133633, May 2024, doi: 10.1016/j.colsurfa.2024.133633.

[109] Z. Huang, L. Li, Z. Li, H. Li, and J. Wu, "Synthesis of Novel Kaolin-Supported g-C3N4/CeO2 Composites with Enhanced Photocatalytic Removal of Ciprofloxacin," *Materials*, vol. 13, no. 17, p. 3811, Aug. 2020, doi: 10.3390/ma13173811.

[110] M. Nguyen Van *et al.*, "Fe-Doped g-C3N4: High-Performance Photocatalysts in Rhodamine B Decomposition," *Polymers*, vol. 12, no. 9, p. 1963, Aug. 2020, doi: 10.3390/polym12091963.

[111] S. Khosrovan, J. Vahdati Khaki, M. Mirjalili, M. M. Matin, and N. Esfandiari, "Synergistic Mechanisms Underlying Optical, Antimicrobial, Anticancer, and Antioxidant Activities of Multifunctional Bioactive ZnO/CuO/Clay Nanocomposites," *ACS Appl. Bio Mater.*, vol. 8, no. 12, pp. 11190–11205, Dec. 2025, doi: 10.1021/acsabm.5c01884.

[112] H.-L. Guo, Q. Zhu, X.-L. Wu, Y.-F. Jiang, X. Xie, and A.-W. Xu, "Oxygen deficient ZnO_{1-x} nanosheets with high visible light photocatalytic activity," *Nanoscale*, vol. 7, no. 16, pp. 7216–7223, 2015, doi: 10.1039/C5NR00271K.

[113] L. Jiang *et al.*, "Doping of graphitic carbon nitride for photocatalysis: A review," *Applied Catalysis B: Environmental*, vol. 217, pp. 388–406, Nov. 2017, doi: 10.1016/j.apcatb.2017.06.003.

[114] S. Tonda, S. Kumar, S. Kandula, and V. Shanker, "Fe-doped and -mediated graphitic carbon nitride nanosheets for enhanced photocatalytic performance under natural sunlight," *J. Mater. Chem. A*, vol. 2, no. 19, p. 6772, 2014, doi: 10.1039/c3ta15358d.

[115] Y. Li *et al.*, "Synthesis and photocatalytic activity of a bentonite/g-C3N4 composite," *RSC Adv.*, vol. 4, no. 23, p. 11831, 2014, doi: 10.1039/c3ra46818f.

[116] M. H. Suhag, A. Khatun, I. Tateishi, M. Furukawa, H. Katsumata, and S. Kaneco, "Visible Light Induced Photocatalytic Degradation of Diclofenac in Aqueous Solution Using Fabricated ZnO/g-C_3 N_4 by Facile Calcination Technique," *ACS Omega*, vol. 9, no. 45, pp. 45090–45103, Nov. 2024, doi: 10.1021/acsomega.4c05679.

[117] A. Kubala-Kukuś *et al.*, "X-ray photoelectron spectroscopy analysis of chemically modified halloysite," *Radiation Physics and Chemistry*, vol. 175, p. 108149, Oct. 2020, doi: 10.1016/j.radphyschem.2019.02.008.

[118] P. Yuan, D. Tan, and F. Annabi-Bergaya, "Properties and applications of halloysite nanotubes: recent research advances and future prospects," *Applied Clay Science*, vol. 112–113, pp. 75–93, Aug. 2015, doi: 10.1016/j.clay.2015.05.001.

[119] J. Li *et al.*, "Enhanced photocatalytic activity of g-C_3 N_4 –ZnO/HNT composite heterostructure photocatalysts for degradation of tetracycline under visible light irradiation," *RSC Adv.*, vol. 5, no. 111, pp. 91177–91189, 2015, doi: 10.1039/C5RA17360D.

[120] A. E. A. Aboubakr *et al.*, "Direct Z-Scheme Heterostructure of In Situ Planted ZnO Nanorods on g-C_3 N_4 Thin Sheets Sprayed on TiO_2 Layer: A Strategy for Ternary-Photoanode Engineering toward Enhanced Photoelectrochemical Water Splitting," *ACS Appl. Energy Mater.*, vol. 7, no. 3, pp. 906–918, Feb. 2024, doi: 10.1021/acsaem.3c01992.